Structure Investigations of $LiMn_2O_4$ as Oxygen Evolution Reaction Catalyst

---

Dissertation

for the award of the degree
"Doctor rerum naturalium"
of the Georg-August-Universität
within the doctoral program
Physics
of the Georg-August University School of Science (GAUSS)

submitted by

Florian Schönewald
from Wolfhagen, Germany

Göttingen, 2023

Thesis committee
Prof. Cynthia A. Volkert, PhD
Institut für Materialphysik
Georg-August-Universität Göttingen

Prof. Dr. Jörg Behler
Lehrstuhl für Theoretische Chemie II
Ruhr-Universität Bochum

Dr. Marcel Risch
Nachwuchsgruppe Gestaltung des Sauerstoffentwicklungsmechanismus
Helmholtz Zentrum für Materialien und Energie

Members of the examination board
Prof. Cynthia A. Volkert, PhD
Institut für Materialphysik
Georg-August-Universität Göttingen

Dr. Marcel Risch
Nachwuchsgruppe Gestaltung des Sauerstoffentwicklungsmechanismus
Helmholtz Zentrum für Materialien und Energie

Further members of the examination board
Prof. Dr. Jörg Behler, Lehrstuhl für Theoretische Chemie II Ruhr-Universität Bochum
Prof. Dr. Michael Seibt, IV. Physikalisches Institut
Prof. Dr. Hans Hofsäss, II. Physikalisches Institut
Prof. Dr. Vasily Moshnyaga , I. Physikalisches Institut

Date of the oral examination: 06.03.2023

Abbreviations

BE	Binding Energy	27
CV	Cyclic Voltammetry	57
DFT	Density Functional Theory	13
EELS	Electron Energy Loss Spectroscopy	3
EEL	Electron Energy Loss	3
ETEM	Environmental Transmission Electron Microscopy	25
FWHM	Full Width at Half Max	26
HAADF	High Angle Annular Dark Field	46
HER	Hydrogen Evolution Reaction	5
HR	High Resolution	44
IMFP	Inelastic Mean Free Path	32
KE	Kinetic Energy	31
OER	Oxygen Evolution Reaction	1
ORR	Oxygen Reduction Reaction	5
RHE	Reversible Hydrogen Electrode	24
ROI	Region of Interest	38
RRDE	Rotating Ring Disc Electrode	24
RSF	Relative Sensitivity Factor	27
STEM	Scanning Transmission Electron Microscopy	3
TEM	Transmission Electron Microscopy	21
THF	Tetrahydrofuran	24
XAS	X-ray Absorption Spectroscopy	9
XPS	X-ray Photoelectron Spectroscopy	20
XRD	X-ray Diffraction	27

Contents

1. Introduction

The scenario of limiting global warming to 1.5 °C requires a massive decrease of current CO_2 emissions towards net-zero in 2050.[1] Thus, one of the biggest challenges for our societies is the transformation from a fossil fuel based to a carbon emission-free energy supply.[2] Wind and solar energy are feasible carbon-neutral technologies that even surpass conventional energy sources in cost efficiency, but lack reliability due to a high volatility. In average, the wind energy production is 16% of the total installed capacity in Germany. But only 0.4% of the total capacity is available with a probability of 99.5%.[3] Thus, energy storage systems are crucial to ensure a reliable energy supply which can be adapted to the varying energy demand and to allow for a highly efficient use of generated electricity.[3,4]

The splitting of water to H_2 and O_2 is one of the most attractive approaches to store an energy surplus chemically in times when the energy production exceeds the demand.[5] If the electricity demand surpasses the production by wind, solar or other energy sources, the stored energy can be fed back into the power grid using fuel cells. In addition to stationary applications for electricity supply, H_2 is also attractive to replace fossil fuels in the mobility sector, since gravimetric and volumetric energy densities of hydrogen surpasses the one of battery technologies.[6]

Generation of elemental hydrogen via an electrochemical reaction is rate limited by the transfer of four electrons and four protons during the Oxygen Evolution Reaction (OER), which hampers the efficiency of the water splitting reaction. To drive the OER at reasonable rates, a comparably high overpotential of several hundred mV is necessary while the minimum potential for this reaction is 1.23 V.[7] As a consequence, searching for optimized OER catalysts has become a central research goal. IrO and RuO have been identified as benchmark catalysts[8] but the high cost and limited abundance hinder their application on a big scale. Thus, it has to be identified what factors determine catalytic activity in order to design cost-effective, abundant and environ-

ment friendly OER catalysts.

Unravelling the individual steps and mechanisms of the electron transfer from or to the catalyst in an experiment is far from being trivial, which complicates deduction of universal design principles for active and stable OER catalysts. An approach that has been successful in developing active catalysts is to identify descriptors, which are material properties showing a correlation with catalytic activity. Although descriptors do not necessarily need to represent cause-effect relationships, they lead to finding highly active catalysts.[9,10] Prominent descriptors are the adsorption energy of oxygen on the catalyst surface[11–15] or the binding energies of O* and HO*reaction intermediates.[11,15] Often descriptors have a volcano like relationship with activity, which means that there is an optimum value of the descriptor leading to peak activity. Materials with a higher or lower descriptor value have a linear decreasing activity.[11,15] This behaviour is reflected in the Sabatier principle, which states that the catalyst-reactant interaction must neither be too strong, nor too weak for optimum activity. Because it is difficult to experimentally measure binding energies of adsorbates,[15] research focused on accessible material properties, often based on bulk electronic or geometric structure, that correlate with the adsorbate binding energies and thereby OER activity.[9–13,15–19] This approach might not lead to a fundamental understanding of the OER mechanism and the rate limiting reaction steps, but it can provide guidelines to focus research on important aspects.[13]

Mn based catalysts gained popularity in catalyst research since Mn is abundant, has low toxicity and is the active site of the oxygen evolving complex in natural photosynthesis.[7,9,20–24] Especially Mn oxides in form of perovskites, spinels and related structures have been in focus as condensed matter catalysts due to their rich Mn redox chemistry.[25] Various candidates for descriptors have been tested on these materials. Electronic structure based properties e.g. the number of transition metal d electrons,[12] the O $2p$ band centre,[26] the metal-oxygen covalence[10] or the metal e_g occupancy[9,16] exhibited correlations with OER activity. The transition metal e_g occupancy for example shows the expected volcano shape when plotted against activity, with a peak activity at an e_g occupancy of 1.0 or a Mn valence of Mn^{3+}.[9,16]

Interestingly, using bulk properties of different materials has been successful in finding activity-property correlations in a number of studies.[9–13,15–19] However, it can-

not be assumed without further experiments that properties of material surfaces are identical to bulk properties or that they change accordingly when a bulk property is tuned.[12] Breaking the crystal symmetry at $LiMn_2O_4$ surfaces can lead to geometric reconstruction[27] or to differing oxidation state distributions.[28] Since reactants interact at catalyst surfaces it has to be assumed that the surface structure should have a more direct influence on the OER than bulk properties. The overriding importance of surface properties is highlighted by the fact that changing the surface termination[29] or orientation[30] of a material has significant impact on activity, although the bulk properties are identical. While applying bulk descriptors has been successful in some cases, this clearly shows that they are not able to narrow down the path in understanding what property directly influences the mechanisms of the OER. Instead, the characterization of surface properties is crucial for a reliable understanding of catalytic reactions.[31]

In this thesis, $LiMn_2O_4$ is investigated as a model system for OER catalysis where the catalytic-relevant octahedral Mn d or e_g states can be tailored by electrochemical delithiation without changing the crystal symmetry.[32,33] The octahedral Mn-O framework is fixed while the octahedral Mn valence can be selected through the occupancy and oxidation state of the ions on the tetrahedral and octahedral sites. Thereby, the influence of the Mn e_g occupancy on the intrinsic OER catalytic activity is studied directly without the need to discuss effects of coordination or structure changes.

The goal of this thesis was to resolve the electronic and crystal microstructure of the model catalyst with high resolution and to monitor how the control tactic delithiation impacts material properties relevant for catalysis at the catalyst surfaces. In addition, the stability of the model system, when used for OER catalysis, was investigated to test, if the approach of literature studies, that link descriptors based on pre-characterization to OER activity, is reliable. In combination with OER activity measurements performed by Max Baumung and Omeshwari Bisen, the role of Mn e_g occupancy as a single descriptor for OER activity was tested.

To establish a link between the catalytic activity of $LiMn_2O_4$ nanoparticles and a material property, the local structure of samples used as OER catalysts was resolved. Different surface sensitive techniques with focus on Scanning Transmission Electron Microscopy (STEM)-Electron Energy Loss Spectroscopy (EELS) were applied. Comparing Electron Energy Loss (EEL) measurements on pristine particles to simulated spectra,

based on DFT calculations, revealed a core-shell structure where the overall oxidation state of Mn in the shell is reduced through the presence of anti-site tetrahedral Mn^{2+}. While electrochemical delithiation could tune the core oxidation state successfully, the shell structure remained unchanged. In contrast, the tetrahedral Mn defects are dissolved out of particle shells during OER catalysis, thereby changing the near surface octahedral Mn oxidation state.

Surprisingly, the effect of the surface e_g occupancy on OER catalytic activity is much smaller than expected from the established literature descriptor[9,16] while the tetrahedral Li occupancy does affect the OER activity as expected.[34] This makes clear that near-surface octahedral Mn valence or e_g occupancy, which should be affected by both tetrahedral ions similarly, is not a sufficient descriptor of OER catalytic activity. More differentiated measures than Mn valence or e_g occupancy, which include both geometric and electronic structure, are required to describe the active catalytic surface.

2. Background

Scope of this chapter is to give an overview about the $LiMn_2O_4$ structure and known effects in this material, as well as to summarize viewpoints and challenges in understanding the mechanisms of electrocatalyzing the OER.

2.1. OER Catalysis by Transition Metal Oxides

The reaction of generating elemental oxygen and hydrogen out of water using electrolysis

$$2H_2O \rightarrow 2H_2 + O_2 \tag{2.1}$$

can be divided in the two sub reactions Hydrogen Evolution Reaction (HER) and OER.[35] The HER, which occurs at the cathode, is the reaction:

$$4H^+ + 4e^- \rightarrow 2H_2 \tag{2.2}$$

while O_2 is evolved at the anode via the reaction

$$2H_2O \rightarrow 4H^+ + O_2 + 4e^- \tag{2.3}$$

The standard Nernstian potential of the OER is 1.23 V. That means that oxygen is oxidised and evolves at potentials higher than this value while at lower potentials than 1.23 V, the reduction of oxygen is favoured (Oxygen Reduction Reaction (ORR)).[15,35] However, the OER is found to be kinetically limited and thus is the rate limiting step in the water splitting reaction.[35] As a consequence, large overpotentials need to be applied to drive the OER reaction at reasonable rates which impacts the overall efficiency of this reaction severely. In order to improve the efficiency of the OER and thereby making hydrogen as energy carrier more attractive, it is necessary to understand the origin of the overpotential and to find catalysts that have a better OER activity.[11]

The binding energy[11] or adsorption energy[36] of species on the catalyst surface has been found to influence the amount of overpotential and therefore the catalytic activity. A volcano shaped relationship between OER overpotential and the standard free energy difference of absorbed $\Delta G^0_{O^*} - \Delta G^0_{HO^*}$ has been reported[11] which agrees with the Sabatier Principle. This states that the interaction of reactants in the water splitting reaction with the catalysts surface must neither be too weak, nor too strong to facilitate an optimum amount of absorption and desorption. Still, even if $\Delta G^0_{O^*} - \Delta G^0_{HO^*}$ is optimised, the overpotential of the best catalyst is between 0.2 V and 0.4 V.[11] To understand the origin of the overpotential, four-step mechanisms of the OER have been proposed, where the reaction O_2 evolution happens at one site at the catalysts surface.[10,11,15,35,37] The individual steps differ from model to model, since it has yet not been possible to resolve the full OER mechanism in an experiment.[15] The following steps have been proposed for transition metal spinels in an alkaline solution.[10] Stars (*) mark a species that is adsorbed on a transition metal centre in the surface of the OER catalyst.

$$(1)\ OH^- + {}^* \rightarrow OH^* + e^- \tag{2.4}$$

$$(2)\ OH^* + OH^- \rightarrow H_2O + O^* + e^- \tag{2.5}$$

$$(3)\ OH + O^* \rightarrow OOH^* + e^- \tag{2.6}$$

$$(4)\ OOH^* + OH^- \rightarrow O_2 + H_2O + e^- \tag{2.7}$$

An individual Gibbs reaction energy ΔG^0_i can be assigned to each reaction step (i). The origin of the non-vanishing overpotential can thus be understood as the deviation of the individual reaction energy of one step from the equilibrium value of 1.23 V.[11,35] If the surface properties of a catalyst are altered, one reaction energy might decrease while others increase. In a four step model that means, that the step with the highest Gibbs reaction energy is determining the overpotential of the OER[37]:

$$G_{OER} = [\Delta G^0_1,\ \Delta G^0_2,\ \Delta G^0_3,\ \Delta G^0_4]_{max} \tag{2.8}$$

Therefore, an ideal catalyst would have equal Gibbs reaction energies of $\Delta G^0_i = 1.23\,eV$ for each step. However, the binding energies of a reaction intermediate, which are an important variable for the reaction energies,[11] can not be tuned individually by altering the catalysts surface properties. Instead, scaling relations between the binding energies of different surface steps have been found, which interlink all four reaction

intermediates, on metals[36,37] as well as for perovskites and spinels.[11] These scaling relations are linear correlations between adsorption energies that have been found independent on the catalysts material class. Thus, G_{OER} is only dependent on one parameter, which imposes a thermodynamical limit to the optimization of overpotentials. Thus, a material class that breaks or has optimized scaling relations needs to be found in order to design an OER catalyst that has zero overpotential.

2.2. Activity Descriptors

Binding energies have been used successfully to describe and to predict the catalytic behaviour in different material classes.[11,12,36,37] These reports rely on binding energy calculations since it is difficult to determine them in experiments.[15] As a result, descriptors that are accessible more easily have been established which show correlations of OER activity with material properties. Investigating activity descriptors might then lead to deeper understanding about how OER activity is governed by material properties.[36] These descriptors can then be used to predict highly active materials or deliver guidelines to design novel materials for efficient OER catalysis. In the following paragraphs, different established property-activity relationships are summarized.

2.2.1. Number of Outer Electrons

The influence of the number of valence electrons on absorption energies of O^*, OH^*, and OOH^* and OER catalytic activity was investigated on pure metals, metal oxides, and on different perovskite structures by either changing the oxidation state of the metal or by varying the site population in a fixed compound.[17,36,38] General trends for perovskites are, that an increasing number of valence electrons, while maintaining the *B* site metal oxidation state, leads to a weakening of adsorbate binding. At the same time, an increase of the *B* site oxidation state by changing the *A* site occupation leads to a weaker bond as well. As a result, the adsorption energy of reaction intermediates does not only depend on the number of outer electrons but also on the oxidation state of the element in octahedrally coordinated *B* sites, which is summarized in Fig. 2.1. In addition, linear correlations between the bulk formation energy and the number of outer electrons could be established, leading to volcano relationships between OER overpotential and bulk formation energy.[12] The reported volcano is however not universal for the different material classes, which means that bulk formation energy or

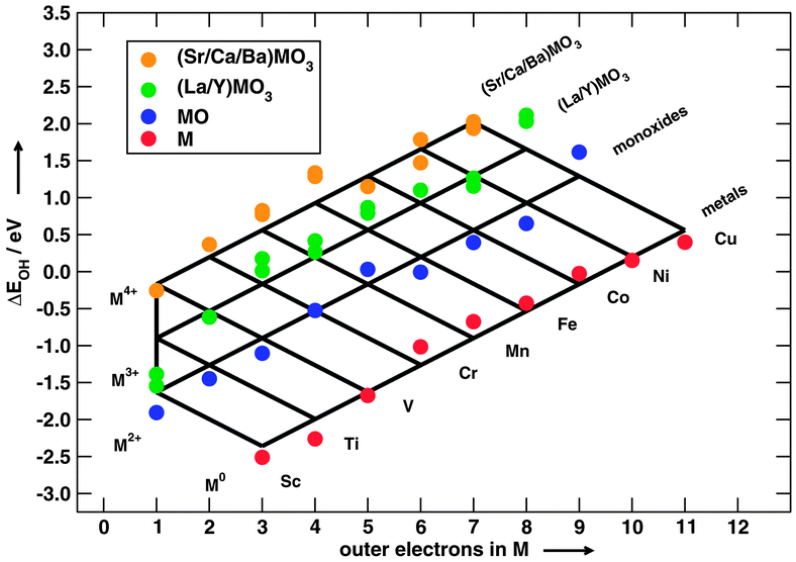

Figure 2.1.: OH adsorption energy dependencies of number of metal *d* electrons. Data points with identical colour indicate constant oxidation state of the elements, but a change in *d* electron number by a change of element. Negative indicated slopes highlight the impact of a change of the oxidation state of the same element. Reprinted from ref. [12] with permission from Royal Society of Chemistry, permission conveyed through Copyright Clearance Center, Inc.

number of outer electrons can only explain activity trends if compared in materials with identical coordination and structure.

2.2.2. O $2p$ Band Centre

Properties of transition metal oxides, such as the number of outer electrons, do not only correlate with absorption energies, but are also interlinked with each other. Both, the O-p band centre as well as the transition metal d-band centre change with the number of outer electrons of *B* site cations in perovskites.[26,38] A general trend is that increasing the *d* electron number results in decreasing the energy distance between the O *p* and metal *d* bands. This distance of the oxygen $2p$ band centre to the Fermi level was proposed as a descriptor for activity in double perovskites and showed a linear relationship with activity. It was found to be a more reliable measure compared to e_g occupancy, when transition metals exist in multiple coordination states in a double perovskite.[39] Shifting the $2p$ band centre closer to the Fermi level leads to an increase in oxygen binding energy and OER activity.[26,39] However, if the distance to the Fermi

level gets too small catalyst corrosion was reported as a negative side effect.[39] Increasing the oxygen p band centre leads to a greater metal-oxygen hybridization, since the overlap of O p and metal d band increases. This indicates that covalence can be considered as an activity descriptor as well.

2.2.3. E_g Occupancy of Transition Metals

The e_g occupancy of transition metals in perovskites and spinels is directly related to the oxidation state and thus, the number of outer electrons, which has been discussed as descriptor for OER activity previously. A significant difference of e_g occupancy to the formal oxidation state is that the transition metal valence band splits up in the anti-bonding e_g orbital with σ character and in the bonding t_{2g} orbital having π character.[9] This leads to a stronger interaction of e_g orbitals with the ones of an adsorbed species compared to the t_{2g} states. Hence, it is assumed that e_g filling is more accurate in describing activity than using the whole transition metal d band.[31] It has been pointed out, that a reliable description of OER activity necessitates to measure and use the e_g occupancy of surface atoms, rather than bulk values since broken bonds can alter the e_g occupation.[31]

Applying this descriptor to perovskites and spinel structures resulted in volcano shaped OER activity-e_g occupancy plots.[9,16] These relationships are based on e_g occupancy of B site ions in perovskites[9] and of the octahedrally coordinated transition metal in spinels.[16] In case of transition metal spinels, metals can reside in both, octahedral and tetrahedral sites which does not allow to differentiate activity of different sites a priori. Focussing on octahedral e_g occupancy was justified by the arrangement of orbitals with metal d character. The e_g and t_{2g} orbitals of tetrahedrally coordinated metals do not point in the direction of O, in contrast to e_g states of octahedrally coordinated atoms. This leads to the assumption that the metal-oxygen interaction in tetrahedral sites can be neglected.[16] Both studies report an optimum activity at an e_g occupancy close to 1, however the peaks of the volcano plots predict an optimum activity at $e_g \approx 1.2$. Based on this finding a catalyst (BSCF) was designed, having optimal e_g occupancy, which has a comparable overpotential and mass activity as the benchmark catalyst IrO_2.[9] Surprisingly, e_g occupancy of octahedral metals in spinels result in a volcano shaped behaviour that agrees well with the behaviour of perovskites, even though a bulk sensitive method (X-ray Absorption Spectroscopy (XAS) in transmission mode) was used

to determine e_g occupancy and neglecting surface effects. The e_g occupancy in octahedral sites - activity relationship is plotted in Fig. 2.2. The approximation of using bulk

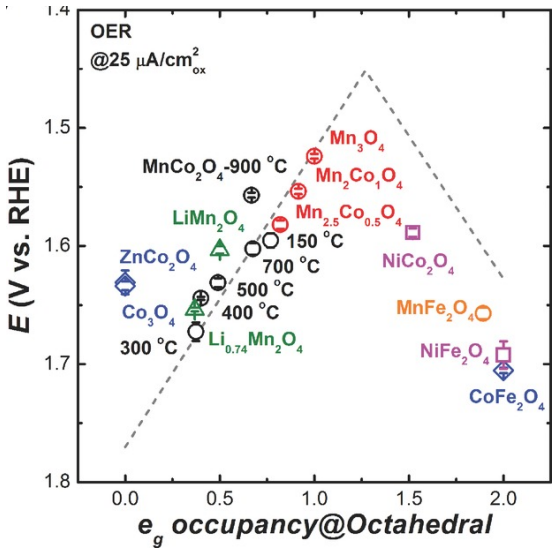

Figure 2.2.: OER activity described by e_g occupancy of octahedral coordinated metals in spinels with different compositions. The activity is measured as potential that is necessary to achieve a current of 25 mA/cm^2 where the area is the measured available oxide surface. Reprinted with permission of John Wiley and Sons, from ref. [16]

properties instead of surface values can be justified if a clear relationship between bulk and surface properties exists. This has been shown for example for bulk formation energy, which scales linearly with absorption energies of reaction OER intermediates.[12]

In case of spinels, e_g occupancy has been questioned to be a universal activity descriptor. In a study that investigated more than 300 spinel structures, descriptors that have been successfully applied to perovskites (such as O 2p band centre or e_g occupancy) have not been able to describe catalytic activity universally.[10]

2.2.4. Alternative Descriptors

Transition metal oxides have a variety of electronic and structural properties that can be used as possible descriptors that scale with OER activity. A statistical analysis of 101 activities of 51 perovskite structures investigated the reliability of 14 descriptors in activity prediction. These 14 descriptors were divided into 5 factors that can be considered as descriptor families.[17] Although being considered as activity descriptor

previously,[9] e_g occupancy has a lower loading magnitude in the descriptor family of electron occupancy than *d* electrons. This indicates that they describe activity differences of different materials as a single descriptor poorly.[17]

Although single descriptors have been used in previous studies and showed an expected volcano shaped activity behaviour,[9,10,16,39] they are not sufficient when applied to a bigger data set of perovskites. Instead, a model including two descriptors enhances the probability of predicting activity, but best prediction necessitates the inclusion of 9 descriptors for an activity model.[17] Within this model the number of *d* electrons and covalence have been found to have the biggest influence on activity which justifies the use of descriptors that are based on the electronic structure of a material, rather than crystal structure or tolerance factors.[17]

That covalence is a superior activity descriptor has been reported for perovskites[17,40] and spinel systems as well.[10,41] Opposed to the argument that octahedral sites are the active sites for OER catalysis,[16] the covalence of metal-oxygen bonds in either tetrahedral or octahedral coordination is named as an activity governing descriptor. The bonding strength to oxygen differs between tetrahedrally and octahedrally coordinated metals. Since an oxygen atom is coordinated with tetrahedral and octahedral metals at the same time, the oxygen *p* orbitals coordinated with both metal sites. The weaker metal-oxygen bond is more likely to break at the surface, which leads to unpaired valence electrons that can participate in the OER reaction steps.[10] Independent of the coordination, both metal sites can be active. Covalence is defined as the energy difference of the metal *d* and oxygen *p* band centre. The metal-oxygen bonding is considered stronger if the energy difference is smaller and both bands have a bigger overlap. The descriptor for OER activity uses the maximum value of covalence of the two differently coordinated metals.[10] A volcano relationship has been reported applying this descriptor to experimental activity values of other publications. An explanation for the observed volcano is that less pronounced covalence enhances the possibility of metal-oxygen bond breakage, thereby enhancing activity. However, if the covalence is too weak, this implies that the metal-oxygen bond is too polarized. In case of a bond breakage this might lead to formation of metal ions at the surface which hinders adsorption of reaction species at these metal centres. An optimum covalence of 3 eV is predicted.[10]

As a summary, covalence values have been calculated and reported for 300 spinel structures, including $LiMn_2O_4$ and defect structures with Mn on tetrahedral and Li on octahedral sites.[10] It has to be criticised that the crystal structures used for calculating covalence of $MnMn_2O_4$ and $LiMn_2O_4$ for example deviate from experimentally determined structures. For $LiMn_2O_4$ a tetragonal structure with $a = c = 8.172$ Å and $b = 8.71$ Å was used for calculations which disagrees with the experimentally determined cubic spinel structure. The local geometry around Mn atoms differs if the lattice is tetragonally distorted, which will probably affect the band structure calculations. If no good reason exists to assume that the metal *d* and oxygen *p* band positions stay constant when the lattice gets distorted, it has to be doubted that the calculated covalence measures reflect experiments reliably.

2.2.5. Strain Effects on Activity

The effects of strain on the electronic structure of transition metals and transition metal oxides have received attention as a way to tune OER catalytic activity of perovskite catalysts,[38,42–46] but have been investigated on pure metal systems as well.[47–49]

A clear correlation between strain, the metal *d* bandwidth and the metal *d* band centre was established for metals. If the band is occupied more than half, compressive strain in late transition metals leads to broadening of the metal *d* band and a lowering of its average energy, and vice versa for tensile strain (see Fig. 2.3).[47,48,50] In early transition metals, an opposite *d*-band centre shift was observed. While compressive strain still leads to a broadening of the metal *d* band, its centre moves to higher energies.[44] The maximum amount of strain reaches from 1.75%[48] to 8%[49] in the investigated systems. Perovskites show different reactions to strain as well, dependent on the transition metal occupation. The amount and direction of a *d* band shift, as a reaction to band broadening, scales with the number of *d* electrons of the *b* site metal.[38,45] Since the relationship between the O *sp* band and the transition metal *d* band has been discussed intensively as activity descriptor (see previous section) it is particularly interesting that, for compressive strain, the energy of the lower O *sp* band edge moves to smaller energies compared to the Fermi level and that the energy gap between the O *sp* band and the metal *d* band increases.[45]

Furthermore, strain affects the orbital occupation of metal e_g orbitals in perovskites.Strain

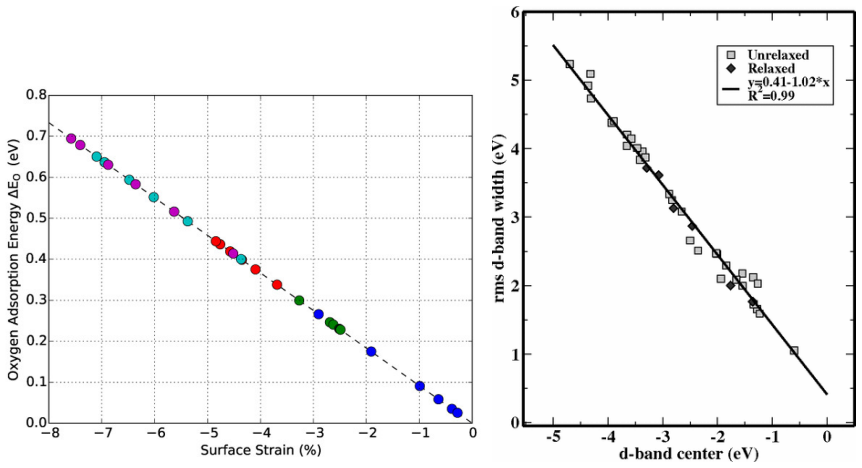

(a) (b)

Figure 2.3.: Effect of compressive strain on oxygen adsorption energy on Pt/Cu nanoparticles based on Density Functional Theory (DFT) calculations (a). Reprinted from ref [49] with permission from American Chemical Society, Copyright 2015. Relationship between metal d band centre position and width for bimetallic Ni/Pt surfaces calculated using DFT (b). Reprinted from ref [47] with permission from the American Physical Society, Copyright 2004.

causes a splitting of the e_g $x^2 - y^2$ and $3z^2 - r^2$ orbitals, where compressive strain leads to a lower energy and thus preferential occupation of e_g $3z^2 - r^2$ orbitals. This is depicted in Fig. 2.4. The opposite is reported for tensile strain.[42,46] Due to symmetry

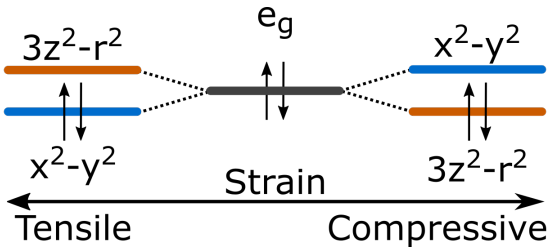

Figure 2.4.: Splitting and preferential occupation of e_g orbitals if strain deforms octahedrally coordinated metals.

breaking at the surface, the e_g orbital is expected to degenerate even without strain, leading to preferential occupation of out of plane orbitals. Compressive strain can strengthen this tendency, while tensile strain can invert this preference and leads to in-plane orbital occupation.[46] The assumption that orbitals pointing out of the surface play a key role in adsorption and desorption processes of reaction intermediates led to the identification of e_g occupancy as activity descriptor in perovskites[31] and

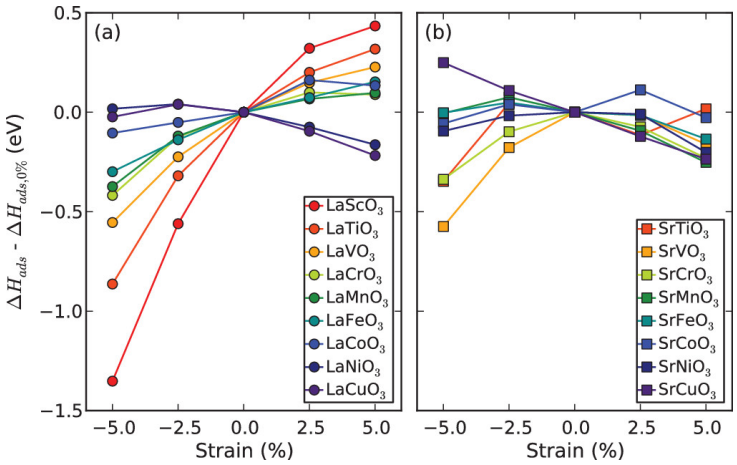

Figure 2.5.: Relative oxygen adsorption energy change on (001) perovskite surfaces with varying *B* site occupation if strain is imposed. Reprinted with permission from ref. [38]. Copyright 2012 AIP Publishing.

spinels.[16] Thus, strain is expected to influence catalytic activity.

The impact of strain on surface properties and OER or ORR catalytic activity has been investigated via adsorption energy calculations[38,47–49] or by measuring activity on thin films that have been prepared on substrates with different lattice mismatch.[42,51]

The O adsorption energy on metals increases by about 0.08 eV/%[48,49] under compressive strain if the *d* orbitals are more than half filled.[52] This corresponds to a weaker interaction with adsorbed O. For platinum for example, a compressive strain of 2.25% optimizes the ORR activity.[49] How strain affects the adsorption energies on perovskite surfaces is not as clear, as can be seen in Fig. 2.5.

In LaBO$_3$, compressive strains decreases the O binding energy, where the decrease is more pronounced in early transition metal *B* site population. In SrBO$_3$ this trend is much less pronounced and applying compressive and tensile strain only results in a small decrease of O adsorption energy.[38] Thus, the impact of strain on the oxygen binding energy depends on the number of *d* electrons and on the structure environment (*A* site occupation).

That the impact of strain on activity is ambiguous is reflected in experimental studies. Both, compressive and tensile strain led to an activity increase in epitaxial NdNiO$_3$ thin

films. The positive impact of tensile strain is explained by an enhanced oxygen vacancy formation.[42] A different observation was made using $CaRuO_3$ thin films, where tensile strain increased OER activity, and compressive strain lead to a decreasing activity compared to samples with small strain.[51]

That means that a generalized trend of how strain in catalyst surfaces affects the OER cannot be established. The impact of strain on oxygen adsorption energies and OER activities is governed to a large extent by factors like the transition metal d electron number in metals and perovskites, as well as by the interaction of B site cations with A site cations. In addition to that, the strain induced changes on absolute values of oxygen adsorption energies are comparably small in relation to the effect of e.g. the number of d electrons. A change of the B site cation in $LaBO_3$ from Ti to Cu leads to an oxygen adsorption energy difference of more than 6 eV[36,38] compared to a change between 1.5 eV and 0.25 eV if an amount of 5% of compressive or tensile strain is applied.[38] In metals, an even smaller impact of 0.08 eV/% is observed. Therefore, strain can be a strategy to optimize OER activity in a material system, but is not able to fundamentally change it.

2.3. $LiMn_2O_4$ Structure and Surface Effects

Important structure features of the material $LiMn_2O_4$ used in this work will be discussed in the following paragraphs. This includes the general structure and behaviour under delithiation as well as defects and surface effects that have been reported in literature.

2.3.1. $LiMn_2O_4$ Structure

$LiMn_2O_4$ spinels have been investigated for almost 70 years,[53] but gained interest in the 1980s. That the Li content x in $Li_xMn_2O_4$ can be varied reversibly without affecting the Mn_2O_4 framework of the host material[54,55] makes this material a candidate for a cathode material in rechargeable Li-ion batteries.

Cubic spinel structures have the general formula $A[B_2]X_4$ and Fd3m symmetry, where the anions X, in this specific case O, form a cubic close packed structure and occupy the 32e sites. B-site cations are octahedrally coordinated with O on the 16d sites which

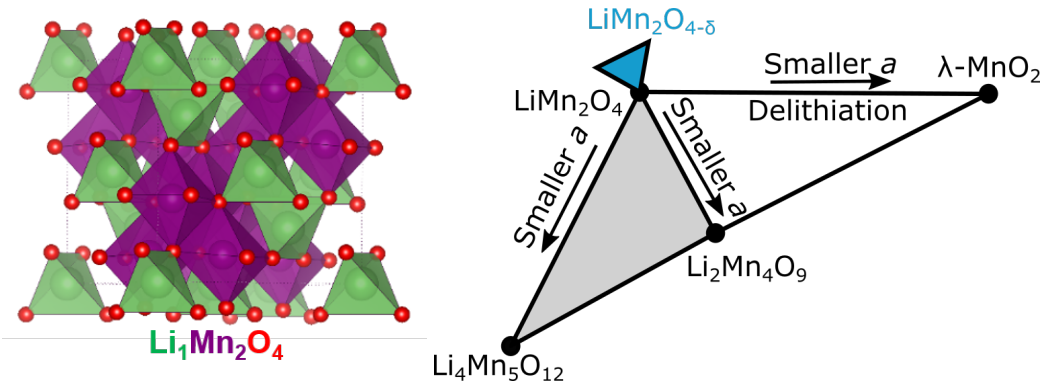

(a) (b)

Figure 2.6.: Cubic spinel structure of $LiMn_2O_4$ with site occupation (a). Excerpt of ternary Li-Mn-O phase diagram (b) following Yonemura *et al.*[57]. Bulk stoichiometry variations and defect structures are highlighted in grey and blue.

means that half of the totally available sites are occupied. The *A* site cations, Li in this case, have tetrahedral coordination and occupy the 8a sites. Thereby, one eighth of tetrahedral sites are populated.[56]

A complete removal of Li is possible via acid treatment[54] or electrochemical methods at a potential of 4 V vs Li/Li^+.[55,58] This forms the metastable λ-MnO_2 structure, which has the identical crystal symmetry as $LiMn_2O_4$ and is accompanied by a contraction of the unit cell parameter from 8.24 Å at $x = 1$ to 8.03 Å at $x = 0$. At the same time, the average Mn oxidation state increases from $Mn^{3.5+}$ at $x = 1$ to Mn^{4+} after removing Li completely.[54] Thus, the sum formula can be also expressed as $Li_{1-x}[Mn^{3+}_{1-x}Mn^{4+}_{1+x}]O_4$.

Delithiation of $LiMn_2O_4$ in electrochemical cells, battery cells in other words, exhibits a characteristic electrochemical profile that indicates a two stage process which is divided by a 0.15 V step at the composition $Li_{0.5}Mn_2O_4$. This step in the potential diagram has been explained by Li ordering,[59,60] a coherent picture of the underlying order mechanism is however elusive.[61] The delithiation process can be stopped at any Li content x, allowing to investigate how the crystal structure changes with the Li content. The lattice constant a decreases linearly with Li removal,[32,58,62,63] but phase separation in two cubic spinel structures with different lattice constants has been observed at varying Li contents at varying delithiation rates.[58,62–65] That a two phase regime is thermodynamically favoured could not be supported in DFT based calcula-

tions of the $Li_xMn_2O_4$ structure in different delithiation states.[32] In addition, phase separation could be suppressed by reducing the delithiation rate or by allowing the samples to equilibrate after end of the delithiation experiments.[62] This is a strong indication, that a phase separation at certain Li contents is not an equilibrium state but rather a kinetic effect of removing Li from a bulk electrode.[62] As a result, the Li content in $Li_xMn_2O_4$ can be determined by measuring the lattice parameter.

As pointed out, Li removal leads to a decrease of the amount of Mn^{3+}, which is expected to show a Jahn-Teller distortion. This means that the oxygen octahedron and thus the bond distances around a Mn^{3+} atom are elongated or shortened along one axis and vice versa at the other four-fold axes,[66] which lowers the total energy of the configuration. As a consequence, half of the Mn in $LiMn_2O_4$ should be located in distorted octahedra having two different Mn-O bond distances while the other half is expected to be located in regular octahedra as Mn^{4+}. Close to room temperature at 290 K, a phase transition to orthorhombic symmetry has been observed in this material[67,68] and explained in a theoretical study by a cooperative alignment of Jahn-Teller distortions.[32] In agreement with that postulation, different Mn-O bond distances are found in experiments in that low temperature phase.[66,69,70] If the material has the cubic spinel structure above the transition temperature, the theoretical study predicts that Mn^{3+} sites still show Jahn-Teller distortions, but that the distortions at single sites can change direction on a sub pico-second timescale and do not align cooperatively. The time average then leads to the observed cubic symmetry.[32,71] Nonetheless, the expected differing Mn-O bond distances of Jahn-Teller distorted octahedra could not be resolved in measurements yet. Instead, a distortion of all Mn-O octahedra was resolved where all 6 Mn-O bonds have different lengths.[66] This implicates a conflict of experimental data with simulated structures. Either the timescales of fluctuations of the Mn bonding environment are too short to be accessible by experiments, or a Jahn-Teller deformation does not set-in in real systems.

2.3.2. Bulk Defects and Stoichiometry Variations

Starting from $LiMn_2O_4$, where Li solely occupies tetrahedral and Mn occupies octahedral sites, stoichiometry and site occupation variations are possible within the cubic spinel structure. These can be divided into the categories of oxygen deficient, defect, and stoichiometric spinels.[59,72]

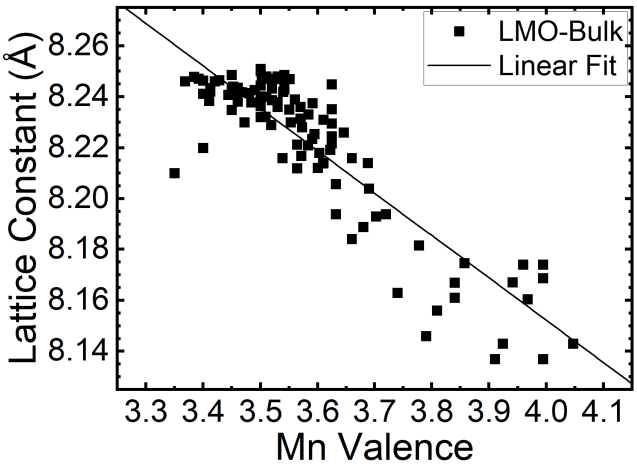

Figure 2.7.: Influence of bulk stoichiometry variations and defects on the lattice constant of spinels of the $LiMn_2O_4$ system evaluated against the average Mn valence in those structures. Data points are collected from various literature reports.[57,59,64,72–80] The Mn valence was either directly reported or evaluated on the basis of the given composition.

Stoichiometric spinels, also specified as Li excess spinels,[57] follow the general $A[B_2]X_4$ composition, but additional Li can partially replace Mn in octahedral sites which results in $Li_{8a}[Mn_2 - \delta Li_\delta]_{16d}O_4$ structures with $(0 \leq \delta \leq 0.33)$. These compositions lie on the $LiMn_2O_4$-$Li_4Mn_5O_{12}$ tie line in the Li-Mn-O phase diagram. An increasing Li occupation of octahedral sites leads not only to a decrease of Jahn-Teller active Mn^{3+}, but also to a decreasing lattice constant down to a =8.137 Å[59] and a =8.168 Å[73] at $\delta = 0.33$ (see Fig. 2.7). Both, a linear and saturation like relationship of the lattice constant a with the defect concentration x have been reported.[73,74] A higher Mn^{4+} concentration reduces the overall capacity of repeatable Li de/-intercalation at 4 V but enhances the stability of the material when used repeatedly as cathode material in batteries and causes a decreasing temperature for the orthorhombic phase transition.[57,59,74] The opposite effect, occupation of tetrahedral sites by Mn in bulk defect structures, was only observed for very small concentrations with a maximum of 1% of all Mn found on tetrahedral sites.[75]

Cation vacancies form the category of defect spinels. Compositions of $Li_{1-\delta}[Mn_2 - 2\delta]O_4$ with $(0 \leq \delta \leq 0.11)$ lie on the $LiMn_2O_4$-$Li_2Mn_4O_9$ tie line. At the maximum

vacancy concentration of $\delta = 0.11$, all Mn has the oxidation state Mn^{4+}. The synthesis temperature was shown to be a control parameter for δ, where higher temperatures lead to smaller vacancy concentrations.[74] As in the case of Li excess spinels, the increasing Mn valence is accompanied by a smaller lattice parameter (see Fig. 2.7). At the maximum defect concentration of $\delta = 0.11$, a lattice parameter of a =8.174(1) Å is expected.[59]

Oxygen vacancies can be introduced in the $LiMn_2O_4$ structure by varying synthesis conditions like temperature, time and atmosphere during heating.[64,72] They are found in the blue triangle in the phase diagram in Fig. 2.6b.[57] A precise control of the amount of O vacancies is difficult since the Li and Mn stoichiometry can be affected by varying synthesis conditions as well. Oxygen vacancies cause Mn reduction which is reflected in an increasing lattice constant, which is agrees with the trend of previously discussed defects.[57,64,72,75] Although the reported defect concentrations of $\delta \leq 0.13$ in $LiMn_2O_{4-\delta}$ are comparably small (3.25% of all oxygen) the phase transition temperature and cycling stability under repeated de-/lithiation are impacted significantly by O defects. The orthorhombic phase transition temperature increases with the O vacancy concentration, which leads to the hypothesis that a certain amount of O vacancies must be present for the phase transition to occur.[57,64,72] On the other hand, presence of O vacancies leads to quicker cathode degradation when used in battery experiments.[64]

Thus, the bulk structure of the $LiMn_2O_4$ system is far from being trivial. A number of variables in the synthesis process like the Li/Mn ratio, maximum temperature and temperature profile as well as the atmosphere, determine the exact stoichiometry, defect type and concentration of the resulting material. That means it is not straightforward synthesizing $LiMn_2O_4$-related spinels with a defined composition and defect structure. It has been shown in various studies that bulk defects, imposing Mn oxidation state changes, distinctively change the lattice constant. Higher average Mn oxidation states result in smaller lattice constants and vice versa. This connection is plotted for over a hundred reported defect structures in Fig. 2.7.

2.3.3. Surface Defects and Stoichiometry Variations

Similar to the bulk, stoichiometry and site population variations are reported at surfaces of $LiMn_2O_4$ spinels. The literature mainly discusses Mn populating tetrahedral

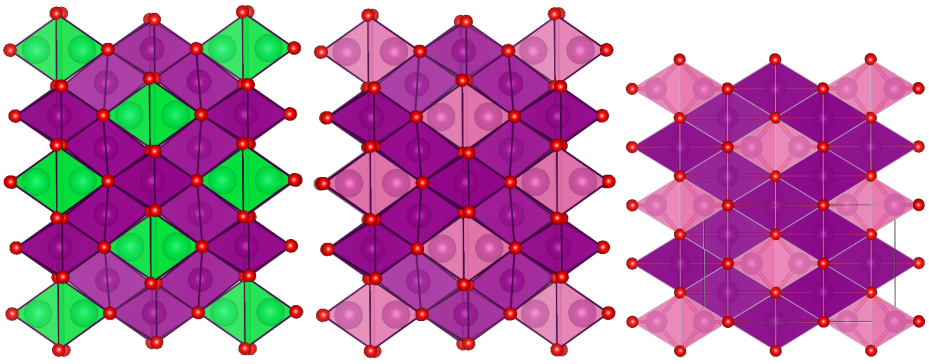

(a) (b) (c)

Figure 2.8.: Projection of the crystal structure of cubic spinel $LiMn_2O_4$ along [110] showing the octahedral and tetrahedral sites (a). Identical structure, but with Mn replacing Li on tetrahedral sites (b). Equivalent crystallographic orientation of tetragonal Mn_3O_4 (c), where tetrahedral sites are occupied by Mn as well. The structural motive is comparable to cubic spinel, but distorted. Plots were created using Vesta.[84]

sites and oxygen vacancies.[81, 82] While oxygen vacancies also occur as bulk defect, Mn antisite defects on tetrahedral sites were solely reported in a few nm thick surface layers.[83]

Mn in tetrahedral sites, which has oxidation state Mn^{2+}, was either detected by a contrast in tetrahedral sites in high resolution STEM images in [110] zone axis[81–83,85] (see Fig. 2.8), or by changes of the oxygen and Mn edges in X-ray Photoelectron Spectroscopy (XPS) and EELS spectra. Presence of tetrahedrally coordinated Mn in surface regions was detected after delithiation[81,82] as well as in pristine state.[83,85]

If all Li is replaced by Mn in $LiMn_2O_4$, the site population is identical to Mn_3O_4 with the difference that Mn_3O_4 has a tetragonal crystal structure. The additional electron that is doped if a Li atom is replaced by Mn in a tetrahedral site leads to a higher amount of Jahn-Teller active Mn^{3+} and thus to the preference to form a tetragonal crystal structure, when the Mn valence drops below $Mn^{3.5+}$. Reported high resolution images do however not indicate that the surface has a different crystal structure if Mn^{2+} is present, instead the particles are single crystalline.[81–83,85,86] As depicted in Fig. 2.8c, formation of Mn_3O_4 would lead to an increase of the Mn_{oct}-tet-tet-Mn_{oct} distance by 15%. In addition, no direct observation of the Mn_3O_4 crystal structure has been reported except after several cycles of de-/lithiation.[83] Still, strain is expected in

surfaces with the cubic spinel geometry when tetrahedral Mn^{2+} increases the amount of Jahn-Teller active Mn^{3+}. Since relaxation of a strained lattice is easier at surfaces than in the bulk, the formation energy of Mn antisite defects is expected to be lower at surfaces.[87] That explains that tetrahedral Mn is exclusively reported in surface regions. This aligns well with a DFT based model of surface reconstructions in $LiMn_2O_4$, which predicts a reduced Mn oxidation state due to surface reconstruction at all surface terminations. In addition, formation of fourfold coordinated Mn^{2+} has been observed in relaxed surfaces,[27] where formation of reduced Mn oxidation states is explained by a lower cost of Jahn-Teller distortions at surfaces.

Oxygen vacancies were reported at surfaces of $LiMn_2O_4$ particles, which led to a reduced Mn oxidation state and an increased Mn/O ratio. Since Transmission Electron Microscopy (TEM) images did not show contrast of Mn on tetrahedral sites, the formation of oxygen vacancies was proposed.[88] In contrast to other studies, the reduced Mn oxidation state led to a tetragonal distortion of the lattice at the surface. The concentration of oxygen vacancies was found to alternate from site to site.[88]

3. Materials and Methods

This chapter gives an overview of the sample material, sample preparation methods as well as data acquisition and evaluation techniques. Section 3.1 describes the starting material and summarizes the preparation of delithiated and electrochemically cycled particles. Section 3.2 lists specimen preparation techniques, conducted experiments, and instrument parameters sorted by method. A brief description of the applied experimental techniques, including background information about data interpretation and evaluation, is given in Section 3.3. The description of TEM techniques and EELS data interpretation and Mn valence evaluation partially overlaps with the equivalent parts of the pre-print Schönewald *et al.*[89]. Details of electrochemical experiments are summarized based on publications of Max Baumung covering OER catalysis[90] and delithiation.[34]

3.1. Material and Electrochemical Preparation

3.1.1. Material

$LiMn_2O_4$ powder was purchased from Sigma-Aldrich (single synthesis batch, purity >99%) with a nominal particle size smaller than 500 nm. The powder has a lattice constant of 8.234(2) Å[32] and a cubic spinel structure. The particles mainly consist of truncated octahedra and some truncated rhombic dodecahedra with a mean particle diameter of 41(15) nm.[91]

3.1.2. Delithiated Particles

The lithiation state of $LiMn_2O_4$ has been manipulated using an electrochemical battery cell that was built and operated by Max Baumung. The following summarizes the essential steps. A detailed description has been reported by Baumung[34]. The purchased $LiMn_2O_4$ particles were mixed with carbon black (mass ratio 83/17) and distributed on

a stainless steel electrode. A cotton separator, soaked in ethylene carbonate/dimethyl carbonate (50:50) (EC/DMC) and lithium hexafluorophosphate ($LiPF_6$), was placed between the powder and the metallic Li counter electrode. All components are pinched by a spring, the cell is sealed under an inert gas atmosphere in a glovebox. A constant current (c/12 rate - 12 h for a full charge) was applied to charge the battery cell. Delithiated material was removed by disassembling the cell in a glovebox.

Even at comparably small charge rates of c/12 or lower, phase separation has occurred where two cubic spinel $LiMn_2O_4$ phases with different lattice constants are present.[58,65] This is, presumably, caused by a non-homogeneous Li distribution in the $Li_xMn_2O_4$ powder. Therefore, particles were not investigated directly after delithiation to ensure for the sample to reach an equilibrium state and a homogeneous Li concentration.

3.1.3. Particles Catalyzing the OER

OER activity of $LiMn_2O_4$ in different lithiation states has been measured using a Rotating Ring Disc Electrode (RRDE) setup. While the disc is used to apply a potential to the catalyst and to measure the total induced currents, the ring can be used to detect reaction products if set to a designated potential. Preparation and execution of OER catalysis experiments has been performed by Max Baumung. The essential steps and details of these experiments[90] are summarized in the following.

Particles have been mixed with carbon black in a weight ratio of 83/17, were dissolved in Tetrahydrofuran (THF) and then applied on the glassy carbon disc electrode. While being rotated in sodium hydroxide (NaOH), that was diluted with ultrapure water to $c_{NaOH} = 0.1\,\mathrm{M}$, ten scans have been performed by varying the disc potential at a rate of $10\,\mathrm{mVs}^{-1}$ between 1.25 V and 1.75 V vs. Reversible Hydrogen Electrode (RHE). The ring potential was set to oxygen (0.4 V vs. RHE) or manganese (1.2 V vs. RHE) detection. After cycling, the particles were rinsed from the electrode and diluted in THF or isopropanol for drop casting on TEM grids.

3.2. Specimen Preparation and Experiments

3.2.1. TEM Specimens

Post-mortem TEM measurements have been performed on pristine, and delithiated particles, as well as on particles that catalysed the OER. Samples were prepared by drop casting a particle-solvent immersion on copper mesh grids that are coated with lacey carbon. Prior to drop casting, the immersion was sonicated for 15 minutes to break particle agglomerates. The particle distribution on the grid was controlled with a light microscope. To avoid contamination by the solvent, it is recommended to prepare immersed samples one day before the planned experiment.

EELS spectrum images were recorded using a step size of 1 nm, a high loss illumination time between 0.1 s and 0.3 s, a spectrometer dispersion of 0.1 eV and an electron beam current in STEM mode of 50 pA. Particles were selected for measurement if they were located (partially) in a hole of the lacey carbon film to minimize background intensity. Eight to fourteen particles, that varied in size and thickness, were measured in one experiment.

In-situ Environmental Transmission Electron Microscopy (ETEM) measurements have been performed on pristine particles. The evolution of the local structure under the influence of a water atmosphere and an electric potential was studied with high resolution TEM and STEM-EELS. The potential was applied using a biasing chip and holder. Fig. 3.1 displays the plan view scheme of this setup.

A piece was cut out of the chip to allow for a larger electron transparent area. Particles were drop cast on a grid as described just before. A piece was cut from that grid and glued with conductive silver on the biasing chip. Electronic contact was checked by measuring the resistance between contacts on opposite sides of the chip. Values of approximately 5 Ω indicated a proper contact to the grid. The resistance between chip and holder/ground should exceed that by several orders of magnitude. Values greater than 12 MΩ have been measured. Conductive silver releases solvent gases. Measurements one or two hours after gluing the grid onto the chips resulted in drastic electron beam contamination. A good strategy is to insert the holder with the chip the day before the measurement into the TEM column.

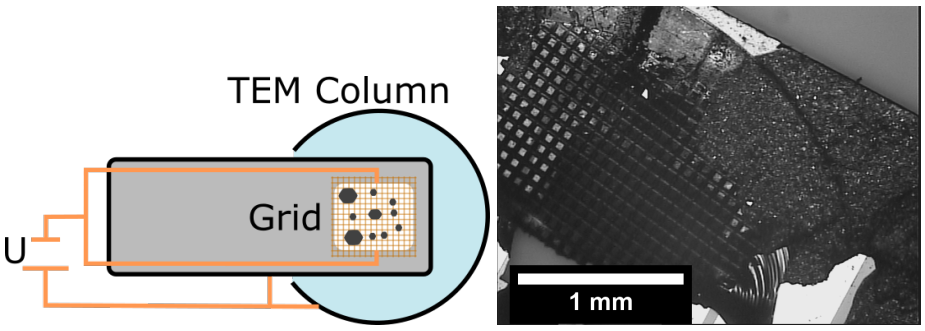

(a) (b)

Figure 3.1.: Plan view of the biasing chip that was used in in-situ ETEM experiments. A potential versus the TEM column was applied externally. Particles were drop cast on a copper grid that was mounted onto the contacts of the biasing chip. (a) shows a sketch of the chip and the electrical connections. (b) displays a light microscope image of the mounted grid piece on the biasing chip.Improve formatting

In-situ experiments have been carried out in a controllable water atmosphere in the TEM column of 0.2 mbar. High resolution TEM experiments were carried out in one single particle. Image series before water contact, in water atmosphere and with applied potential were recorded with the particle being oriented in a zone axis. For STEM-EELS experiments, a series of particles were pre-characterized in high vacuum state. The influence of a water atmosphere and a varied potential was studied in separate steps on separate particles to avoid high electron doses on single particles.
High resolution ETEM imaging and STEM-EELS were performed with an image C_s corrected FEI Titan ETEM at 300 kV acceleration voltage, equipped with a Quantum 965ER Gatan Image Filter and X-FEG by FEI. The Full Width at Half Max (FWHM) of the electron energy distribution in the electron beam is 1.3 eV.

3.2.2. XPS Specimens

XPS measurements have been carried out on particles in pristine state, after catalysing the OER and after delithiation with a Kratos Axis Supra instrument, that is equipped with a monochromatic Al k_α X-ray source. Samples of particle powder were prepared by pressing powder on double-sided conductive carbon tape. As prepared RRDE glassy carbon electrodes for electrochemical measurements were directly mounted on the XPS sample holder thereby ensuring electrical contact to the holder. Therefore, the

glassy carbon cylinders were pressed on conductive carbon tape on the XPS sample holder.

Overview scans were performed on all samples with a pass energy of 160 eV and with a Binding Energy (BE) step size of 1 eV. High resolution scans of the Mn 2p, the O 1s, the C 1s and Mn 3p edge, that contains the Li 1s peak, were performed with a step size of 0.05 eV and a pass energy of 5 eV. The auto quality criteria was set to 500 to achieve a very high signal-to-noise ratio.

Prior to data evaluation, the BE scale has been corrected for potential charging by shifting the C 1s maximum to a BE of 284.8 eV. For quantification and determination of the Mn $2p_{3/2}$ centroid, a Shirley background was subtracted. Quantification was carried out using the instrument specific Relative Sensitivity Factor (RSF), incorporating transmission and escape depth correction.

3.2.3. XRD Specimens

The crystal structure of pristine particles was investigated using $\theta - 2\theta$ X-ray Diffraction (XRD) in a Bruker D8 diffractometer with a Cu Kα source in the angular range $15° \leq 2\theta \leq 120°$ and with a total measurement time of 106 h. $LiMn_2O_4$ powder was embedded into glue on a plastic sample plate. Electrochemically cycled material was prepared for measurements by mounting the complete glassy carbon electrode. In addition, powder from six electrochemical experiments was distributed on Kapton tape to enhance the density. The material density was however not sufficient to gain structural signals of the particles.

3.3. Methods and Evaluation

3.3.1. TEM and EELS

TEM and STEM are methods that allow to investigate the sample structure with sub nanometre resolution. A sufficient description of the principles and physics of a TEM quickly exceeds the scope of this chapter and this thesis so that the following paragraphs focus on fundamentals that are necessary to understand the experimental set-up and gained results within this work.

Inherent in the name, TEM and STEM generate data from electrons that have penetrated samples and thereby interacted elastically or inelastically with atoms in the specimen. Electrons have a small mean free path in solids, which necessitates high acceleration voltages and thin samples ($\approx 100\,\mathrm{nm}$). Electrons are generated, accelerated to high velocities, focused on the sample using electromagnetic lenses and are projected with an electromagnetic lens system on a camera or varying detectors in the imaging plane. The sample surface is illuminated homogeneously in TEM mode, where either real space or reciprocal space information can be projected into the imaging plane. Real space images allow resolving the structure of the sample with atomic resolution. In STEM mode, however, the incoming electron beam is converged to illuminate a tiny fraction of the sample, smaller than $1\,\mathrm{nm}^2$. Detected electrons thus only contain information from a well confined area. By rasterising the beam over the sample, images are compounded.

EELS is a spectroscopic method that measures the intensity distribution of energy loss from electrons that interacted inelastically with the sample. A spectrometer is fitted to the bottom of the TEM column, which projects the electron beam energy dispersively on a camera. In combination with STEM, this allows to gain EEL spectra with a very high spatial resolution. Commonly, EEL spectra are divided in a low-loss and a core loss region. The low-loss region contains the zero loss peak (not interacted and elastically scattered electrons) and low energy excitations of plasmons and valence band electrons, for example. Based on Poisson's law, the relative sample thickness t/λ can be calculated using the low-loss spectrum:[92]

$$t/\lambda = \ln(I_t/I_0) \tag{3.1}$$

I_0 describes the intensity of non-scattered electrons, I_t the total intensity in the low-loss spectrum, t the distance that an electron travelled through a sample and λ the inelastic mean free path.

The core-loss region contains intensity from electrons that excited core electrons of atoms in the sample. Observed curve shapes of a core-loss edge $J(E)$ can be understood as a product of the density of final states $N(E)$ with the atomic transition matrix

$M(E)$[92] under the assumption of single scattering

$$J(E) = |M(E)|^2 N(E). \tag{3.2}$$

Since $M(E)$ describes the overall edge shape, the variations with E can be assumed as being small. Therefore, $N(E)$, that depends on the bonding environment of the excited atom, dominates the observed fine structure. The obtained spectral resolution is limited in this work by the finite energy distribution of the generated electron beam.

3.3.2. EELS Interpretation of Mn Oxides

EELS analysis in this work will focus on the oxygen K- and manganese L-edges of manganese oxides. The oxygen K edge contains excitations of oxygen 1s electrons to unoccupied O 2p states. In manganese oxides, O 2p orbitals overlap with Mn valence states. Thus, a strong correlation exists between the O K-edge shape and the Mn electron configuration. As a result, the position and intensity of the O pre-peak at 530 eV are sensitive to the Mn 3d occupancy and the hybridization strength of O 2p and Mn 3d orbitals.[93] Peaks centred around 540 eV reflect O 1s excitations to O 2p states that are mixed with the Mn 4sp band.[93] The Mn L-edge between 640 eV and 655 eV reflects transitions from Mn $2p_{3/2}$ (L_3 peak) and $2p_{1/2}$ (L_2 peak) levels to unoccupied Mn 3d states and is sensitive to the Mn 3d occupancy as well.[94,95]
How Mn 3d occupancy affects O K- and Mn L-edges is illustrated in Fig. 3.2. A decrease of the Mn oxidation state, hence an increase of 3d occupancy, leads to a decrease of the O pre-peak intensity compared to the EEL region at 545 eV because the number of unoccupied states with Mn 3d character decreases. At the same time, the pre-peak maximum shifts to higher energies. Noticeable is the pre-peak doublet structure (labelled as a_2 in Fig. 3.2a) in Mn_3O_4, where Mn is coordinated octahedrally and tetrahedrally. How this doublet structure can be interpreted in a density of states picture is discussed when tetrahedral Mn defects are investigated by EELS simulations.

The Mn L_3 peak at 640 eV shifts to lower energies if the nominal oxidation state is reduced. This is accompanied by an increase of the L_3/L_2 peak intensity ratio, also known as white line ratio.[96] Manganese in Mn_3O_4 exists in two distinct oxidation states (Mn^{2+} in tetrahedral and Mn^{3+} in octahedral coordination), which is reflected by a splitting of the Mn $L_{2,3}$ peaks (See (Fig. 3.2b). This allows to distinguish if different

Mn oxidation or coordination states are present in a sample.[97]

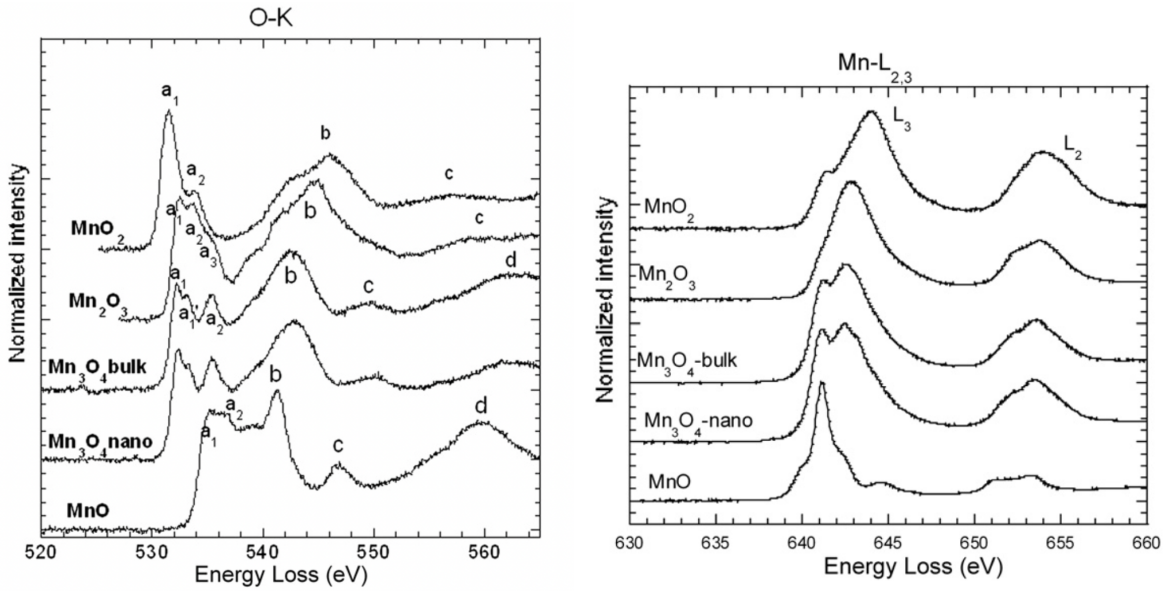

(a) (b)

Figure 3.2.: EEL O k- (a) and Mn l-edges (b) of Mn oxides with Mn in different oxidation states. The spectra show systematic changes with a change of the Mn oxidation state, such as a decrease of the O pre-peak intensity at 530 eV or a shift of the Mn $2p_{3/2}$ peak at 640 eV towards lower energies if the Mn oxidation state is reduced. These trends are used to interpret changes of the Mn oxidation state in $LiMn_2O_4$ later in this thesis. Reprinted from ref.[97] with permission from Elsevier.

3.3.3. Evaluation of Mn Oxidation States by EELS

It is often useful to use the Mn valence as a simple proxy for the complex electronic structure. An easily applicable and qualitative method uses the Mn L_3/L_2 intensity ratio which is sensitive to 3*d* occupancy,[94–96,98] and has been used to determine the Mn valence in a variety of transition metal based materials.[98–101] However, it is known to fall short in capturing the oxidation state in some manganese oxides[102] and can only determine the Mn valence within 0.3.[103] Various calibration studies focused on perovskites,[98,100] or on Mn oxides with different crystal structures,[96,99,100] but none have focused exclusively on transition metal oxide spinels.

A second method based on the O K- to Mn L peak distance has been calibrated using a wide variety of manganese oxides with oxidation states between Mn^{3+} and Mn^{4+}, including $LiMn_2O_4$ and $Li_2Mn_2O_4$,[104] and is claimed to be more sensitive to Mn valence than the Mn L_3/L_2 intensity method.[101] This calibration method has been applied in this study to calculate Mn valence maps from the EEL spectrum images and Mn valence values from core and shell spectra. The reported relationship between peak distance ΔE and Mn valence V_{Mn} is[101]

$$V_{Mn} = 0.377\Delta E - 39.03. \tag{3.3}$$

Based on the reported errors, the uncertainty in the Mn valence calculation is $\sigma(V_{Mn}) = 0.12$. Since the particles were neither aligned in a specific zone axis nor scanned with atomic resolution during the STEM-EELS measurements, the EEL spectra and Mn valences reflect the average oxygen and manganese states in the unit cell.
However, differences as large as 0.3 between the valences predicted by the two methods suggest that these methods are best used only as qualitative measures of Mn valence. Instead of focusing on Mn valence alone, measured EEL spectra are compared to simulated spectra for different $LiMn_2O_4$ based structures with the focus on peak shape, intensity, and position. This so-called "fingerprinting" approach has been used[105,106] to take advantage of the multifaceted information provided about the electronic structure by the EEL spectra, that is not captured by the simple proxy of Mn valence.
Qualitative comparison of calculated spectra with experimental spectra has been successful in explaining the origin of fine structure of the oxygen K edge[107–109] and was able to identify partial population inversion in transition metal spinels.[108,109]

3.3.4. XPS

XPS applies the photoelectric effect. Electrons, which are bound to an atom, are excited by X-ray photons and thereby emitted into a vacuum as depicted in Fig. 3.3. The kinetic energy distribution of these photoelectrons is measured. Regarding conservation of energy, the relation Eq. (3.4) allows converting the measured Kinetic Energy (KE) distribution to an electron BE spectrum,[110] where $h\nu$ describes the X-ray photon energy in eV and Φ_{spec} the spectrometer work function.

$$\mathrm{BE} = h\nu - \mathrm{KE} - \Phi_{spec} \tag{3.4}$$

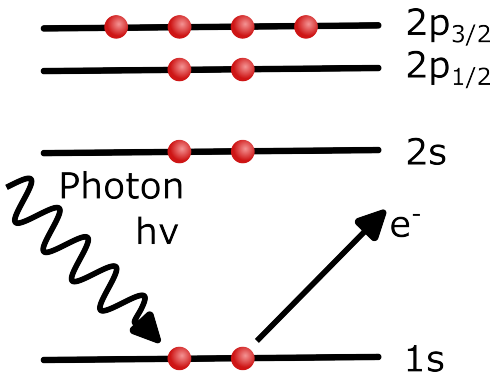

Figure 3.3.: Scheme of XPS process for the example of a 1s electron.

Peak positions in a BE spectrum are characteristic for the elements that are contained in the sample and allow identifying which elements are present down to a detection limit between 0.3 *at.*% and 0.01 *at.*% for most compounds.[111] The Inelastic Mean Free Path (IMFP) of electrons in solids with electron KE in the order of 1000 eV is in the range of a few nm. Hence, the obtained intensity will decay quickly with sample depth, which is described by Beer's law. The fraction $I(d)$ of the total intensity I_0 that is excited in a distance of d and deeper from the surface is

$$I(d) = I_0 \exp(-d/\lambda) \tag{3.5}$$

where λ is the effective attenuation length, similar to the IMFP.[110] As a result, XPS is a very surface sensitive technique.[112] In case of $LiMn_2O_4$ the IMFP is 17.7 Å for electrons excited (using Al kα radiation) from the Mn 2p state, 19.7 Å for the O 1s state and 26.7 Å for the Mn 3p and Li 1s state.[113] According to Eq. (3.5), approximately 63% of the total signal is generated in the first two nm of the sample and 86% in the first 4 nm.

While Peak positions are element specific, peak intensities are proportional to the element concentration in the probed volume, which allows determining the stoichiometry. Furthermore, it is possible to deduce the chemical state of an element from BE shifts and the peaks' fine structure.[110] In the simplest case, a peak of an element in a specific chemical state/oxidation state is approximated by a single Voigt peak.[114] For Mn oxides, however, the most intense 2p line splits up in a $2p_{3/2}$ and a $2p_{1/2}$ peak due to spin-orbit coupling. Multiplet splitting will further complicate the Mn $2p_{3/2}$ peak shape if Mn has unpaired d electrons[115]. Therefore, up to six Voigt components have to be used to model a Mn $2p_{3/2}$ peak - for a single oxidation state.[115] The peak cen-

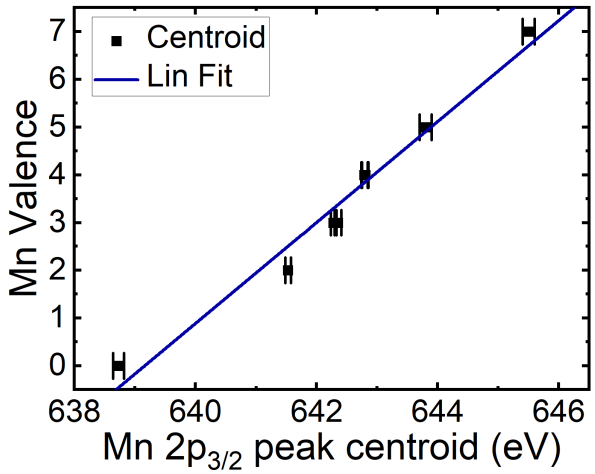

Figure 3.4.: Mn $2p_{3/2}$ peak centroid shift plotted versus the Mn valence for several Mn oxide standards, including a linear fit to the data points. The centroid has been calculated using the fit parameters that have been reported previously.[115]

troid is an alternative measure for the average Mn valence in the sample applying the linear relationship between Mn valence and the Mn $2p_{3/2}$ centroid shift (see Fig. 3.4). The shift is evaluated as energy difference between centroid and 642.5 eV on the basis of reported peak fit parameters of various Mn oxides.[115] A linear fit to the data in Fig. 3.4 allows to determine the average Mn valence using the equation:

$$\mathrm{Mn}_{ox}(\mathrm{BE}_c) = 1.057(0.08) \cdot \mathrm{BE}_c + 3.53(0.14). \tag{3.6}$$

The average Mn oxidation state can be measured with a precision of 0.33 based on the average residuum of the data points.

3.3.5. XRD

The angular distribution of elastically scattered X-rays is measured using XRD to gain information about the crystal structure of a sample. In a θ-2θ scan, the angle between the X-ray source and surface normal of the sample is equal to the angle between the detector, that measures the intensity of diffracted X-rays, and the surface normal. An intensity maximum is observed when the scattered X-rays interfere constructively. This condition is described by Bragg's law. If the phase shift of X-rays, that are scattered at

two neighbouring lattice planes with distance d, is a multiple of the wavelength $n \cdot \lambda$, both interfere constructively:

$$n \cdot \lambda \stackrel{!}{=} 2d \sin(\theta). \tag{3.7}$$

In a cubic crystal the distance between lattice planes d_{hkl} with miller indices (h,k,l) and the lattice constant a can be expressed as

$$d_{hkl} = \frac{a}{\sqrt{h^2+k^2+l^2}}. \tag{3.8}$$

Not all possible reflexes have to occur in a diffractogram. The structure factor F_{hkl}, that is dependent on the unit cell symmetry and element distribution, is zero in face centred cubic crystals if (h,k,l) have mixed parity. Thereby, those reflexes will not occur in diffractograms. The structure factor also scales the peak intensity $I_{hkl} = B_{hkl} \cdot V_{hkl}$ that is observed in a powder diffraction pattern

$$B_{hkl} = |F|^2 p \frac{1+\cos^2 2\theta}{\sin^2\theta \cos\theta}. \tag{3.9}$$

The multiplicity of identical lattice planes is described by p, the fraction describes the Lorentz-Polarisation factor. If two different crystallographic phases are present in a diffractogram, the volume ratio of the two phases can be estimated using Eq. (3.9):

$$\frac{V_1}{V_2} = \frac{I_{hkl;1} B_{hkl;2}}{I_{hkl;2} B_{hkl;1}}. \tag{3.10}$$

The observed peaks in a diffractogram are approximated by a Voigt profile. The FWHM depends on the instrument resolution, the crystallite size L and the residual strain ϵ. A crystallite size smaller than 200 nm[116] leads to peak broadening, which is described by the Scherrer Equation:

$$FWHM_{2\theta,L} = \frac{K\lambda}{L \cdot \cos(\theta)}. \tag{3.11}$$

K is the Scherrer form factor, whose value depends on the crystallite form. A value of 0.89 was taken for analysis.

Samples that are strained non homogeneously have a distribution of d rather than a fixed value. The imposed peak broadening of a mean strain of ϵ is:[116]

$$FWHM_{2\theta,\epsilon} = 4\epsilon \tan(\theta). \tag{3.12}$$

The resulting peak width can be assumed to be a linear combination of crystallite size (Eq. (3.11)) and strain broadening (Eq. (3.12)).[116] Multiplying with $\cos(\theta)$ leads to

$$FWHM_{tot} \cdot \cos(\theta) = 4\epsilon \sin(\theta) + \frac{K\lambda}{L}. \tag{3.13}$$

Plotting $FWHM_{tot} \cdot \cos(\theta)$ versus $\sin(\theta)$ allows reading the crystallite size from the y-axis intercept and ϵ from the slope of the observed linear trend.

Crystallite size, strain, and lattice constant a were calculated as a weighted average of all fitted peak positions. The two peak components from the two apparent copper k-α wavelengths were fitted independently, giving two 2θ values for each peak. The peak positions and peak intensities were evaluated by fitting two pseudo Voigt profiles with identical FWHM to the reflexes in the diffractogram. The peak positions for each Cu k-α component were evaluated separately to calculate the plane distance d from a reflex.

3.4. Simulation of EEL Oxygen K Edges

The observed core-shell structure of $LiMn_2O_4$ nanoparticles called for a deeper understanding of EEL spectra. This has been provided by Marco Eckhoff, former PhD student at the Institute for Physical Chemistry, University of Göttingen, via DFT based simulations of O K edges. These simulations are a key in substantiating the proposed defect model for particle surfaces. Details and assumptions underlying the simulations have been reported in a pre-print and are available via reference Schönewald *et al.*[89].

4. Results

4.1. Electron Beam Influence on EELS Measurements

It is beneficial for in-situ measurements if one single particle can be studied by STEM several times in a row. In order to identify if multiple measurements and thus accumulating electron dose at one location of a single particle are possible without damaging the particle with the e-beam, ten consecutive STEM-EELS scans have been performed at one particle (pristine $LiMn_2O_4$). The scan parameters (e-beam current=0.5 pA; pixel scan time=0.3 s; pixel size =1 nm^2) met the standard conditions of EEL spectrum imaging used in this work. The results of this experiment were used to plan and conduct in-situ experiments.

It is necessary to mention at this point, that the investigated $LiMn_2O_4$ particles have a core-shell structure with respect to the Mn oxidation state. The experimental results that lead to this conclusion are presented in the chapter Section 4.2. Therefore, the core and shell region of the particles are examined separately in this section.

The overview STEM image in Fig. 4.1a highlights that contrast, presumably contamination, builds up after the first scan. Carbon contamination is a known issue in TEM measurements due to decomposition of hydrocarbon molecules mainly by secondary electrons or the electron beam.[117,118] Molecules present on lacey carbon TEM grids, that were used in this work, are already enough to cause problems in STEM-EELS experiments with high illumination time.[119] The thickness of the contaminated layer scales linearly with the illumination time, while the growth rate increases for higher electron current densities and lower acceleration voltages.[120,121]

A relative thickness plot in Fig. 4.1b shows that the measured thickness t/λ in electron beam direction increases at the centre of the particle, while a strong increase is observed close to the particle's surface. Deviations from the expected linear increase of

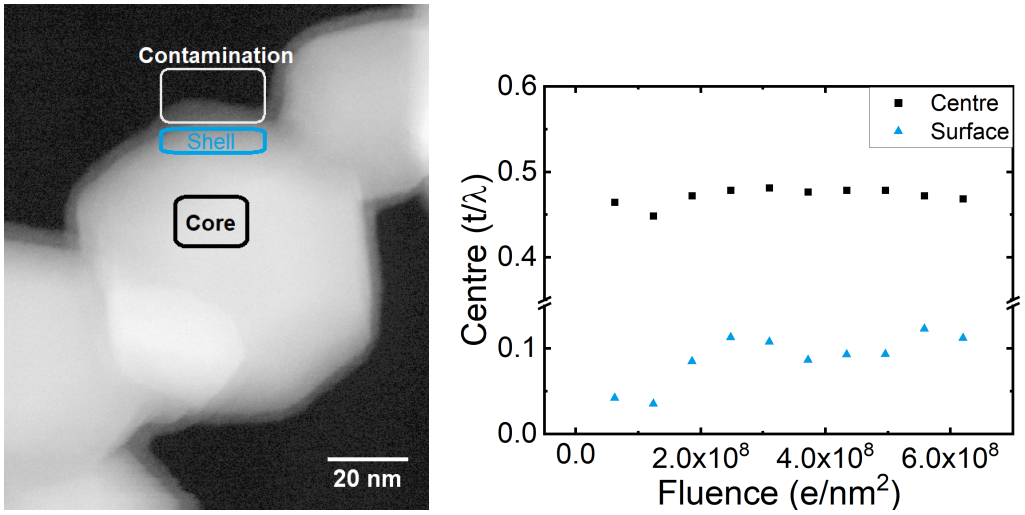

(a) (b)

Figure 4.1.: (a): Overview STEM image of particle after the first scan, showing that contamination built up. Highlighted areas show location from where EEL spectra of contamination, shell and core were extracted (see Fig. 4.3a and Fig. 4.2). (b): Thickness evolution (t/λ) at surface and particle centre with fluence.

t/λ occur because of sample drift. If the Region of Interest (ROI) shifts during a scan, previously not illuminated areas with less contamination will contribute to the resulting signal. A larger contamination growth rate is expected when scanned at surfaces parallel to the electron beam, if contamination formation is predominantly caused by secondary electrons. Secondary electrons typically have kinetic energies of few tens of eV, and thereby small mean free paths of a few nm in solids.[122,123] When scanned in proximity of a particle surface, a bigger part of secondary electrons can escape the particle, and therefore react with hydrocarbons as if scanned at the centre. After ten scans, the contamination layer thickness increased perpendicular to the particle boundaries but most prominently at the scan window position as shown in Fig. A.1. The non-linear thickness increase compared to the first scan can be attributed to shifts of the scan region due to sample drift, which leads to a non-homogeneous illumination during consecutive EELS scans.

Fig. 4.2 compares EEL spectra of the O K and Mn L edge of the first and the tenth scan. The position of the measurements on the particle are marked in Fig. 4.1a. Core and shell spectra after ten scans have a decreased O pre-peak intensity, a smaller Mn L_3

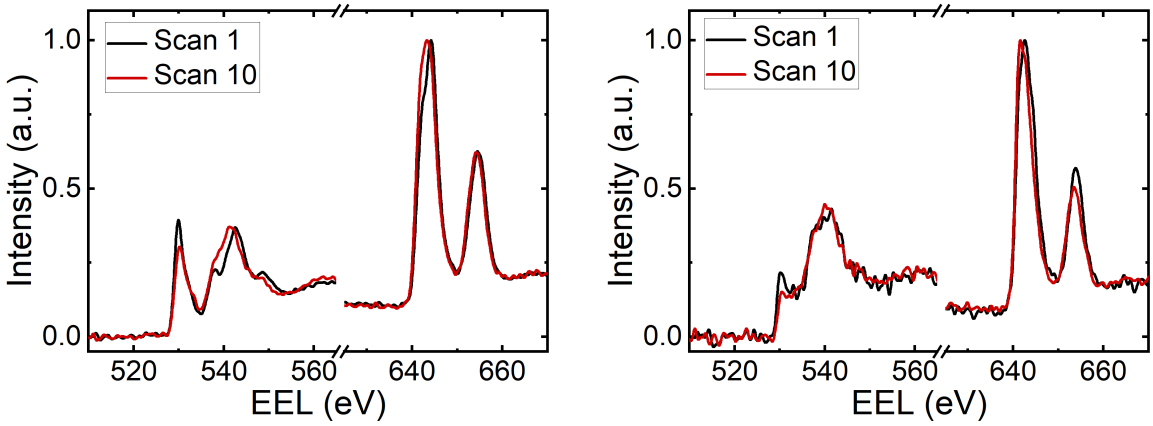

Figure 4.2.: (a): EEL spectrum of first and after ten repeated scans of the (a) core region of the same particle and of the shell region (b).

peak energy, and a lower Mn L_2 peak intensity. These changes can be interpreted coherently as Mn reduction. A detailed description of EEL spectrum interpretation with focus on Mn valence changes can be found in Section 3.3.2.

Mn valence values have been calculated using the O K-pre-peak - Mn L_3 distance for the core and shell of the particles of each scan (see also Section 3.3.3). Fig. 4.3b indicates Mn reduction when scanned repeatedly, which increases the e^- fluence. In case of the core, the Mn valence decreases monotonically with scanning, while the shell valence drops in the first four scans and stays relatively constant afterwards.

To exclude that contamination formation interferes with the Mn valence measurements, Fig. 4.3a shows an EEL O K- and Mn L-edge spectrum of the contaminated area close to the particle surface after the tenth scan. A strong oxygen K-edge peak is observed, which has its maximum intensity at 539 eV. No intensity is observed at the oxygen pre-peak position at 529 eV, and comparably small intensity at the Mn L_3 peak position at 642 eV. Absolute counts of the Mn L-edge are smaller by a factor of 25 (core) and 15 (shell) in the contamination region compared to spectra of the particle. That leads to the conclusion that contamination building up during the measurements will not affect the O pre-peak and Mn L_3 peak positions and therefore, has negligible impact on Mn valence measurements.

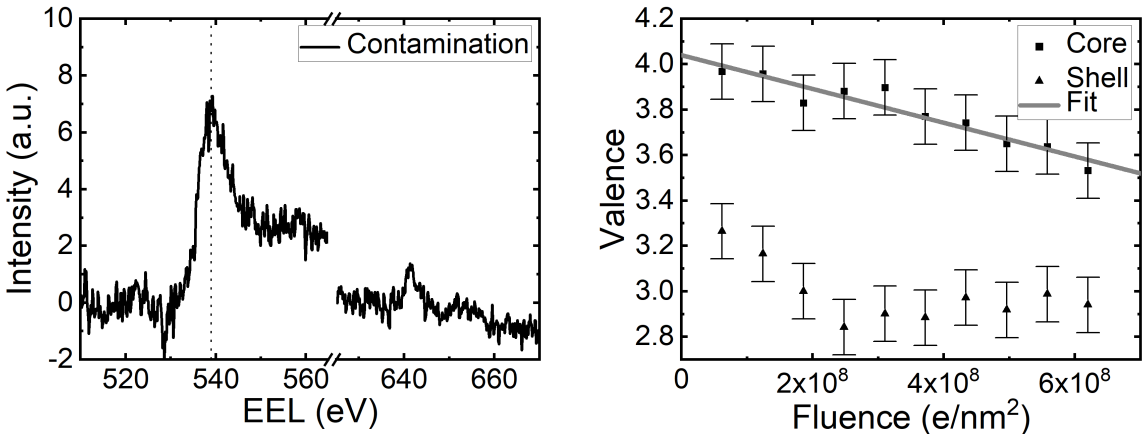

(a) (b)

Figure 4.3.: (a): EEL spectrum of contaminated area indicated in Fig. 4.1a showing a pronounced O K signal after 10 scans. (b): Mn valences from the particle core and shell regions in the course of 10 consecutive scans over an identical area. The electron fluence was calculated using the STEM beam current, the scan grid size and the high-loss illumination time. Mn valence values were evaluated using the O K pre-peak - Mn L_3 distance.

The applied electron dose during one scan is necessary to gain surface spectra with sufficient quality, which results in a total dose of 5×10^7 e/nm^2 in one scan. Systematic Mn reduction was observed previously in different Mn oxides at lower electron doses at 197 kV acceleration voltage. It was proposed that defects, domain boundaries and surfaces increase the vulnerability for electron beam imposed defects.[124] Since, the $LiMn_2O_4$ particles are single crystalline (see Section 4.2.2) a higher safe dose is expected than reported by Livi *et al.*[124] The safe dose of $LiMn_2O_4$ for EELS measurements is two orders of magnitude larger than the dose of a single scan in this work.[85] Degradation of the crystal structure at the surface of nanoparticles was observed at a much higher electron dose of 1.5×10^{11} e/nm^2.[85] Thus, it can be assumed that no damage is induced to the crystal structure under the experimental conditions. Over ten scans, the average Mn valence decrease per scan is 0.046 at core and surface, which is smaller than the uncertainty of the valence measurement itself (see Section 3.3.3). The overall decrease of the Mn valence after ten scans is 5 times larger than the standard deviation of valence measurements of different pristine particles (see Section 4.2). That indicates that the electron beam systematically lowers the Mn oxidation state. The core and shell valence differences between the first two scans are much smaller than the uncertainty of valence measurements.

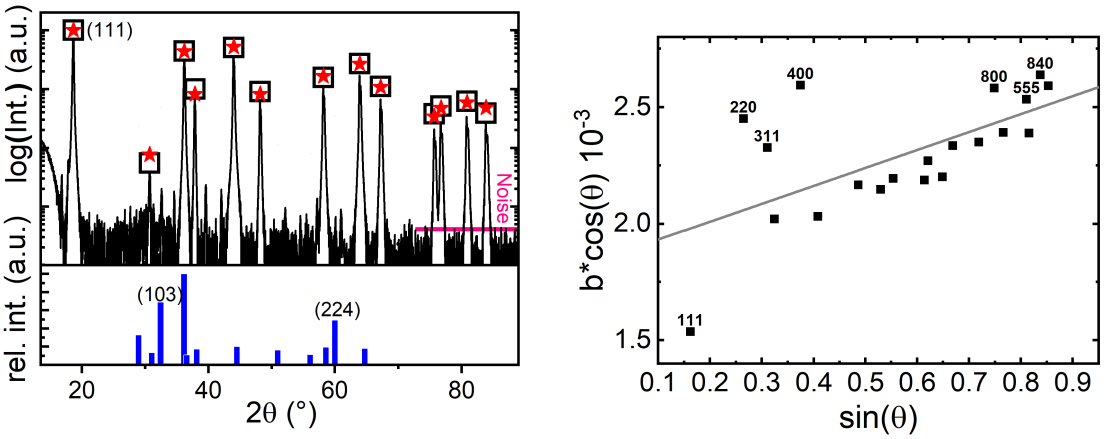

(a) (b)

Figure 4.4.: (a) XRD diffractogram of pristine $LiMn_2O_4$ with support of Thomas Brede. Peaks of cubic spinel are marked with red stars, whose y-axis positions mark the measured relative intensity. Expected peak positions and relative intensities for $LiMn_2O_4$ are marked with open squares. A magenta line indicates the noise level. The bottom inlet displays an expected peak pattern of tetragonal Mn_3O_4. (b) Williamson-Hall plot based on FWHM$= b$ values of peaks in (a) and the peak positions (θ) including a lin. fit. Values of FWHM and peak positions are in rad. Plane set indices (hkl) are indicated for points that deviate from the linear fit.

As a summary, multiple scanning at one location leads to contamination formation. It was ruled out, that contamination formation interferes with Mn valence measurements based on O pre-peak - Mn L_3 peak distances. Higher electron doses cause a systematic reduction of the Mn oxidation state over the whole particle starting with the second scan. A single particle can thus not be used for more than two scans. Otherwise, it is not possible to disentangle Mn reduction as a sample effect from electron beam induced variations.

4.2. Pristine Particles

The following section will focus on characterization of pristine nanoparticles with the nominal composition of $LiMn_2O_4$, as purchased from the manufacturer.

4.2.1. XRD

The crystal structure of pristine particles was measured using XRD. Main peaks in the $\theta - 2\theta$ XRD diffractogram (Fig. 4.4a) can be indexed as cubic spinel. A lattice parameter of $a = 8.234(2)$ Å was determined by peak fitting. This measurement was repeated with two years distance (see Fig. A.2) yielding to a lattice constant of $a_2 = 8.234(3)$ Å. That indicates that the crystal structure does not change when the particles are stored under atmosphere for longer time periods. The determined lattice constants are in good agreement with literature values for $Li_{1.03}Mn_2O_{4.05}$ (a =8.236 Å)[64] or $Li_1Mn_{1.94}O_4$ (a =8.235 Å),[74] but smaller than lattice constants that are reported for stoichiometric $LiMn_2O_4$ (a =8.242 Å).[56] Calculated peak intensities, using Vesta[84] (marked with black open squares), compare reasonably well with the integrated experimental peak intensity (red stars) after the background had been accounted for. The measured (220) peak intensity (at $2\theta \approx 31^\circ$ in Fig. 4.4a) exceeds the calculated value. The effect of replacing Li with Mn on the 8a tetrahedral sites leads to a strong increase in the (220) peak intensity, suggesting the presence of some tetrahedrally coordinated Mn in the nanoparticles.[20]

Additional unmarked peaks found in the X-ray pattern can be indexed as two cubic phases with a =8.603(3) Å and a =9.123(4) Å with a volume fraction smaller than 1 %, assuming similar structure factors as the cubic spinel phase. The peak positions were compared with data of a reference XRD library, but no matches with reported structures were found. It should be explicitly mentioned that the unmarked peaks are not consistent with tetragonal Mn_3O_4, which was reported to occur on $LiMn_2O_4$ particles and on thin film surfaces.[81–83,85,125] The expected peak positions and intensities of Mn_3O_4 are indicated below the XRD pattern in Fig. 4.4a. Peaks of a Mn_3O_4 phase are only discernible in the diffractogram, if the peak maximum exceeds the noise level of the measurement. The scattering, or integrated peak intensity is proportional to the material volume however, the height of the peak maximum depends as $1/x$ on the FWHM as well. As a first approximation, the upper limit of a Mn_3O_4 to $LiMn_2O_4$ volume ratio has been calculated using Eq. (3.10) by requiring that the intensity of the Mn_3O_4 (103) peak (which does not overlap with a $LiMn_2O_4$ peak) exceeds twice the noise level (0.04% of the $LiMn_2O_4$ (111) peak as indicated in Fig. 4.4a),which yields

$$\frac{V_{Mn_3O_4}}{V_{LiMn_2O_4}} \leq 0.08\% \cdot \frac{B_{111;LiMn_2O_4}}{B_{103;Mn_3O_4}}.$$

As a result, a maximum scattering volume share of 0.57% Mn_3O_4 is estimated. Using the Mn_3O_4 (224) peak results in a maximum volume share of 0.8%. The underlying values for the calculation based on Eq. (3.10) are given in Table A.1. This estimation assumes that the peak shape is similar to the $LiMn_2O_4$ peaks. However, a small crystallite size like one of thin surface layers leads to peak broadening and thereby a reduction of the peak maximum at identical peak intensity. Thus, the detection limit of very small Mn_3O_4 crystallites is higher due to Scherrer broadening. A crystallite size of 4 nm for example leads to FWHM 15 times larger than of the $LiMn_2O_4$ peaks. At identical scattering intensity, a larger FWHM results in a smaller peak maximum and thus, to a detection limit of 9% Mn_3O_4. As a result, presence of bigger crystallites of the tetragonal Mn_3O_4 phase can be excluded by this measurement, although a higher volume of very small tetragonal areas would be difficult to identify in the diffractogram. Presence of a thin layer of epitaxial Mn_3O_4 on particle surfaces can not be confirmed. The c axis has the biggest distortion in the Mn_3O_4 tetragonal spinel compared to the $LiMn_2O_4$ cubic spinel, a minimum tensile strain of 1.1% is necessary to fit a plane in Mn_3O_4-(a, b) direction to the cubic spinel. A Poisson ration of $\nu = 0.33$[126] would result in an expected compressive strain of 0.7%, and thus $c = 9.376$ Å The additional peaks cannot be explained by this structure.

Values of the average particle size and inhomogeneous strain were evaluated using the peak width b from fits (FWHM) via the Williamson-Hall method (see Eq. (3.13)). Each data point in Fig. 4.4b corresponds to one reflex in the diffractogram, and thus to one crystal plane set (hkl). Most data points follow a linear trend. At low and high reflection angles, however, deviations from a linear behaviour are observed. A broader FWHM of some reflexes can either be explained by smaller crystallite sizes in these directions or by a higher amount of inhomogeneous strain in these planes. Since the particles have preferential surface orientations[27], the resulting faceted shape might cause different average crystallite sizes in certain crystallographic directions. The indices (hkl) of the outlying reflexes, marked in Fig. 4.4b, do not indicate a systematic deviation of specific crystal plane sets. A crystallite size of $74(6)$ nm using the y-axis intercept and an inhomogeneous strain of 0.019(6)% using the slope was evaluated from the linear fit to all data points. If the outliers are not included in the fit, these values change to $81(4)$ nm for the crystallite size and 0.022(4)% for strain. Thus, the outlying lattice planes do not change the evaluated values by orders of magnitudes.

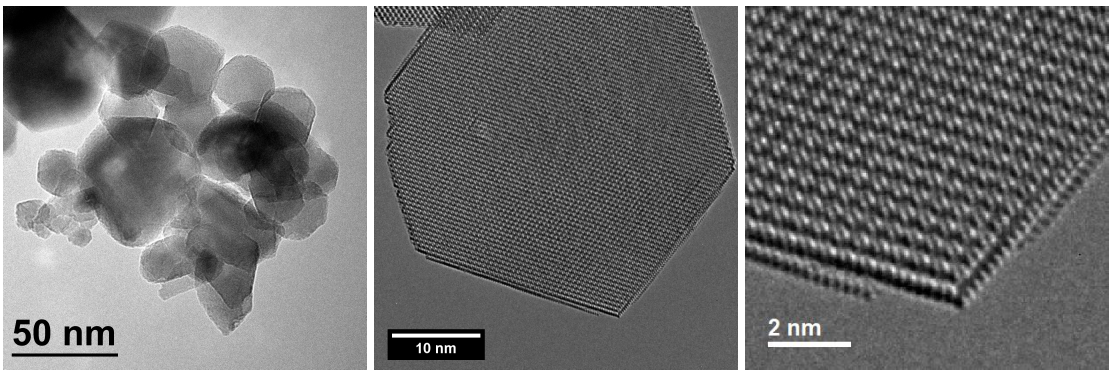

(a) (b) (c)

Figure 4.5.: TEM images of pristine $LiMn_2O_4$ nanoparticles. Agglomerate showing clearly faceted particles with differing sizes (a). High Resolution (HR)-TEM image of an exemplary particle (c). Magnified image of (b) showing atomic sized steps at the particle surface.

As a conclusion, these results show that the pristine material has the expected cubic spinel crystal structure, that no intensity of tetragonal Mn_3O_4 is detected within the resolution limits, and that no other additional identifiable phases were detected. Inhomogeneous strain was estimated to be smaller than 0.1%.

4.2.2. TEM Imaging

TEM images of pristine particles (Fig. 4.5) show that they are partially faceted single crystals with diameters ranging from 20 nm to 140 nm. Larger particles show more faceted shapes than the smaller particles and are mainly truncated octahedrons and some truncated rhombic dodecahedrons. High resolution TEM images of Fig. 4.5b confirm that the particles are single crystalline up to the surface. Surfaces are sharp and exhibit atomic scale steps (Fig. 4.5c). Single particles with diameters larger than 400 nm were occasionally found. The diameter of 140 particles was measured in overview TEM images as plotted in Fig. 4.5a using two perpendicular measures on each particle. A mean diameter of 55(20) nm and a most frequent diameter of 45 nm were calculated by fitting a log-normal distribution to the size distribution plotted in Fig. 4.6. Weighted by the particle volume, a mean diameter of 62(66) nm is found.

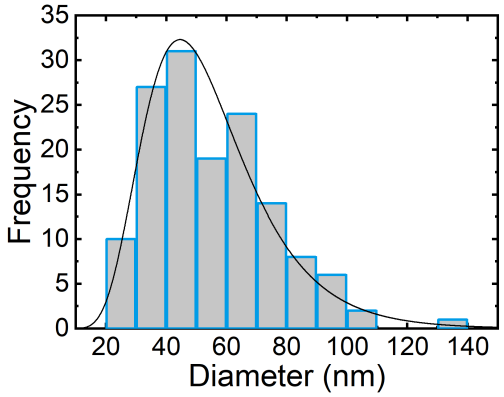

Figure 4.6.: Size distribution of pristine $LiMn_2O_4$ particles measured in TEM overview images as plotted in Fig. 4.5a, including a fitted log-normal distribution. The particle diameter is evaluated as the average length of one particle measured in two directions.

4.2.3. STEM-EELS

STEM-EEL spectrum images were obtained from 12 different pristine particles that were selected for their TEM transparency and position over holes in the TEM grid carbon layer (Fig. 4.7a). The particles had different diameters, with a relative maximum thickness t/λ between 0.18 and 0.81. All investigated particles show clear differences when EEL O K- and Mn L-edge spectra are compared from surface and core regions.

Representative spectra are shown in Fig. 4.7b where the following systematic differences are apparent in surface spectra relative to core spectra: smaller O pre-peak intensity (529 eV) compared to the second O 4sp peak (ca. 540 eV); shift to lower energies of the O pre-peak (Fig. 4.8d); smaller O 4sp peak compared to the Mn L_3 peak at 640 eV; shift to lower energies of the Mn L_3 peak maxima (Fig. 4.8c); increase of the L_3/L_2 intensity ratio from $L_3/L_2 = 2.13(5)$ to $L_3/L_2 = 2.63(17)$ (Fig. 4.8e); less pronounced low energy shoulder on the Mn L_3 peak. The plotted EEL spectra are a sum of multiple single spectra from core or shell. EEL low-loss spectra in Fig. A.3 show only a weak Mn and Li signal. As a tendency, a higher Mn/Li intensity ratio is found in core spectra.

These changes can be interpreted coherently as a reduction of the Mn oxidation state in the surface region relative to the core (see Section 3.3.2). Fig. 4.8e and Fig. 4.8f display measures that have been established to calculate Mn valences.[96,98,101] Maps over a representative particle of these different measures illustrate the core-shell behaviour in

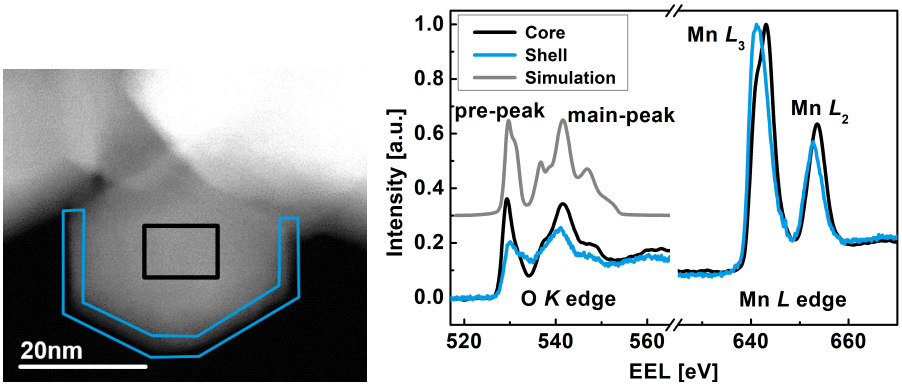

(a) (b)

Figure 4.7.: (a) STEM image of an exemplary pristine $LiMn_2O_4$ nanoparticle. Regions indicate areas where core and shell spectra of (b) were extracted. (b) Averaged O K and Mn L spectra from core and shell of one particle. The intensities are normalized by the Mn L_3 height. A simulated O K spectrum for $LiMn_2O_4$ is included for comparison.

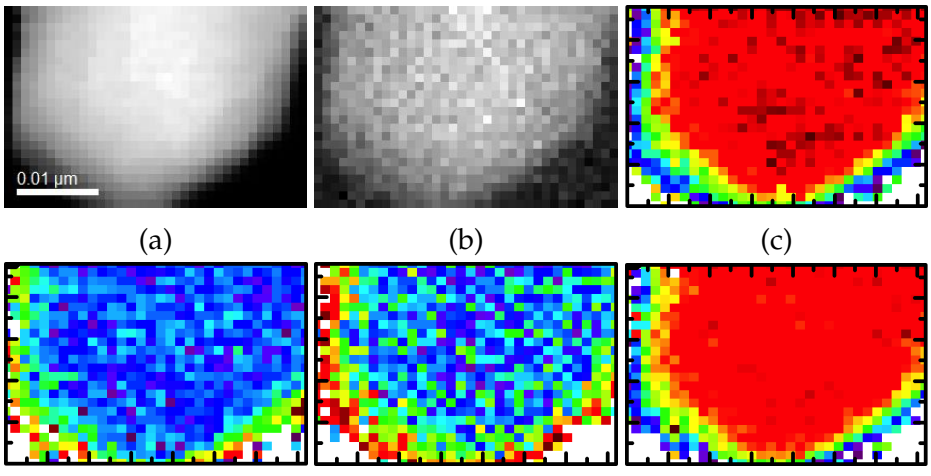

(a) (b) (c)

(d) (e) (f)

Figure 4.8.: Exemplary maps derived from STEM-EELS measurements of pristine particles. (a) High Angle Annular Dark Field (HAADF)-STEM image from a particle with maximum relative thickness $t/\lambda = 0.36$, (b) Relative thickness map of particle in (a), (c) Mn L_3 peak position map (colour bar range violet to red: 640.7-643.4 eV), (d) O pre-peak position map (528.9-532.1 eV), (e) L_3/L_2 intensity ratio map (1.9-3), (f) Map of O pre-peak and Mn L_3-peak energy difference (110-114.6 eV).

terms of Mn oxidation state and allow quantifying the trends that have been observed in summed spectra (Fig. 4.7b). Comparing the noise level in Fig. 4.8e and Fig. 4.8f confirms the choice of the O pre-peak to Mn L_3 peak distance as method for Mn valence evaluation (see also Section 3.3.3). Fig. 4.20 (a) shows the resulting Mn valence. The maps allow estimating the thickness of the shell layer as 2 nm to 4 nm. Core and shell oxidation states of single particles were determined from summed core and shell spectra, as shown exemplary in Fig. 4.7b. An average core oxidation state of $Mn^{3.77(7)+}$ and a shell oxidation state of $Mn^{2.91(21)+}$ were determined. Approximating the particles as spheres with average diameter of 55 nm, a 2 nm to 4 nm thick shell contributes to the total particle volume by 12 % to 22 %.

The evaluated shell values are independent of the particle thickness, however very thin particles have a smaller core valence. Even at measurement points at the particle core, transmitting electrons will interact with the shell layers. In the preceding master thesis,[62] it was shown, that this shell contribution is of importance up to a total particle thickness of $t/\lambda = 0.36$.[62] Values of thinner particles were discarded from the Mn valence evaluation of the core valence.

Valence measurements of different single particles, which are nominally in the same state, differ by a maximum of 0.23. The two core spectra of particles with highest and lowest measured Mn oxidation state spectra are plotted in Fig. A.5. This allows estimating to what extent variations of spectra from different particles can be expected. The biggest apparent changes are changes in the O pre-peak height and a change in the intensity distribution in the Mn L_3 peak. A shift of the Mn L edge to different energies is not observed. Especially at the shell, a comparably large standard deviation is observed if valence measurements from different particles are compared. These variations can either be induced by variations in the shell structure or by the method. The particle orientation was random and the exact geometry, shape, and thickness with respect to the electron beam varied from particle to particle. Thus, it is not straightforward to identify the shell regions in EELS maps and to guarantee that no core region intensity contributes to shell spectra. Hence, it is likely that the observed variance of shell valence measurements of 0.2 is caused by experimental difficulties in acquiring pure core or shell spectra.

The measured average Mn oxidation state of particle cores deviates with $Mn^{3.77(7)+}$

from the expected value of $Mn^{3.5+}$ for stoichiometric $LiMn_2O_4$. This means that either the particle cores are off stoichiometry or that the Mn valence calibration[101] is not accurate for $LiMn_2O_4$. Therefore, a simulated spectrum of $LiMn_2O_4$, which has been provided by Marco Eckhoff, is plotted next to a measured core spectrum in Fig. 4.7b. The energy differences of peaks and shoulders agree well with the measured spectrum however, a closer comparison finds that the pre-peak intensity compared to the O 4*sp* peak is higher in the measured spectrum. This points out that particle cores are oxidised compared to expected $LiMn_2O_4$.

In summary, STEM-EELS experiments show, that a core-shell structure exists in the characterized pristine $LiMn_2O_4$ nanoparticles in terms of the Mn oxidation state. In a 2 nm to 4 nm thick shell, Mn is significantly reduced, whereas it is found to be oxidized in the core compared to the expected Mn oxidation state $Mn^{3.5+}$.

4.2.4. XPS

Pristine powder has been investigated with XPS, which allows identifying which elements are present in the sample. The fine structure of transition metal peaks allow drawing conclusions about chemical states.
An overview spectrum of pristine powder is plotted in Fig. 4.9a. All peaks in the spectrum can be explained with the element set [Mn, O, Li, C]. The detection limit of trace elements in a O matrix is smaller than 0.3 at.% for elements with atomic number $Z > 4$, in a Mn matrix it is about 1 at.% for $Z < 17$ and smaller than 0.3 at.% for $Z < 17$.[111] Thus, possible contamination with transition metals is smaller than 0.3 at.%. Presence of a high carbon amount is expected because of the sample preparation routine for powder, where particles were embedded in a carbon tape (see Section 3.2.2).

The Mn/O stoichiometry was determined using Mn 2*p* and O 1*s* intensities. Using the oxygen 1*s* peak is not trivial, since part of the signal arises from the oxygen containing carbon tape that supports the powder. A spectrum of pure carbon tape shows a single O 1*s* peak at 532 eV and carbon 1*s* peaks at 285 eV (Fig. A.4a). With $LiMn_2O_4$ powder on carbon tape, two prominent peaks are found in the oxygen 1*s* spectrum in Fig. 4.9b. The 1*s* peak energy of oxygen bound to manganese (O-Mn) is found at approximately 530 eV, independent of the Mn/O ratio,[127] whereby the component at 532 eV can be

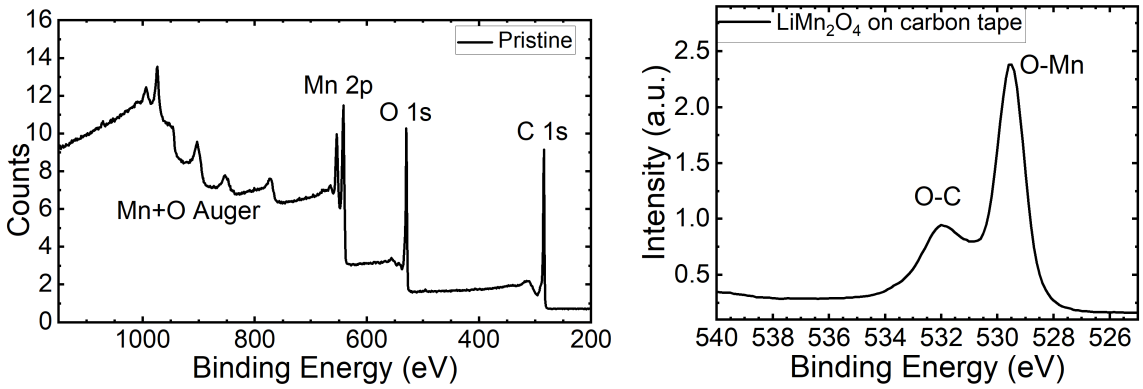

(a) (b)

Figure 4.9.: Overview XPS spectrum of pristine $LiMn_2O_4$ powder in (a) and spectrum of the O 1*s* peak with intensity contributions of O-Mn and O-C bonds in(b).

ascribed to O-C bonds, which agrees with the O peak position of pure carbon tape. This allows to separate the intensity contributions to the oxygen 1*s* peak and to subtract the O-C signal from the total O intensity. As a result, a Mn/O stoichiometry of $Mn_{2.30(1)}O_4$ was calculated, which indicates a Mn excess. The Mn to Li ratio was determined by peak fitting of the Mn 3*p* peak as well, where the Li peak appears as a shoulder at 55 eV in Fig. 4.16b. The determined Li/Mn ratio of Li/Mn= 1.2(4) has a comparably high uncertainty. Stoichiometry determination by XPS is considered being precise but not accurate.[128] A test with a silver reference sample showed that stoichiometry variations of up to 4%$_{at}$ can be expected, which is much smaller than the difference of the measured Mn/O ratio to the expected value of Mn/O= 2. Due to the high surface sensitivity of this method with a probing depth of about 6 nm (see also Section 3.3.4), Mn enrichment is detected in the materials surface layers.

Both, the Mn 3*p* (Fig. 4.16b) and 2*p* (Fig. 4.16a) peak, have a well pronounced fine structure, which is ascribed to the presence of different Mn oxidation states.[129] Comparison with literature data[127] shows that an unexpected shoulder at low binding energy is present in the pristine samples at 48 eV and 641 eV respectively. The energy position of the low binding energy shoulder in the Mn 3*p* spectrum agrees with values reported for Mn^{2+} in spinels.[129] This is also the case for the Mn 2*p* line, where intensity in the same energy range is attributed to the presence of Mn^{2+}.[130,131]

An average Mn oxidation state of 3.2(3) was estimated using the Mn 2*p* peak centroid

and the calibration curve presented in Section 3.3.4. This is lower than the expected value of 3.5 which agrees with the presence of Mn^{2+}, a species that is not expected in stoichiometric $LiMn_2O_4$ spinels.

As a summary, these measurements indicate, that the pristine sample material is free of contaminants within ca. 1at.% but has a significantly higher Mn/O ratio in the first 6 nm below the surface. In addition, analysis of the fine structure of Mn peaks shows that Mn^{2+} is present unexpectedly, the average Mn oxidation state is found to be lower than the expected $Mn^{3.5+}$.

4.3. Delithiated Particles

Varying the lithium content is one way to systematically change the Mn oxidation state in $LiMn_2O_4$. In the following, it will be presented how electrochemical delithiation affects the particle structure.

High-resolution TEM images of delithiated particles in Fig. 4.10 show that they have a facetted shape, but that the surface roughness increased. Either delithiation lead to a change of surface crystallinity or the particles are wrapped in residuals from the battery cell used for delithiation. In Fig. 4.10a and Fig. 4.10c, structures are displayed that are absent in pristine particles and resemble carbon nano onions.[132] These are presumably remainders of carbon powder which is added to $LiMn_2O_4$ during assembly of electrodes for delithiation. An image of a particle surface with higher magnification in Fig. 4.10c shows that the crystal structure does not differ within a 1 nm distance to the surface. As for pristine particles, the observed lattice fringes continue all the way from the centre to the surface and thereby indicate that the particle is single crystalline. That an atomic contrast is not discernible within 1 nm at the surface can be either attributed to surface amorphization or due to residuals of the battery cell which cover the surface.

STEM-EELS experiments have been performed on two sets of delithiated particles with nominal Li contents of $x = 0.25$ and $x = 0.64$ in $Li_xMn_2O_4$. The Li content x was determined using the observed linear decrease of the lattice constant under delithiation.[32,62] An according change of the average Mn oxidation state was checked by Max Baumung measuring the Mn K-edge position using XAS.[34]

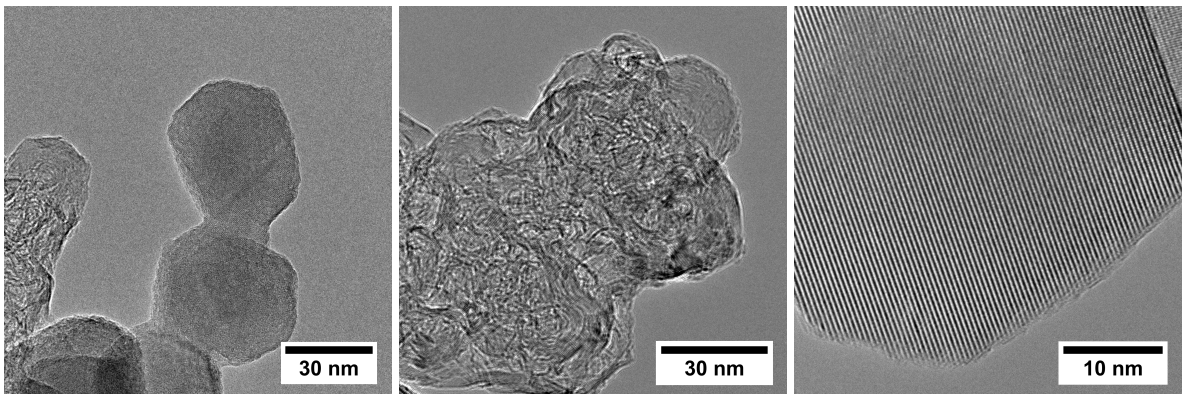

(a) (b) (c)

Figure 4.10.: TEM images of $Li_xMn_2O_4$ particles after delithiation in a battery cell showing that (a) particles are facetted but have higher surface roughness, (b) structures with shapes of carbon nano onions[132] are found and (c) that the particles are single crystalline up to a 1 nm thick region at the surfaces.

The particles are still faceted after delithiation as can be seen exemplarily in Fig. 4.11. Nonetheless, Fig. 4.11b and Fig. 4.11c show that the surface contrast is not as sharp as in the pristine case and that clear particle silhouettes are hard to see at all. This will be explained by remaining battery cell chemicals (see Fig. 4.14).

Valence measurements of particle cores (see Table 4.1) and core EEL spectra (see Fig. 4.12) indicate a significant increase of the Mn oxidation state after delithiation. The spectra have been aligned by the Mn L_3 peak position for better comparison. Compared to the spectrum of pristine $LiMn_2O_4$, delithiation results in an increased O pre-peak intensity at 529 eV and in a shift of this peak to lower energies compared to the Mn L_3 peak. The Mn L_3 peak has a less pronounced shoulder at low EEL and a smaller L_3/L_2 intensity ratio, which is expected for Mn oxidation.[96,98,101]

Shell valence measurements do not show an expected increase of the Mn oxidation state after delithiation. An exemplary Mn valence map in Fig. 4.13 shows that a shell with reduced Mn oxidation state, similar to pristine particles, is still present. Valence measurements in shells do not show a significant change of the Mn oxidation state however, the standard deviation of the average is with 0.2 quite high (see Table 4.1). Shell spectra of delithiated particles in Fig. 4.12b show that the O pre-peak intensity decreases relative to the Mn L_3 peak, but that no shift of the pre-peak position is ob-

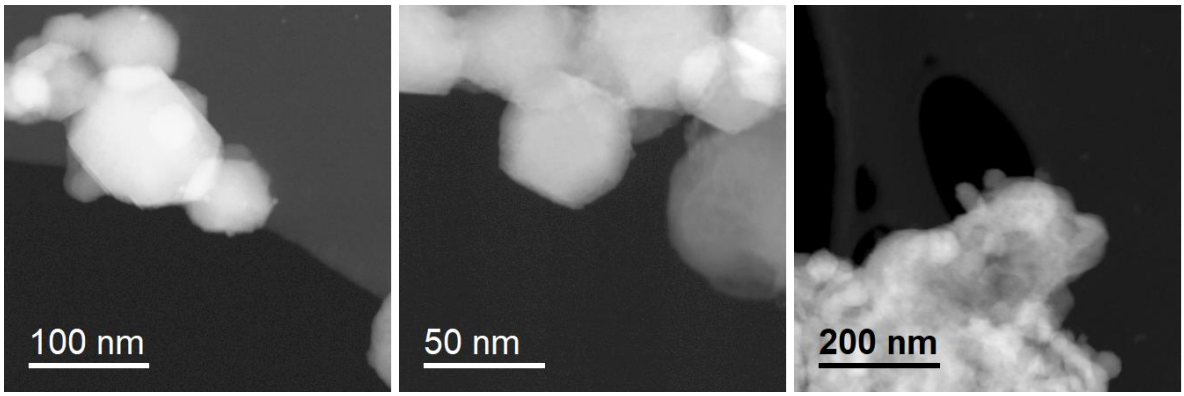

(a) (b) (c)

Figure 4.11.: Exemplary STEM images of delithiated particles with Li content of x=0.25 (a,c) and x=0.64 (b). Images (a) and (b) show that the particles have a faceted shape. (c) shows an agglomerate of several particles in a contaminant.

Sample	Mn valence core (EELS)	Mn valence shell (EELS)	Mn valence Av. (EELS)	Bulk Valence (XAS/XRD)
x=1	3.72(6)	2.9(2)	3.6	3.51
x=1 OER	3.78(8)	3.5(2)	3.73	3.72
x=0.64	3.86(8)	3.0(2)	3.69	3.68
x=0.25	4.04(7)	2.9(2)	3.82	3.88

Table 4.1.: Comparison of evaluated Mn valence values of samples in different lithiation state and after catalysing the OER. The averaged EEL Mn valence was calculated using a model that assumes a shell volume fraction of 0.19 (see Eq. (4.1)). The corresponding measurements of the average Mn valence by XAS are reported by Baumung[34].

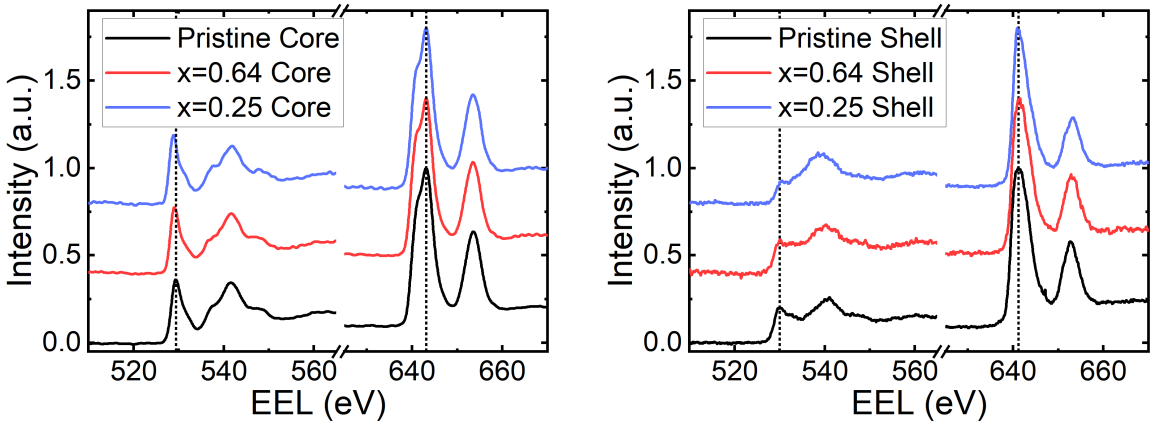

(a) (b)

Figure 4.12.: EEL core spectra of pristine and delithiated particles in different lithiation states. The energy axis was shifted so that Mn L_3 peaks overlap as highlighted by a vertical line at 642 eV in (a) All spectra are normalized by the maximum intensity. A second line is drawn at the pristine pre-peak position of 529 eV in (a) to point out the observed shift of the O pre-peak position. The corresponding shell spectra are plotted in (b).

served. A smaller O pre-peak would indicate further Mn reduction (see Section 3.3.2), but has to be considered as an artefact of spectrum normalization by the Mn peak height and apparent contamination by battery residuals. This statement will be elaborated in the following paragraphs.In addition, the Mn L_2 peak height decreases relative to the Mn L_3 peak maximum. However, the calculated L_3/L_2 intensity ratios from shell spectra of delithiated samples which are an alternative measure for the Mn oxidation state[98,101] do only show variations from the value of pristine particles that are within the standard deviation of single particles measures. A decreasing L_3/L_2 intensity ratio indicates reduction and not oxidation.[98,101]

As depicted in Fig. 4.11c, a locally varying amount of contamination has been detected in delithiated samples. The particles have been delithiated in a battery cell which contains $LiPF_6$ with $C_3H_6O_3$ as electrolyte and carbon black to improve conductivity.[34] These chemicals or degradation products partially cover the surfaces of the investigated particles. An XPS overview spectrum of $x = 0.25$ particles is shown in Fig. 4.14, where signals from F and P are observed. Mn $2p$ and $3p$ spectra could not be evaluated in detail because of artefacts, presumably induced by charge accumulation during these measurements.

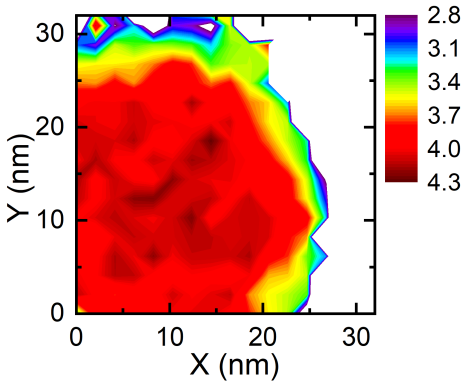

Figure 4.13.: A Mn valence map derived from EELS measurements of a delithiated particle with Li content $x = 0.25$ shows that reduced shell is still present after delithiation.

To rule out that these residuals affect the Mn valence determination, Fig. 4.15a shows a spectrum of a contaminated region where no $Li_xMn_2O_4$ particle was discernible. In contrast to the contamination that grew under the electron beam influence (see. Fig. 4.3a), an unexpected Mn signal is found in the spectrum in Fig. 4.15a. The absence of the O pre-peak indicates that this Mn signal does not come from Mn in $Li_xMn_2O_4$. Since $LiMn_2O_4$ is the only possible source of Mn in the battery cell, it has to be assumed that Mn leached out of the particles during delithiation. This process has been ascribed to Mn^{3+} disproportionation in the presence of water or acids, which results in Mn^{2+} dissolution,[83,133] or by dissolution of tetrahedral Mn^{2+} defects.[82] The high observed L_3/L_2 intensity ratio and the low Mn L peak positions are an indication that dissolved Mn is found in a lower oxidation state than in particle shells. The Mn L_3 peak maximum is shifted by 0.2 eV to lower energies compared to the shell spectra in Fig. 4.12b.

When particles are covered in residuals, dissolved Mn will contribute to some extent to the shell Mn *L* spectrum and might induce peak intensity and position changes that might lead to misinterpretation of the $Li_xMn_2O_4$ shell oxidation state. In order to estimate how the Mn valence calculation in particle shells is affected, Fig. 4.15b evaluates how delithiated shells deviate from pristine ones. Therefore, a linear combination of the pristine shell spectrum (ratio: 0.63) with the contamination spectrum Fig. 4.15a (ratio: 0.37) is compared to a shell spectrum of the $x = 0.25$ sample. The combined spectrum reproduces the O pre-peak intensity, the Mn L edge shape and the L_3/L_2

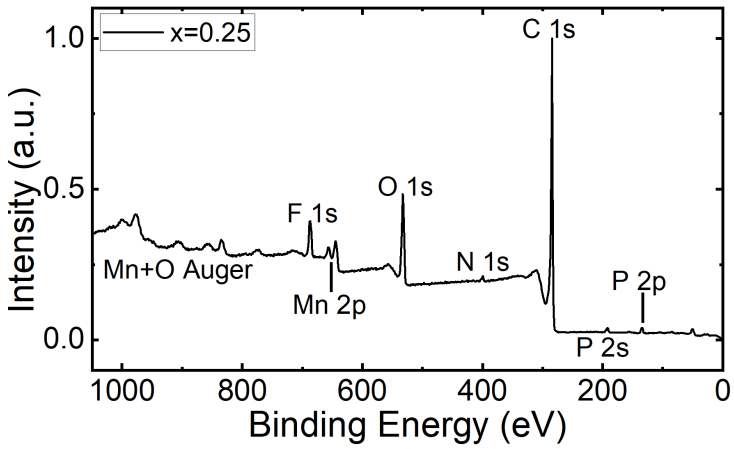

Figure 4.14.: XPS overview spectrum of delithiated particles with Li content $x = 0.25$ showing F and P peaks which are interpreted as residuals of the battery electrolyte used for delithiation. Unmarked peaks are less intense transitions of Mn and O.

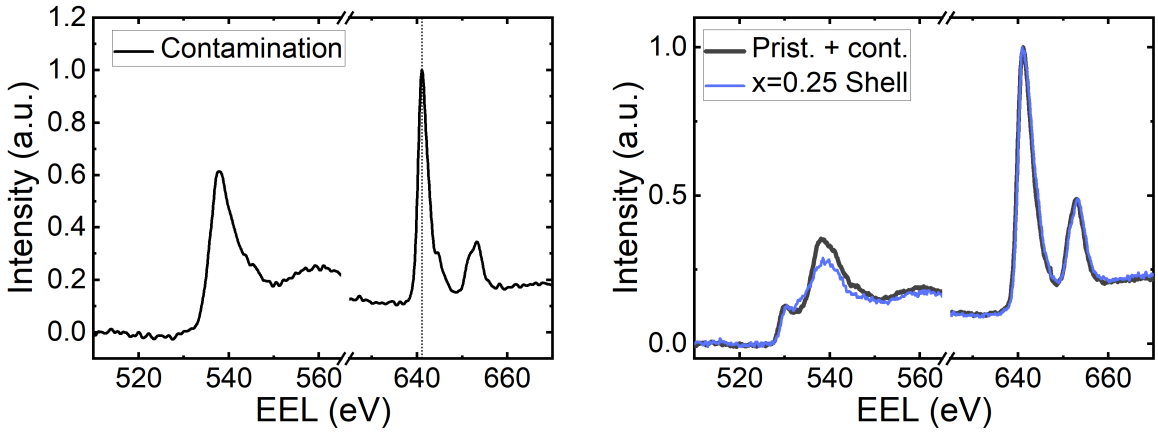

(a) (b)

Figure 4.15.: EEL spectra of area from contamination in delithiated sample set where no particle contrast is apparent (a). Shell spectrum of a delithiated particle compared with a linear combination of the spectrum in (a) with a shell spectrum of a pristine particle.

peak height of the delithiated spectrum well. Differences in the two spectra are comparable to the differences between two pristine particles, which are nominally identical (see. Fig. A.5). A lower intensity of the oxygen edge at 539 eV in the delithiated sample can be explained by a smaller amount of oxygen containing contaminants on the particle, compared to the spectrum of the contaminated area. That the combination of a pristine shell spectrum and of contamination is able to reproduce the shell spectrum of a delithiated sample is a clue that particle shells do not oxidise when the whole sample is delithiated. However, it can not be stated definitely that the shell structure and valence is unchanged by delithiation since spectrum shape and Mn valence calculation can be (partially) affected by Mn containing contaminants. Nonetheless, shell Mn valence values do still differ significantly from the core. Although a change of the shell valence by 0.2 can not be resolved due to the large standard deviation of measurement points, it can be stated that a reduced shell is still present after delithiation. This aligns well with literature reports that show that delithiation leads to formation of a reduced surface layer by incorporating tetrahedral Mn defects.[81,82,85]

Based on the core-shell geometry, which is still present after delithiation, average Mn valence values have been calculated and compared to XAS measurements in Table 4.1. The average EELS based Mn valence V_{EELS} was calculated as the average of the core and shell valence measurements weighted by the volume shares:

$$V_{EELS} = \rho_{Shell} \cdot V_{Shell} + (1 - \rho_{Shell}) \cdot V_{Core}. \tag{4.1}$$

The parameter ρ was optimized to minimize the deviation of averaged EELS valence measurements from XAS ensemble measurements. The optimum was found for a shell volume share of $\rho_{Shell} = 0.19$, which agrees well with the estimated shell volume share of 0.12 , to 0.22 , based on the particle geometry. Application of this model gives reasonably well agreements with the average valence measurements by XAS.

As expected, Mn oxidation is detected after delithiation in particle cores. The measured core valence values exceed the average values, which were derived from XAS and XRD measurements by Baumung[34]. However, Mn valence measures of particle shells do not illustrate signs of oxidation. Instead, the measured average value of the shell Mn oxidation state after delithiation lies well within the standard deviation of the single measurement points. The uncertainty of measurements is with 0.2 quite high so that

oxidation state changes of this size can not be resolved That means that it can not be stated if the shell Li content and/or Mn oxidation state changes according to the bulk. Nonetheless, a clear difference between core and shell spectra and Mn oxidation state is observed and a core-shell structure with reduced shell still exists after delithiation. Average Mn valence values that were calculated using EELS data and the core-shell model with a shell volume fraction of 0.19 both agree well with corresponding average measurements by XAS.[34]

4.4. Particle Structure Evolution after OER Catalysis

Pristine $LiMn_2O_4$ was used as OER catalyst in RRDE experiments.[91] The following section will cover experiments that resolve if and how the material changes during OER experiments.

4.4.1. XPS

XPS spectra have been taken from an identical electrode before and after catalysing the OER using Cyclic Voltammetry (CV) in ten cycles. XPS measurements have been performed in a time frame of two hours after OER catalysis. An overview spectrum in Fig. A.4b of a cycled electrode shows residuals of the electrolyte used for CV (NaOH). The Na 1s peak at 1070 eV and Na Auger peak at 495 eV clearly indicates that a significant amount of Na is detected on the surface of the electrode. Comparison of the Na and Mn peak intensities allows estimating the ratio of Mn/Na$\approx$ 2.

After electrochemical cycling, the fine structure of Mn 2p (see Fig. 4.16a) and 3p (see Fig. 4.16b) peaks changes. A shoulder that is present in pristine material at low binding energies, which was interpreted as Mn^{2+} signal in Section 4.2.4, is reduced in intensity, so that the centre of gravity of the Mn $2p_{3/2}$ peak at 642 eV shifts by 0.6 eV to higher binding energies, thereby indicating that Mn is oxidised after OER. Using Eq. (3.6), a valence shift by 0.63 to $Mn^{3.86+}$ is detected. The high amount of C and Na in the sample prevents to determine the Mn/O stoichiometry, since intensity contributions of Mn, Na and C coordinated with O cannot be deconvoluted out of the O 1*s* peak.

Repeating the experiment after the sample was kept in air for approximately 5 d shows that the just described trends are partially reversed, as can be seen in Fig. 4.17. The

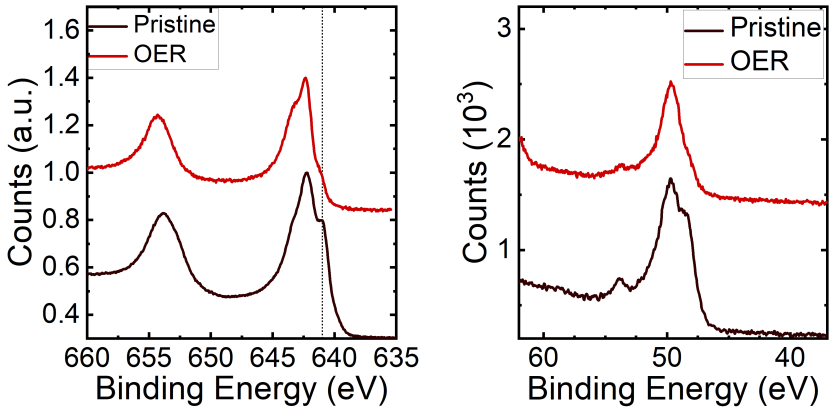

(a) (b)

Figure 4.16.: XPS Mn $2p$ spectrum of pristine and electrochemical cycled $LiMn_2O_4$ powder (a) and of the Mn 3p region of (b).

low energy shoulder at the Mn $2p_{3/2}$, which was ascribed to Mn^{2+}, increases in intensity compared to the measurement conducted within 2 h after OER catalysis. The peak centroid shifts to lower binding energies by 0.2 , thereby indicating Mn reduction to $Mn^{3.64+}$. That means that pristine particle surfaces, which oxidized directly after catalysing the OER, partially return to a more reduced state.

Surface sensitive XPS measurements on pristine particles show that the amount of Mn^{2+} is smaller after OER catalysis and that the average Mn oxidation state is increased. If the sample is stored in air, these changes partially reverse on a timescale of days.

4.4.2. STEM-EELS

In addition to the XPS ensemble measurements of the catalyst behaviour under OER catalysis, imaging and spectroscopic measurements have been performed in the TEM that allow to follow the structure evolution with high spatial resolution.

Eight particles have been studied post-mortem after OER catalysis, out of which two particles exhibited cracks and increased surface roughness (see Fig. 4.18). Six out of eight particles display systematic changes of shell EEL spectra (see Fig. 4.19b), while core spectra remained unchanged compared to pristine particles in all cases (see Fig. 4.19a). After electrochemical cycling, apparent differences between core and shell spectra are

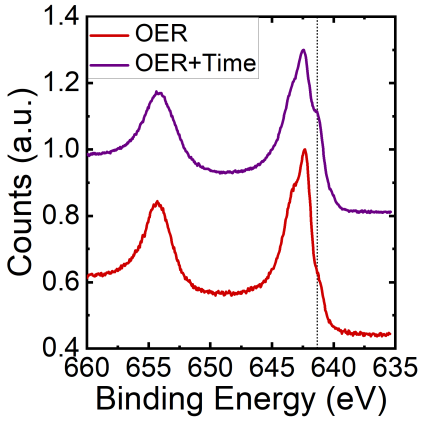

Figure 4.17.: XPS Mn 2*p* spectrum of pristine $LiMn_2O_4$ powder measured 2 h (red) and 5 days (purple) after catalysing the OER.

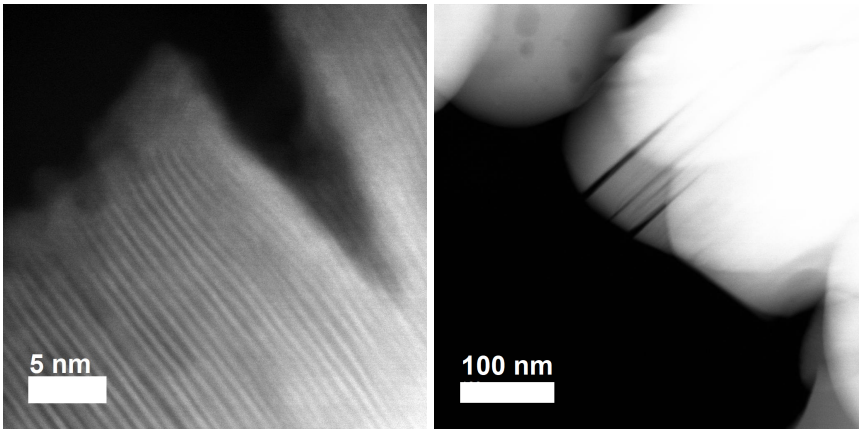

(a) (b)

Figure 4.18.: HAADF-STEM images of LiMn2O4 particle surfaces after catalysing the OER showing cracks and roughened surfaces.

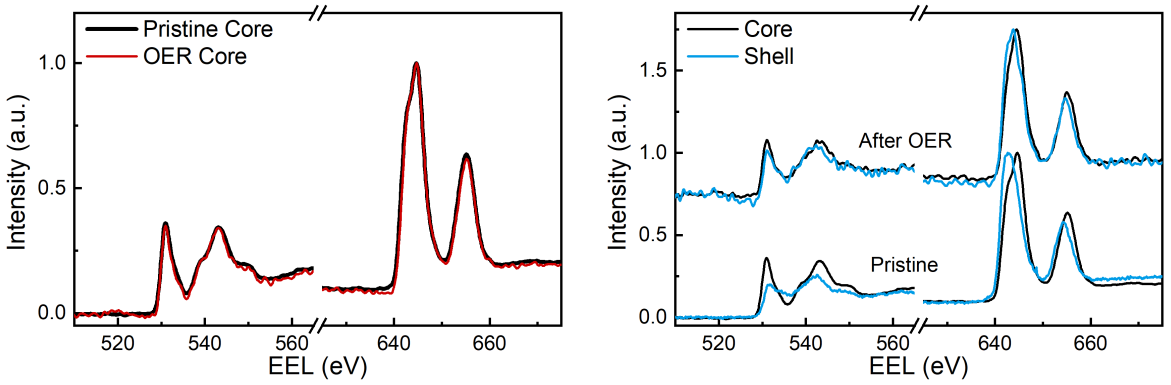

(a) (b)

Figure 4.19.: STEM-EEL O K and Mn L edge spectra of representative core and shell regions of the OER cycled material compared with the pristine case. Core spectra are plotted in (a) showing that el. chem. cycling does not alter the core electronic structure, while (b) shows that the surface spectra of cycled particles change compared to pristine material.

diminished. The shell O pre-peak intensity at 529 eV is increased in particle shells, whereas the intensity at 535 eV, that has been ascribed to tetrahedral Mn (see Fig. 5.4), decreases. That is concomitant with a shift of the Mn L_3 maximum to higher energies, and an increased Mn L_2 peak intensity relative to the L_3 peak, all of which indicate an oxidized shell Mn oxidation state after OER catalysis (see also Section 3.3.2).

The average shell Mn valence of particles exhibiting surface oxidation increased from $Mn^{2.9(2)}$ in a pristine state to $Mn^{3.5(2)}$ after OER, while the bulk oxidation state does not change within the experimental uncertainty by the standard deviation of single measurements (Pristine: $Mn^{3.72(6)}$; after OER: $Mn^{3.78(8)}$. Although, the uncertainty in shell Mn valence determination is with 0.2 comparably high the measured shell valence increase of 0.6 is three times higher than the standard deviation. An influence of the shell Li content on the Mn oxidation state change cannot be studied because of the noise level in the EEL low-loss spectra (see Fig. A.6).

That two particles did not show surface Mn oxidation, opposed to the general trend, can be explained with the known heterogeneous activity of composite electrodes. A poor electrical connection or limited access to the electrolyte can hinder that all particles contribute to the catalytic process.[134]

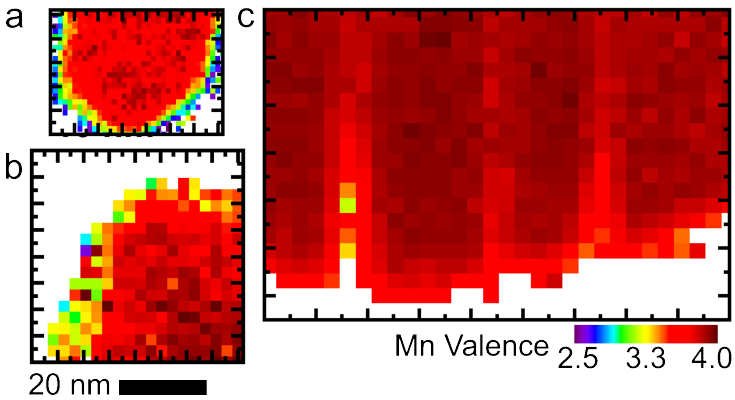

Figure 4.20.: Mn valence maps of representative particles in pristine state (a), after contact with NaOH containing electrolyte for 5 min (b) and after catalysing the OER in ten cycles (c). Maps are based on STEM-EELS spectrum images, the valence values have been evaluated at each pixel out of the O pre-peak Mn L_3 peak distance. Note the different map and pixel sizes.

Oxidation of Mn in particle shells can be illustrated in valence maps. Out of a STEM-EELS spectrum image, the Mn valence values can be plotted with spatial resolution across representative particles (see Fig. 4.20). Comparison with a pristine particle (Fig. 4.20) shows that the Mn valence gradient at particle surfaces is much smaller after OER (Fig. 4.20 (c)). In addition, a map of a non cycled particle is presented, that has been immersed in NaOH containing electrolyte (pH13) as used for RRDE experiments (Fig. 4.20(b)). It shows that a reduced surface layer still exists after 5 min of electrolyte contact. After contact with the electrolyte, an average Mn valence of $Mn^{3.04(18)}$ was measured at the surfaces, which is within the uncertainty of pristine particle shells. The core valence of $Mn^{3.75(8)}$ agrees well with the values of pristine and cycled states, thereby indicating that both core and shell electronic structures are unaffected by electrolyte contact.

Based on the finding that shell EEL spectra contain less intensity of tetrahedral Mn after OER catalysis, and that the shell oxidation state of Mn is increased by 0.6 to $Mn^{3.5+}$, it can be assumed that tetrahedral Mn leached out of the shell. This would lead to the composition of $Li_{0.5}Mn_2O_4$ with an expected Mn oxidation state of $Mn^{3.75+}$, which is higher than the measured value. A possible explanation is that Li from the core (partially) occupies the empty tetrahedral sites, or that tetrahedral Mn is not fully leached out.
Summarized, using $LiMn_2O_4$ nanoparticles as OER catalyst induces structural changes

to particle shells. Shell oxidation of Mn has been detected by STEM-EELS measurements that coincide with the finding of XPS that the Mn^{2+} content decreased in shells.

4.5. In-Situ Surface Effects during ETEM Experiments

4.5.1. Imaging

The evolution of $LiMn_2O_4$ particle surfaces under the influence of water and electric potential was studied in imaging and spectroscopic ETEM experiments. Being precise, the conditions of electrochemical experiments could not be simulated in these experiments. However, they enable to study in-situ how the material behaviour is affected by the presence of a water atmosphere (and inevitably an electron beam).

The experimental set-up, which is described in Section 3.2.1, allows controlling the partial water pressure around the sample as well as to change the electrical potential versus the electron microscope chamber. Two experiments have been carried out focusing on high resolution imaging and on EELS.

High resolution videos of one particle (size 35 nm), that was oriented in (10-1) zone axis, were taken under different conditions. In high vacuum, the particle shows clear periodic contrasts that extend to sharp, faceted surfaces that have sporadic steps with 3.5 Å size (Fig. 4.21) which is preserved under ongoing illumination. The zone axis was determined from a Fourier transform of the image in Fig. 4.21a.

Introducing water in the microscope chamber leads to contrast changes in the centre and at the surface (Fig. 4.22), while the grid was held at the potential of the TEM chamber. A periodic structure is still visible in the centre, but surface layers with thickness up to 14 Å formed where the periodicity is not continued (Fig. 4.22b). Additional contrasts overlay the lattice structure in the centre. The initial facets of the particle are still present in the same orientation, but particle edges are less sharp and the surface roughness increased. Ongoing illumination with the electron beam did not lead to noticeably progression of these effects. Possible explanations for the observed contrast changes in water atmosphere are surface amorphization, recrystallization of domains in the particle, or carbon contamination formation.

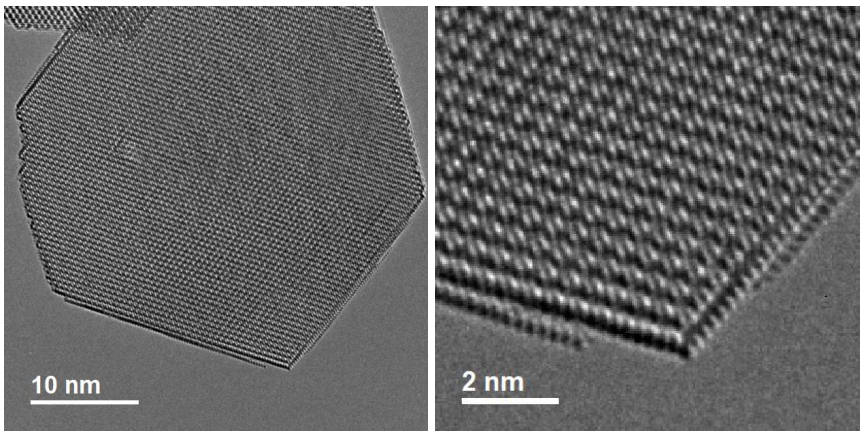

(a) (b)

Figure 4.21.: High resolution TEM image of a $LiMn_2O_4$ particle in pristine state in (10-1) zone axis under high vacuum conditions (a) and detailed view of bottom right corner showing surface structure (b).

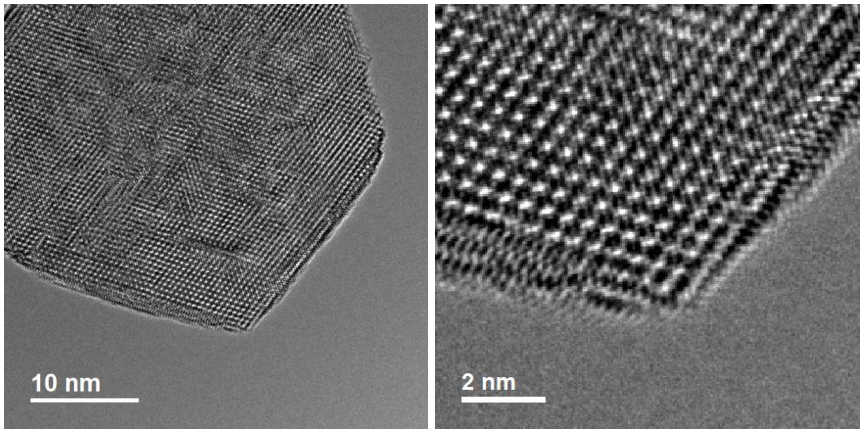

(a) (b)

Figure 4.22.: High resolution TEM image of a $LiMn_2O_4$ particle in pristine state in (10-1) zone axis in water vapor (0.2 mbar (a) and detailed view of bottom right corner showing surface structure (b).

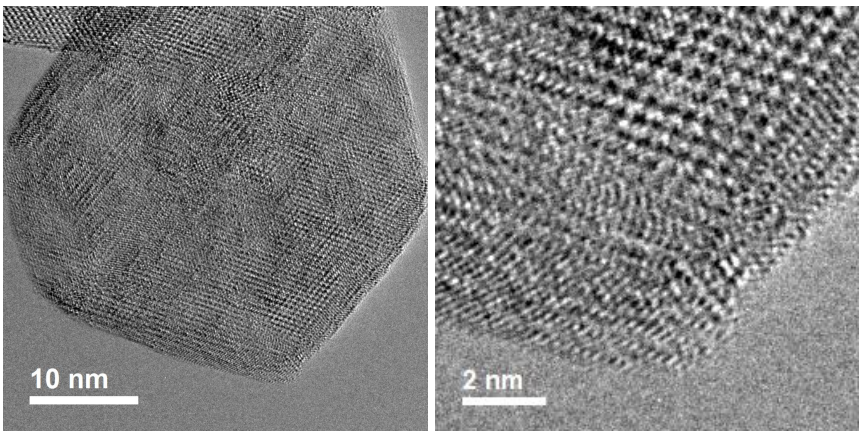

(a) (b)

Figure 4.23.: High resolution TEM image of a $LiMn_2O_4$ particle in pristine state in (10-1) zone axis in water vapor (0.2 mbar with applied potential of 2 V (a) and detailed view of bottom right corner showing surface structure (b).

Applying a potential of 2 V causes a further decrease of periodic contrast in the centre of the particle and an extension of the disordered surface regions to 25 Å. A detailed view of the particle corner is shown in Fig. 4.23b. Changes of the crystal structure have been mapped by measuring the lattice plane distance d in Fourier transformed images. Therefore, the distance of two sets of opposing reflexes was measured in the first and last image of taken image series (see Fig. 4.24a). The lattice constant was determined using the relation Eq. (3.8), a possible mismatch of the microscope's magnification calibration was corrected such that the average lattice constant of measurements in high vacuum state matches the one determined by XRD in pristine state. Fig. 4.24b plots the evolution of the lattice constant measurements versus the experiment time. The presence of water in the microscope chamber is marked by colour, measurements while a potential was applied to the sample are indicated by a dot-pattern.

Although the uncertainty of the lattice constant measurement increases because the noise in the Fourier pattern increases with degrading atomic contrasts, a systematic trend to smaller lattice constants is apparent if water is introduced in the microscope chamber and more pronounced if an external potential is applied. Because of the uncertainty of the diffraction spot position determination, the lattice constants are less exact than XRD.

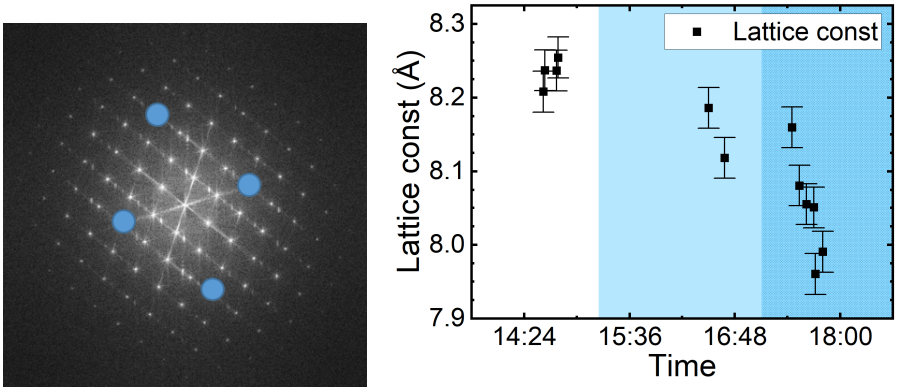

(a) (b)

Figure 4.24.: High resolution TEM image of a $LiMn_2O_4$ particle in pristine state in (10-1) zone axis in water vapour (0.2 mbar with applied potential of 2 V (a) and detailed view of bottom right corner showing surface structure (b).

4.5.2. Spectroscopy

A second ETEM experiment focussed on locally resolved STEM-EELS to investigate the influence of water and potential on the particle's structure. Since the particles are not stable under high electron doses (see Section 4.1), no more than 3 scans should be performed on a single particle. Therefore, suitable particles were selected on the sample, characterized in high vacuum state and then either measured under water or water-potential influence.

EEL spectra in high vacuum, plotted in Fig. 4.25a, from particle surfaces show identical behaviour as previous measurements of pristine particles (see Section 4.2). This indicates, that the shell defect structure with Mn defects in tetrahedral sites is present at the start of this experiment. Bulk spectra differ from previous measurements of pristine particles by a shift of the O K and Mn L edge to higher energies (see Fig. 4.25b) by approx 1 eV and by an increase of the O pre-peak intensity. In addition, an increase of the average bulk valence to $Mn^{4.02(7)+}$ is found, while the values of surfaces increase to $Mn^{3.1(2)+}$. Both values are higher by 0.3 than obtained in previous experiments in high vacuum on the identical sample material (see Section 4.2).

Scanning particles in water atmosphere lead either to particle degradation or to shell oxidation. Particle degradation appears as a strong change of the shape, including loss

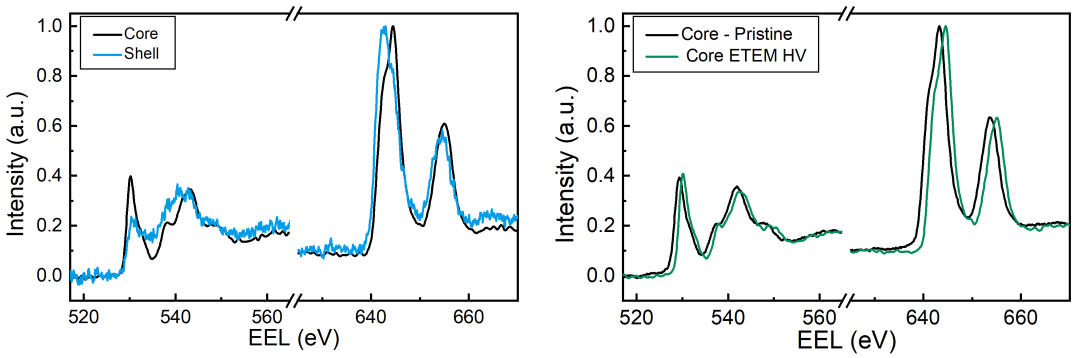

(a) (b)

Figure 4.25.: EEL spectra of pristine $LiMn_2O_4$ particles in high vacuum. Representative spectrum of one particle during pre-characterization in the ETEM experiment, showing a core-shell structure (a). Comparison of core spectra of (a) with an EEL core spectrum from previous STEM measurements (b)

of facets and a reduction in particle volume. An example of a degrading particle is depicted in Fig. 4.26. Initially, a hollow sphere is observed around the particle, that is similar to previously observed effects of contamination (see Fig. 4.3a). This is accompanied by a significant reduction of the Mn oxidation state at the core (see particles 3 and 5 in Fig. 4.27b) and an increase of the particle diameter from 33 nm in high vacuum to 35 nm in H_2O before scanning with the electron beam and finally to 30 nm after scanning in H_2O, including the contrast of contamination.

Particles showing degradation have not been investigated further in ETEM experiments because it is not possible to study the influence of an applied potential systematically on these cases. However, particles that did not show signs of degradation, consistently showed surface oxidation when scanned with the electron beam in water atmosphere, while the core oxidation state remained unchanged. Shell oxidation is indicated by an increase of the O pre-peak intensity and a shift of the Mn L_3 intensity to higher energies (see Fig. 4.27a) as well as in Mn valence values. The average Mn valence changes at the surface of stable particles to $Mn^{4.07(2)+}$ and at the core to $Mn^{4.06(2)+}$. Spectra and valence values show that the surface valence approaches the core state. (Fig. 4.27b). Major differences between core and shell are that the O K-edge at energies of 540 eV has twice the intensity compared to the core and high vacuum state.

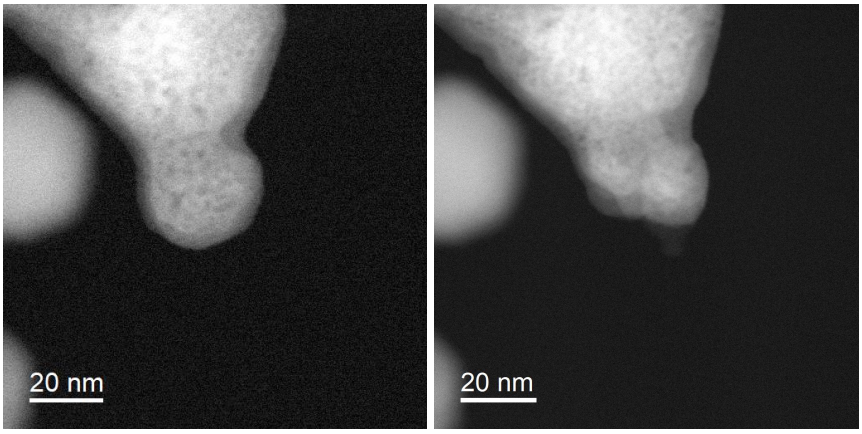

(a) (b)

Figure 4.26.: EEL spectra of $LiMn_2O_4$ particles used in ETEM experiment during pre-characterization in high vacuum. Representative core-shell spectra of one particle (a) and comparison of the core spectra with previous measurements on the same material(b).

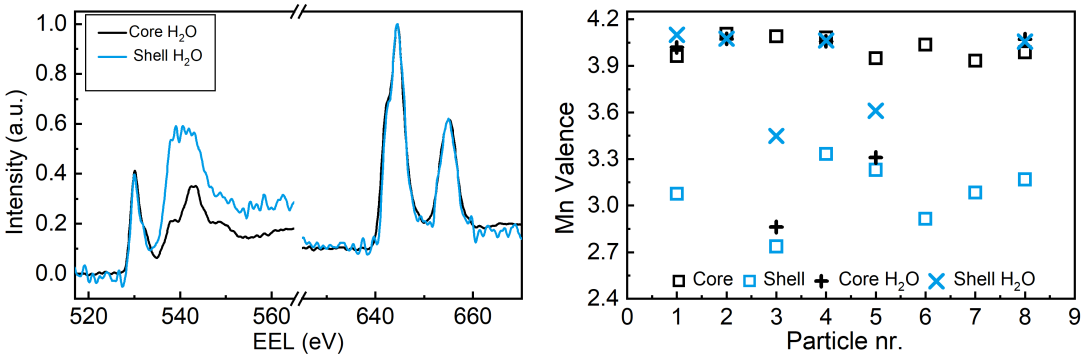

(a) (b)

Figure 4.27.: EEL core and shell spectra of $LiMn_2O_4$ in water atmosphere of 2.7 mbar(a). Evaluated Mn valence measurements of core and shell in high vacuum state (open squares) and after second measurement in water atmosphere (crosses) (b). Particles 6 and 7 have not been characterized in water, particles 3 and 5 showed degradation as depicted in Fig. 4.26.

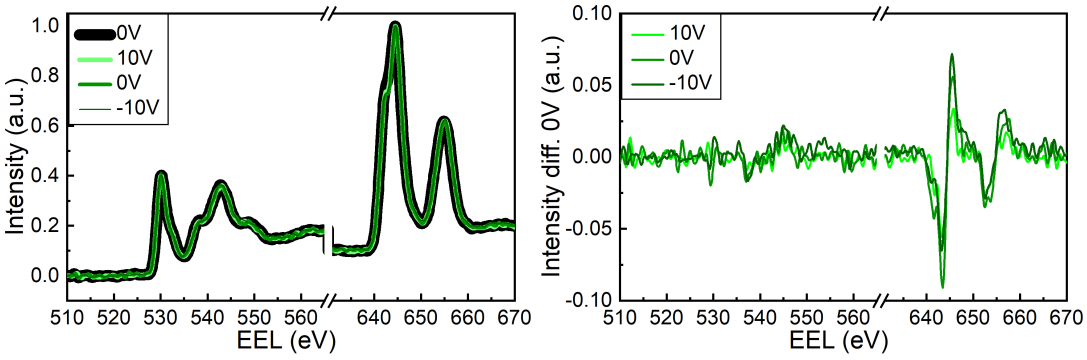

(a) (b)

Figure 4.28.: EEL core spectra of a $LiMn_2O_4$ particle in water atmosphere of 2.7 mbar under application of a potential sequence of [0 V, 10 V, 0 V, −10 V]. Intensity differences of spectra with applied potential and the initial spectrum in water.

The reaction of the particles to an electric potential, that was applied on the supporting grid, was studied on one particle that showed good stability after a scan in water. Potentials were applied in a sequence of [0 V, 10 V, 0 V, −10 V]. Particle cores do not show changes bigger than differences observed between measurements on different particles, if a potential is applied (Fig. 4.28a). The maximum intensity change is 5% at the O K-edge and 9% at the Mn L_3 edge (Fig. 4.28b). The Mn L peaks shift to slightly higher energies, and the intensity of the low energy shoulder at the Mn L_3 peak decreases. This is reflected by an increase of the O pre-peak and Mn L_3 peak distance, which is translated to an increasing Mn valence: [3.99; 4.08; 4.08; 4.17].

Similar trends are observed at the particle surface in Fig. 4.29, with the exception that the O intensity at 540 eV increases by a factor of two with an applied potential of −10 V. The Mn valence values for the potential sequence are [4.06; 4.12; 4.19; 4.20] which is slightly higher than the bulk values. It has to be pointed out that the apparent decrease of the oxygen pre-peak intensity when a potential is applied has to be considered as an artefact. All spectra are normalized by the intensity maximum, which is the Mn L_3 peak. A higher amount of contamination leads to an increase of the background intensity, which is not corrected for before normalization. A higher background at the Mn edge will thus lead to an artificially decreasing relative O pre-peak height.

Previous studies reported that the electron beam itself induces a potential in the sample due to secondary electron emission.[135,136] Thus, it has to be considered, that the

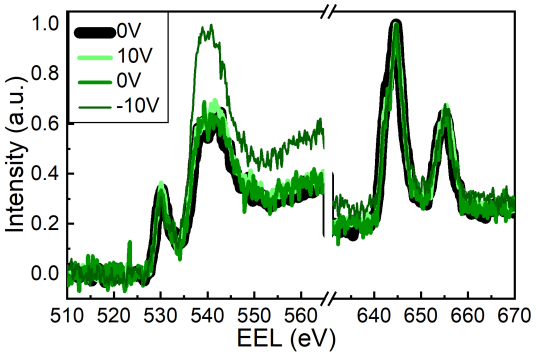

Figure 4.29.: EEL shell spectra of a $LiMn_2O_4$ particle in water atmosphere of 2.7 mbar under application of a potential sequence of [0 V, 10 V, 0 V, −10 V].

effects observed in water atmosphere are partially caused by electron beam effects. As a consequence, particles were studied after the microscope reached high vacuum state again, to be able to differentiate to what extent the electron beam causes the observed reaction in water.

Images and spectra of two particles showing different behaviour are presented in Fig. 4.30. In one case, the typical core-shell structure that is present in pristine particles is still found after potential application in water atmosphere (see Fig. 4.30a, and Fig. 4.30b). The Mn oxidation state changes accordingly to $Mn^{3.22+}$ in the shell and $Mn^{3.94+}$ in the core, which is in the range of values of the pre-characterization in high vacuum state. The shell spectrum however has a higher intensity at O K-edge energies at 535 eV to 550 eV that can be attributed to contamination formation as discussed in Fig. 4.3a.

A different behaviour is observed in Fig. 4.30c, and Fig. 4.30d. The intensity is not homogeneous across the particle and compared to the initial characterization in high vacuum, the diameter increased from 33.8 nm to 36.7 nm. Combined with the high shell O K edge intensity and the absent O pre-peak (as inFig. 4.15) a high amount of contamination formation is expected. The core Mn valence changed from $Mn^{3.93+}$ to $Mn^{3.27+}$ after the experiment, while the shell valence could not be measured because of the missing O pre-peak.

ETEM experiments in water atmosphere show that $LiMn_2O_4$ particles behave differently under the influence of an electron beam in water atmosphere than in vacuum. Effects that have been observed are a change of surface contrast of a single crystalline

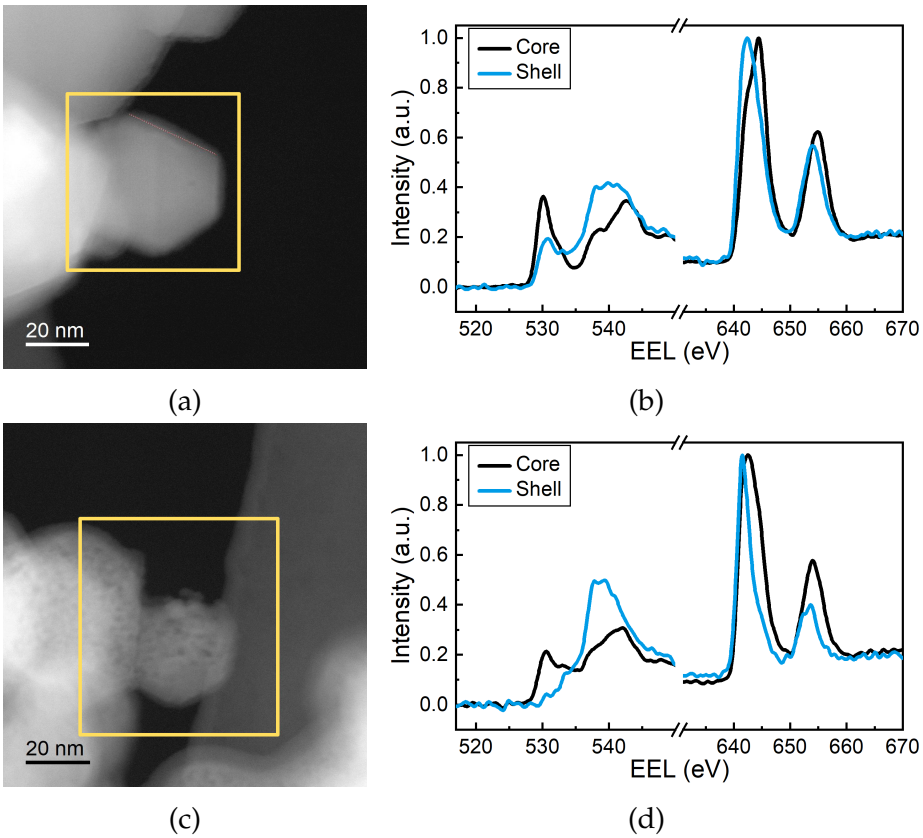

Figure 4.30.: STEM images and EEL spectra of particles at the end of theETEM experiment after the instrument was set in high vacuum state again. Both particles had not been illuminated with the electron beam in the water atmosphere. The particles of the spectra in (b) and (d) are marked in (a) and (c).

particle either due to contamination formation, amorphization or domain formation, while shell oxidation was observed in STEM-EELS experiments. In addition to particle shell oxidation, particle degradation has been observed when particles were scanned with the electron beam in water atmosphere. Particles that were stable under the electron beam did not show a clear reaction to an applied potential. While shell oxidation did not occur without the influence of the electron beam, particle degradation has been observed, although the material has not been scanned with the electron beam in water atmosphere.

5. Discussion: Particle Structure

5.1. Shell Structure of Pristine and Delithiated Particles

Pristine and delithiated particles have a core-shell structure. EELS and XPS measurements show that Mn is in a reduced oxidation state in a 2 nm to 4 nm thick shell layer. It was found that the Mn/O ratio in the shell is higher than expected for bulk $LiMn_2O_4$, that Mn is present as Mn^{2+}, and that the fine structure of the O K edge in shell EEL spectra differs notably from core spectra. In the following paragraphs, the structure of the shell will be explained as an epitaxial layer that contains tetrahedrally coordinated Mn^{2+}.

Mn reduction at $LiMn_2O_4$ surfaces has been observed in several publications and attributed to O vacancy formation[88] or the occupation of tetrahedral sites by Mn^{2+}.[81–83,85,125,137] It was proposed that Mn_3O_4 formation explains formation of Mn rich surfaces. Mn_3O_4 shares the close-packed oxygen lattice with cubic spinel $LiMn_2O_4$ (see Fig. 2.7). In contrast to $LiMn_2O_4$, Mn resides in both octahedral and tetrahedral sites in Mn_3O_4. Tetrahedrally coordinated Mn has the oxidation state Mn^{2+}, while octahedral sites are populated by Mn^{3+}, which is Jahn-Teller active.[138] As a consequence, the unit cell has tetragonal symmetry with lattice mismatches of 1% (a, b) and 14.6% (c), concerning the cubic spinel (a=b=c).[26] If Mn_3O_4 forms on $LiMn_2O_4$ surfaces, it should be discernible by its tetragonal crystal structure. However, except after several cycles of electrochemical de-/lithiation, a direct observation of the Mn_3O_4 crystal structure in the $LiMn_2O_4$ phase has not been made.[83] XRD measurements presented in this work (see Fig. 4.5) did not show any indication of tetragonal Mn_3O_4 peaks albeit having high quality. In combination with high resolution TEM measurements and shell EEL spectra discussed in the next paragraphs, tetragonal Mn_3O_4 formation at surfaces in not a conclusive explanation.

Instead, high resolution TEM images show that an epitaxial relation exists between

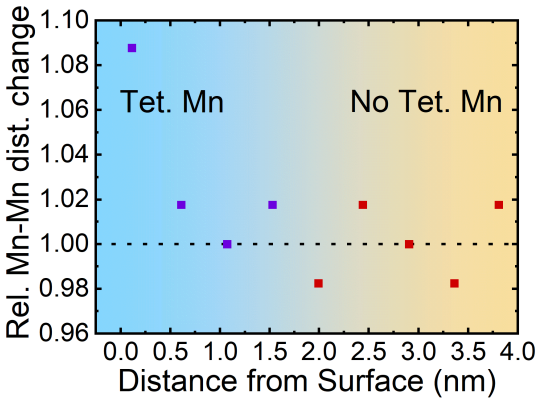

Figure 5.1.: Relative changes of the Mn-Mn distance in a tetrahedral Mn containing surface layer and in a tetrahedral Mn free region deeper in the sample. The region where tetrahedral Mn contrast was present in HAADF images is marked blue. Plotted data is extracted from Fig. 3e in ref. [82].

core and shell, indicating that the shell has the cubic spinel crystal structure. That an epitaxial relation exists between core and surface agrees with a previous analysis on identical samples[23] and with other TEM studies of $LiMn_2O_4$.[81,85,88,137] An analysis of the lattice fringes in Fig. 4.5b reveal that the mismatch of in- and out of plane lattice constants comparing core and shell does not differ by more than 2%, which is much smaller than expected mismatches of Mn_3O_4. In addition, Fig. 5.1 shows a plot of Mn-Mn distances in out of plane direction that were extracted from STEM images of $LiMn_2O_4$ surfaces reported by Gao *et al.*[82]. In proximity of the surface, Mn populates tetrahedral sites, indicated in blue. Except for the topmost layer, no significant difference of Mn-Mn distances was found compared to the tetrahedral Mn free region, thereby ruling a tetragonal distortion out. That Mn_3O_4 formation is unlikely a sufficient explanation for Mn rich shells in this case is also highlighted by the fact that the measured shell Mn oxidation state of $Mn^{2.9+}$ does not fit to $Mn^{2.66+}$, which is the average Mn valence in Mn_3O_4. Thus, an alternative model has to be found to explain the structure of particle shells within the cubic spinel structure.

XPS measurements ruled out that significant contamination with other elements than Li, Mn and O is an explanation for Mn reduction. That means, that the observed shell oxidation state of $Mn^{2.9(2)+}$ can only be explained by stoichiometry variations of Li, Mn and O. To identify what explains the shell structure best, EEL O K-edge spectra of possible defect structures have been simulated by Marco Eckhoff[139] using DFT com-

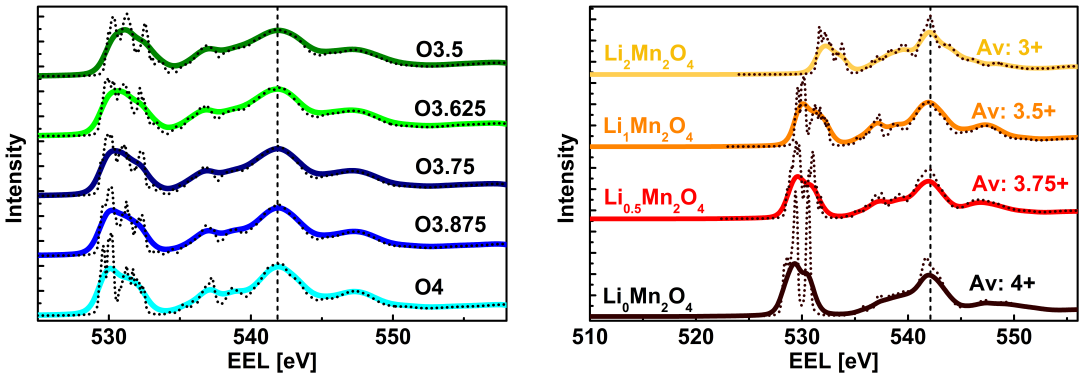

(a) (b)

Figure 5.2.: Simulated EEL O K edge spectra to investigate the influence of O vacancies in $LiMn_2O_{4-\delta}$ (a) and the Li occupation on tetrahedral sites (b) on spectra. The underlying stoichiometry for simulations is included next to the spectra, in case of O vacancies $4-\delta$ is depicted in the graph. Shown data was provided by Marco Eckhoff.

bined with scattering cross-sections, comparable to the approach of Sotoudeh *et al.*[107] These are: O vacancies, Li content in tetrahedral sites and Mn defects on tetrahedral sites. Simulated spectra are compared to measured shell spectra by fingerprinting, enabling to rule out oxygen vacancies and lithium content as the main reason.

Oxygen vacancies are a phenomenon which is broadly discussed in transition metal oxide surfaces.[88,140] The effect of oxygen vacancies on EEL spectra of $LiMn_2O_{4-\delta}$ was simulated by partially removing O from the unit cell down to the formula $LiMn_2O_{3.5}$, which corresponds to Mn^{3+}, while the lattice constant was held at the measured 8.234 Å. Introducing oxygen vacancies does affect the O pre-peak intensity slightly but does not lead to the pre-peak shape changes observed in shell spectra, e.g. an intensity increase at 534 eV (see Fig. 5.2a and Fig. 5.3). As a consequence, O vacancies alone can not explain the shell spectrum shape.

The Li content can be systematically varied by electrochemical de-/lithiation in $LiMn_2O_4$, which directly leads to a change of the Mn oxidation state.[33] Thus, a variation of the Li content in the shell has been considered as a possible explanation for the observed shell spectrum profile. Li contents greater than $x = 1$ in $Li_xMn_2O_4$ lead to a strong tetragonal distortion of the spinel unit cell,[33] which has been accounted for in simulations. Increasing the Li occupancy on tetrahedral sites leads to a shift of the oxygen

pre-peak to higher energies and a reduction of its intensity (see Fig. 5.2b) since less unoccupied Mn 3*d* states are available. Nonetheless, the observed high intensity shoulder 3 eV above the O pre-peak onset in measured shell spectra cannot be reproduced by an increased Li occupation, so that this cannot explain the shell structure.

Mn usually resides in octahedral sites of the cubic spinel structure with oxidation states of Mn^{3+} and Mn^{4+}, but has been reported to occur as Mn^{2+} in tetrahedral sites of surfaces as well.[81–83,85,125,141–143] Therefore, starting with λ-Mn_2O_4 with totally unoccupied tetrahedral sites, tetrahedral sites have been partially filled with Mn and Li. Increasing the tetrahedral Mn content leads to systematic changes in the simulated EEL spectra that are displayed in Fig. 5.3, which are comparable to changes in shell spectra: the O pre-peak onset shifts to higher energies, the O pre-peak height decreases relative to the O 4*sp* peak and the intensity of the high energy shoulder at 534 eV on the convoluted O pre-peak increases relative to the pre-peak intensity.

The observed intensity increase at 534 eV by tetrahedral Mn defects can be explained by comparing calculated DOS plots of $LiMn_2O_4$ (Fig. 5.4a) with $[Mn_{0.5}]_T Mn_2O_4$ (Fig. 5.4b), where octahedral Mn has an identical nominal oxidation state in both structures. Pale colours indicate occupied states, while brighter colours indicate the unoccupied states relevant for EEL spectra calculations. E_g and t_{2g} states of tetrahedral Mn are marked in orange and turquoise, and in yellow and green states for octahedral Mn states. Additional unoccupied e_g and t_{2g} states of tetrahedral Mn are located at higher energy than the ones of octahedrally coordinated Mn. Thus, intensity in shell EEL spectra at 534 can be attributed to the presence of tetrahedral Mn^{2+}.

A comparison of simulated EEL spectra with the observed shell spectrum in Fig. 5.3 allows identifying, which tetrahedral site occupation can reproduce the measured shell spectrum the best. The pre-peak onset energy, its relative intensity to the main O K peak, and the pre-peak shape are used as criteria. A Mn occupation of 0.5 results in the measured pre-peak shape, meaning that intensity at 534 eV is smaller than at 530 eV, but the pre-peak height compared to the O 4*sp* peak is too high. Tetrahedral Mn occupation larger than 0.5 lowers the pre-peak intensity, but the spectrum shape agrees less with the experimental surface spectrum. Thus, the observed shell spectra are best explained with a mixed occupation of Mn and Li on tetrahedral sites. Based on the displayed spectra in Fig. 5.3, the best agreement is found with the composi-

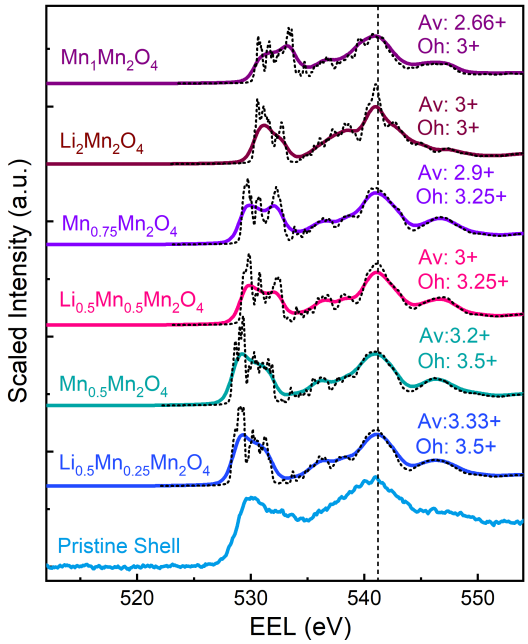

Figure 5.3.: Effect of tetrahedral Mn on the simulated EEL O K edge before (dotted lines) and after (solid lines) convoluting with the experimental energy uncertainty. The energy axis of the simulated spectra are shifted to align with the experimental O 4sp peak (dashed vertical line) shown at the bottom of the plot. The nominal average (Av) and octahedral (Oh) Mn valences are indicated for each spectrum. Shown data was provided by Marco Eckhoff.

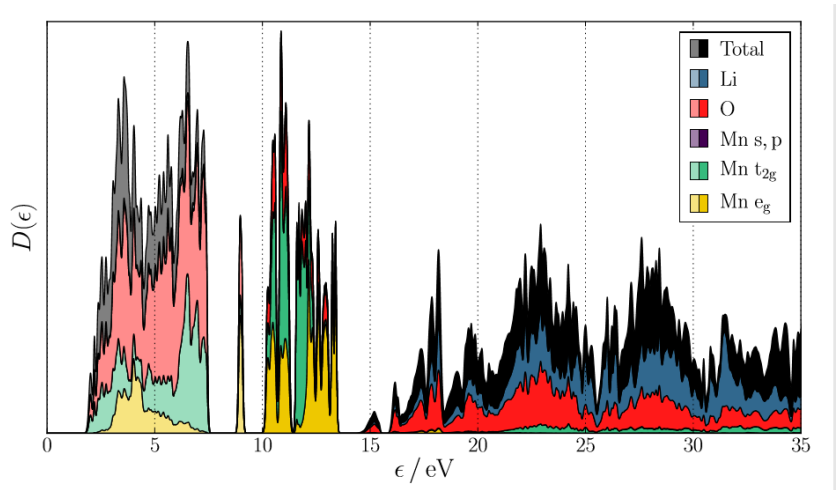

(a)

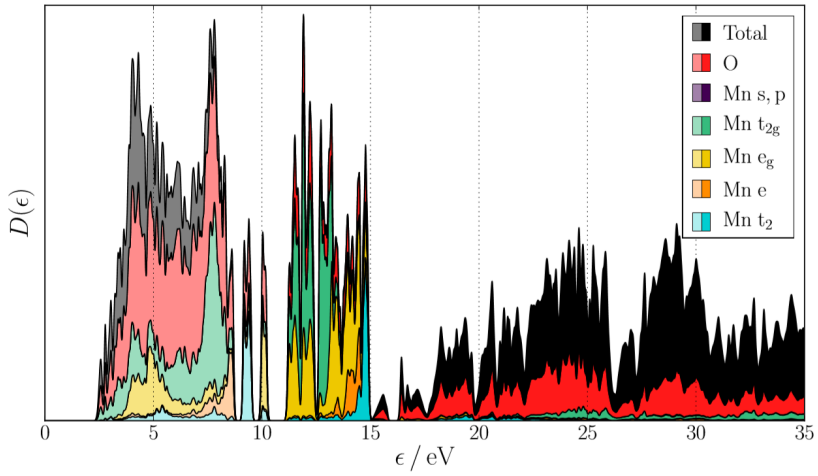

(b)

Figure 5.4.: Calculated DOS for Li1Mn2O4 (a) and $[Mn_{0.5}]_T Mn_2O_4$ (b) showing the influence of replacing Li by Mn on tetrahedral sites. Pale colours indicate occupied states. Mn 3d states of tetrahedrally coordinated Mn are plotted in separate colours to be distinguishable from octahedral 3d states. The displayed data was provided by Marco Eckhoff.

tion $[Li_{0.5}Mn_{0.5}]_TMn_2O_4$. This structure has an octahedral Mn valence of $Mn^{3.25+}$ and an average valence of Mn^{3+}, which is well within the standard deviation of the measured value of $Mn^{2.9(2)+}$ by EELS. An optimum agreement with the measured average shell Mn oxidation state is found for the mixed occupation of tetrahedral sites of $[Li_{0.38}Mn_{0.62}]_TMn_2O_4$. This is close to the best fitting simulated EEL spectrum. It has to be noted that it is not possible to determine an exact shell composition due to the comparably large scatter of the shell valence measurements. Because the particles are aligned differently with respect to the electron beam, the variations in measured shell compositions might also be caused by a varying contribution of core signal to the shell spectra due to different particle orientations. That would mean, under the assumption that all shells have an identical structure, that the minimum measured shell valence reflects the shell structure best.

An increase of the Mn/O ratio in the surface has been confirmed by XPS, where a stoichiometry of $Mn_{2.3}O_4$ was evaluated in pristine particle shells. This is lower than the proposed $Mn_{2.62}O_4$ by fingerprinting EEL spectra, but can be explained by the fact that the probing depth of XPS is higher than the shell layer thickness. At the same time, XPS spectra of Mn edges showed clear evidence that a low Mn oxidation state is present, which could be attributed to Mn^{2+}. Thus, tetrahedral Mn defects are a suitable explanation for the shell structure in good agreement with the experimental data.

The impact of delithiation on the shell structure could not be refined with high accuracy. Contamination as residual from the delithiation experiments which also includes Mn makes it hard to estimate if and how particle shells change under delithiation. Still, the core-shell structure in terms of the Mn oxidation state is present after delithiation and particle shells are significantly reduced. Similar points, which lead to the exclusion of O vacancies and increased Li content in particle shells, make those possibilities unlikely as explanation for Mn reduction in shells after delithiation. Thus, it is expected that tetrahedral Mn is still present in particle shells, which aligns well with a number of literature reports. These state that delithiation leads to an increased population of tetrahedral sites by Mn.[81–83]

Different possible explanations for the observed Mn reduction in particle shells have been tested with the help of DFT based EELS simulations performed by Marco Eckhoff.[139] It was identified that only Mn defects on tetrahedral sites are able to explain

both, effects of shell EEL spectra and the reduced Mn oxidation state. A composition of $[Li_{0.38}Mn_{0.62}]_T Mn_2O_4$ is the best fitting tetrahedral site occupation that explains the observed shell spectrum shape and the experimentally measured Mn oxidation state.

5.2. OER Impact on Shell Structure

Mn oxidation of particle shells and an increase of the average oxidation state after using the particles for catalysing the OER has been observed by XAS, XPS, and EELS. The spatial resolution of STEM-EELS allows locating the oxidation state increase in the particle shells that contain tetrahedral Mn^{2+} in pristine state. Both, XPS and EELS measurements show that the concentration of tetrahedrally coordinated Mn^{2+} is decreased after catalysing the OER. This will be explained by dissolution of tetrahedral Mn defects out of particle shells, which occurs as a parasitic reaction during OER experiments, in the following paragraphs.

Fig. 5.5 shows electrical currents observed in catalytic experiments of pristine particles. The experimental details of this experiment are summarized in Section 3.1.3, the experiments were performed by Max Baumung.[34,90] Disk currents, presented in Fig. 5.5a, include all electrical currents that pass through the electrode that contains the catalyst.

The disk currents, which are normalized by the geometric electrode area, are increased in the potential window of 1.3 V to 1.6 V in the first three positive going half cycles of the ten scans. In later cycles a steady state behaviour is approached where the exponential current-potential relationship at $E \geq 1.58\,\mathrm{V}$ coincides with the current onset of oxygen evolution.[23,90] This behaviour is consistent with previous catalytic experiments on this material where manganese dissolution was identified as cause for the increased disk currents predominantly in the first 3 cycles.[23,90,91]

Currents caused by Mn dissolution have been estimated by subtracting the $j - E$-curve of the tenth cycle, where a steady state behaviour and OER dominated currents are assumed, from the first three cycles. Mn loss currents during the first three cycles are plotted in Fig. 5.5b. A total charge of 16.3 mC is ascribed to Mn dissolution by integrating the summed currents of the first three cycles. 3.5 mC (21% of the total charge) have passed the electrode before the oxygen evolution started in the first cycle at 1.58 V,

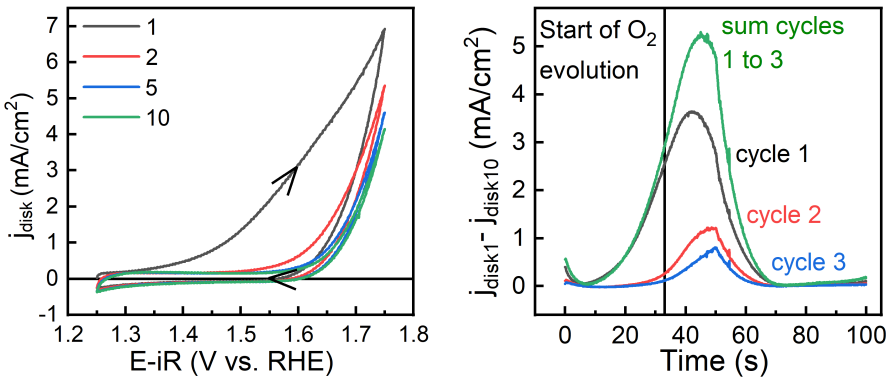

(a) (b)

Figure 5.5.: Pristine $LiMn_2O_4$ RRDE electrocatalysis of OER. (a) Disk current normalized to the geometric disk area (j_{disk}) for cycles 1, 2, 5 and, 10 of OER in NaOH (pH13) with an electrode ink containing the pristine powder. (b) Estimated Mn current density obtained by subtracting the tenth cycle from the previous ones ($j_{disk,i} - j_{disk,10}$). The vertical line indicates the start of OER at a disk potential of 1.58 V. Experiments were conducted by Max Baumung.

which is indicated by a vertical line in Fig. 5.5b.

When Mn is dissolved out of the particles, formation of MnO_4^- is predicted by an E-pH diagram of Mn-H_2O[144] in the alkaline electrolyte. This necessitates transfer of $(7-x)$ electrons from the dissolved Mn^{x+} species via the reaction

$$Mn^{x+} + 8OH^- \rightarrow Mn^{7+}O_4^- + 4H_2O + (7-x)e^-, \tag{5.1}$$

where x describes the initial Mn oxidation state prior to dissolution. To confirm Mn^{2+} dissolution from the shell as cause for shell oxidation, the total amount of Mn dissolution has to be estimated.

The shell volume share was previously estimated with 20%. The overall composition, including core and shell, was assumed to be stoichiometric $LiMn_2O_4$, which agrees with the measured average Mn oxidation state of $Mn^{3.52}$ by XAS (see Table 4.1). Thus, the average molar weight of the nanoparticles is 179.82 g mol^{-1}. A portion of 5.59×10^{-8} mol belongs to the surface layer when the total catalyst loading is 2.8×10^{-7} mol. Based on the shell composition of $[Li_{0.38}Mn_{0.62}]_TMn_2O_4$ the amount of tetrahedral Mn^{2+} in the catalyst is 2.8×10^{-8} mol. According to Faraday's law, a total charge trans-

fer Q is necessary in an electrochemical reaction with a charge transfer of z and amount of material n_{mole},

$$Q = Fz \cdot n_{mole}, \tag{5.2}$$

where F is the Faraday constant. If all tetrahedral Mn^{2+} is leached out of the shell ($z = 5$), a charge transfer of 16.4 mC would be expected, which agrees very well with the measured 16.3 mC Dissolution of other Mn species is less plausible. Loss of Mn^{4+} would not be able to explain the observed reduced amount of tetrahedral Mn and disagree with shell oxidation. The amount of Mn^{3+} dissolution, that would result in the measured shell oxidation state, makes a charge transfer of 9.53 mC necessary. That agrees less with the exhibited currents and the fact that EEL O K spectra and XPS Mn $2p$ spectra indicate coherently a reduced amount of Mn^{2+}.

This current analysis supports the picture that the majority of tetrahedral Mn defects gets dissolved out of the shell during electrochemical cycling in the potential window of 1.4 eV to 1.7 eV, which causes an increase of the average and octahedral Mn oxidation state. Dissolution of all tetrahedral Mn would lead to a shell composition of $[Li_{0.38}Mn_0]_T Mn_2O_4$ and to an average valence of $Mn^{3.81+}$, which deviates more than the standard deviation of the measured Mn oxidation state of $Mn^{3.5(2)+}$ by EELS of cycled particles. Because Li prefers to maximise the distance between individual ions in the structure,[32,33,60] it might be preferred that Li diffuses from the core to the shell, if tetrahedral sites are made available by Mn dissolution. Reported Li diffusion coefficients range from $1 \times 10^{-11}\,cm^2/s$ to $1 \times 10^{-12}\,cm^2/s$ in $LiMn_2O_4$.[145,146] Thus, diffusion lengths of approximately 2 µm are possible within two hours, which is approximately the time between electrochemical cycling and the TEM experiments. The distance from core to shell of 30 nm can be covered by Li ions within 0.2 s, whereas one cycle in OER experiments takes 50 s. A study by Erichsen *et al.*[104] tracked lithiation kinetics in $LiMn_2O_4$ and showed that a lithiation front in $LiMn_2O_4$, which involves a tetragonal phase transformation, moves on micrometer scale in the time of one OER scan. This means that complete Li redistribution is possible across one nanoparticle in that time. Based on the assumption of a Li content on tetrahedral sites of $x = 0.38$ in the shell and of $x = 1$ in the core prior to catalysis, a homogeneous Li content on all available tetrahedral sites of $x = 0.88$ is expected after Mn^{2+} leached out the shell. This leads to an estimated shell composition of $Li_{0.88}Mn_2O_4$ with an average Mn valence of

$Mn^{3.56+}$ after OER catalysis, which fits the measured $Mn^{3.5+}$ well. An increase of the core oxidation state of 0.06 is expected if Li diffuses out of the core. This agrees well with the measured slight increase of the Mn core oxidation state from Mn $^{3.72+}$ prior to catalysis to $Mn^{3.78+}$ after OER catalysis.

When tetrahedral Mn is present, it contributes to an average valence value that is measured by EELS. Under the assumption that tetrahedral sites are either occupied by Li or Mn in pristine particles, hence $[Li_{1-t}Mn_t^{2+}]Mn^{y+}O_4$, the effect of tetrahedral Mn on the octahedral valence y can be calculated via the measured average oxidation state V_{Mn} with the charge neutrality condition.

$$t = \frac{5}{V_{Mn} - 1} - 2 \tag{5.3}$$

$$y = 3.5 - \frac{t}{2} \tag{5.4}$$

EELS shell valence values predict a shell composition change from $[Li_{0.38}Mn_{0.62}^{2+}]Mn^{3.19+}O_4$ to $[Li_{0.88}Mn_0^{2+}]Mn^{3.56+}O_4$ after OER, which involves a change of the octahedral Mn oxidation state by 0.37.

As average over the whole particles, an increase of the bulk Mn oxidation state by 0.2 after electrochemical cycling has been observed in XAS measurements as well, while EELS indicates that the particle core remains close to the pristine oxidation state of $Mn^{3.72+}$. As depicted in Fig. 5.6, a core-shell model, with an assumed shell volume share of 20%, results in good agreement between the calculated average Mn valence values from EELS compared to ensemble XAS valence measurements.

In addition to Mn loss from $LiMn_2O_4$ in electrocatalytic experiments,[23,90,91] Mn leaching is predominantly discussed, when this material is used as cathode in battery cells, as acid induced disproportionation of Mn^{3+}. It is assumed that Mn^{2+} is dissolved in the electrolyte via the reaction:

$$2Mn_{solid}^{3+} \rightarrow Mn_{solution}^{2+} + Mn_{solid}^{4+} \tag{5.5}$$

where octahedrally coordinated Mn^{3+} leaches out of $LiMn_2O_4$ surfaces.[59,133,147–150] This reaction is often discussed as being initiated by F-Mn^{3+} bond formation, which weakens Mn adhesion to the crystal.[133,148,151–153] It has to be mentioned that the con-

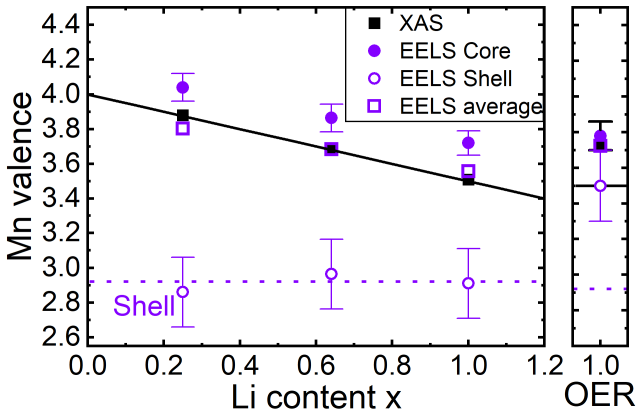

Figure 5.6.: Comparison of EELS and XAS based Mn valence calculations versus the measured Li content of the composition $Li_xMn_2O_4$. The average valence of EELS was calculated using a core-shell model with a shell volume share of 19%. XAS valence values of delithiated samples are taken from Baumung[34]. Valence measurements of pristine particles after catalysing the OER with nominal $x = 1$ are depicted in the right panel. XAS experiments were conducted by Max Baumung.

ditions under which Mn loss was observed in OER experiments cannot be compared to the ones in battery cells. Instead of using an organic, non-aqueous and acidic electrolyte as in battery cells, the OER experiments are carried out in alkaline, aqueous conditions. Mn dissolution was attributed to Mn^{2+}, which is already built in the crystal structure, instead of Mn^{3+} disproportionation. Since the free energy of Mn^{2+} dissolution in neutral water is approximately half of that of Mn^{3+}, it is expected that tetrahedrally coordinated Mn^{2+} is preferentially dissolved out of $LiMn_2O_4$ surfaces.[151] This is in full agreement with the presented picture about the origin of Mn dissolution OER.

Formation of tetrahedral Mn in $LiMn_2O_4$ surface regions has been reported in battery experiments as well if $LiMn_2O_4$ is delithiated. This was described as a reversible process, where the concentration of tetrahedral Mn decreased after subsequent lithiation.[81–83] The mechanism of reversible formation of tetrahedral Mn containing surface layers under de-/lithiation is not understood in detail yet. It is assumed that such surface defects form because $LiMn_2O_4$ surfaces are not stable thermodynamically,[27,81,154] or that population of tetrahedral sites by Mn is induced by strain.[82] Two possibilities have been discussed for the reversible formation of defect surface layers, which are either complete decomposition in the battery electrolyte, or dissolution of Mn on tetra-

hedral sites only.[81] The calculated parasitic currents during OER catalysis agree well with the latter, if Mn rich surfaces are degrading. However, a reaction of tetrahedral Mn only can not explain how a Mn rich surface layer can initially form, if no Mn source is available. It can be stated, that dissolution of tetrahedral Mn requires a charge transfer and happens only at potentials greater than 1.3 V in RRDE experiment. The test experiments show that Mn defects in the shell are a stable in the alkaline electrolyte.

As a result, dissolution of tetrahedral Mn defects, predominantly in the first three cycles of OER catalysis, explains the observed oxidation of Mn in the shell well. Dissolution of tetrahedral Mn leads to an increase of the average Mn oxidation state in the shell by 0.6 and of the octahedrally coordinated Mn by 0.37.

5.3. Core Effects and Induced Shell Strain

XRD measurements showed that pristine particles have the expected cubic spinel structure. However, the measured core oxidation state of $Mn^{3.72+}$ in pristine particles deviates from the expected $Mn^{3.5+}$. In the following paragraphs, it will be discussed how the increased core oxidation state can be explained and what amount of strain is expected from an epitaxial core-shell relationship.

Lattice constants that were reported for stoichiometric $LiMn_2O_4$ are larger than the measured $a_1 = 8.234(2)$ Å. An average of 8 published lattice constants gives $a = 8.241(8)$ Å with a range of [8.225 Å:8.251 Å].[52,54,55,57,58,75,155,156] 75% of the reported values are larger than 8.24 Å. Differences larger than 0.07 Å are bigger than the experimental uncertainties. It could be demonstrated that Mn valence altering bulk defects, such as O over- or under- stoichiometry or replacement of Mn by Li on octahedral sites, affect the lattice constant of $LiMn_2O_4$. As an approximation, a linear relationship exists between the lattice parameter and the Mn^{3+} content[157] or the Mn valence. Higher Mn oxidation states lead to smaller lattice parameters, which was summarized for a number of defect structures in Fig. 2.7. The high amount of scatter shows the difficulty to determine the exact defect structures, stoichiometry and the resulting Mn oxidation state.

A core oxidation state of $Mn^{3.7+}$ was measured by EELS, which is higher than the expected $Mn^{3.5+}$ for stoichiometric $LiMn_2O_4$ and means, that a smaller lattice constant

between $a = 8.19$ Å and $a = 8.22$ Å is expected on the basis of the just mentioned trend. This is smaller than the measured $a = 8.234(3)$ Å. As described in Section 2.3.2, both Li replacing Mn on tetrahedral sites and cation vacancies can account for an increased Mn oxidation state in spinel bulk structures.[74,75] Based on the Mn oxidation state, a value of $x = 0.15$ would be expected in the case of Li rich $Li_{1+x}Mn_{2-x}O_4$ spinels. A Li rich core would not only explain the observed oxidation state, but also that no orthorhombic transition was identified in temperature dependent XRD measurements.[32]. A shift of the transition temperature of the cubic to orthorhombic transition to lower values was observed with increasing Mn^{4+} concentration.[68]

At the same time, a smaller average Mn oxidation state of $Mn^{2.9+}$ was found in particle shells. Based on the trend in Fig. 2.7, an equilibrium lattice constant of $a_{shell} = 8.3$ Å is extrapolated for this oxidation state in the cubic spinel system. A shell stoichiometry of $[Li_{0.38}Mn_{0.62}]_T Mn_2O_4$ was estimated by fingerprinting EEL spectra and the measured average shell oxidation state of Mn. Since an epitaxial relationship exists between core and shell, the difference between the expected core and shell equilibrium lattice constants leads to compressive in-plane strain in the shell and tensile strain in the core. The amount of strain was estimated using a strain model for spherical core-shell nanoparticles.[158] A particle with a diameter $d = 65$ nm, a shell thickness of $d_{shell} = 4$ nm and a Poisson's ratio of 0.3[159] was used in the calculations. This results in an expected strain of 0.12% for the core and an in-plane stress in the shell of -1% and an out of plane stress of 0.93%. Combined, the expected lattice constant of the core is $a_{core} = 8.215$ Å and an in-plane lattice constant of $a_{shell-ip} = 8.215$ Å. The resulting lattice parameters are still smaller than the experimentally determined value, but still in the range of the scatter $\delta a = 0.03$ Å of reported lattice constants for one oxidation state in Fig. 2.7. The negligible in-plane lattice constant mismatch fits well to the amount of inhomogeneous strain that was evaluated from XRD data (see Fig. 4.4b). The out of plane lattice constant mismatch of 2% compared to the core is larger than the strain estimated by XRD, while the estimated core strain fits well to the amount of measured inhomogeneous strain. That the estimated variation of lattice constants by the FWHM of XRD peaks did not indicate this strain component is likely explained by the small scattering volume of the shell. According to Scherrer broadening a $FWHM = 2.6°$ is expected by the out of plane shell size of 4 nm, which is much larger than the $FWHM$ of the main peaks of about 0.15°. As a result of the small scattering volume of the shell, it is not possible to resolve the shell strain components by XRD, which has been confirmed in

personal communication with Dr. Helmut Klein and Dr. Heidrun Sowa. The estimated strain values are smaller than the resolution limit of strain measurements by HRTEM of 2%.[160]

The shell Mn oxidation state and defect structure of particle shells did not exhibit significant changes after delithiation, while the core oxidation state increased due to delithiation. This means that the difference between core and shell oxidation state increases, which should lead to an increase of strain in the shell. A lattice constant of $a_{x=0.25} = 8.0907\,\text{Å}$ was reported for the $x = 0.25$ sample. If that value is taken as the core lattice constant, a core strain of 0.28%, a shell in-plane strain of -2.3% and a shell out of plane strain of 2.1% is estimated using the particle strain model.

A shell volume share of 20% was estimated by comparison of valence measurements by XAS which represent an average over a bulk set of particles with calculated average values on the basis of EELS measurements. The composition of core and shell of the particles needs to deviate from $LiMn_2O_4$ to explain the measured oxidation states. A core composition of $Li_{1.15}Mn_{1.85}O_4$ and a shell composition of $[Li_{0.38}Mn_{0.62}]_TMn_2O_4$ were estimated as a possible explanation for core and shell structure. In the core-shell model, this leads to an average composition of $Li_{0.996}Mn_{2.004}O_4$, which is very close to the nominal composition of $LiMn_2O_4$ given by the manufacturer.

5.4. ETEM Experiments

In-situ ETEM studies show identical behaviour after a water atmosphere has been introduced in the microscope chamber (see. Fig. 4.27) along with a significant increase of the Mn oxidation state in the shell. An increase of the Mn oxidation state is the opposite of electron beam induced effects in high-vacuum, where repeated scanning leads to a reduction instead of an oxidation of Mn (see Fig. 4.3). Therefore, this behaviour does not need to be discussed as an artefact of the measurement, but as an effect of the water atmosphere.

Core spectra of particles in water atmosphere do not change under the presence of water, but have a lower intensity in the range of 535 eV to 545 eV compared to the shell. The particle thickness is lower in the shell by a factor of three, so that a thin layer of water or contamination will have more weight in the normalized spectrum signal.

This signal increased significantly after a potential of −10 V was applied to the sample grid, which indicates that the layer thickness increased due to a potential effect (see Fig. 4.29). The same particle has been illuminated with the electron beam beforehand, using identical beam conditions, which did not lead to an intensity increase. An electron beam influence alone thus can not explain the sudden rise in the fourth scan.

An increased O intensity in this energy region has been observed in high vacuum and was attributed to electron beam induced contamination (see Fig. 4.3a and Fig. 4.1b). Since $LiMn_2O_4$ EEL spectra have a pronounced fine structure at energies of 535 eV to 545 eV, the additional intensity that is observed in shell spectra under water atmosphere was extracted by subtracting the core from the shell spectrum of Fig. 4.27 and compared to Fig. 4.3a, which is plotted in Fig. 5.7 along with a reported EEL spectrum of water at room temperature. The extracted signal agrees very well with the EEL O edge of contamination, which built up after repeated scanning with the electron beam (see Section 4.1). At the same time, the peak position of water agrees well with the signal in Fig. 5.7a, so that the origin of the additional intensity can not be attributed solely to water and/or electron beam induced contamination based on the spectrum shape.

The oxygen atom number density in $LiMn_2O_4$ of 0.1 mol/cm^3 is comparable with the one of water (0.11 mol/cm^3). Under the assumption that the intensity in the energy range of 535 eV to 545 eV of the O K-edge is proportional to the density of oxygen times sample thickness, it can be estimated how thick a water layer has to be to cause the additional signal of Fig. 5.7a. It is assumed that the O/Mn ratio is equal in core and shell after water contact, since presence of additional tetrahedral Mn contradicts the measured Mn valence state of Mn^{4+}. The additional oxygen signal is defined here as area difference of integrating a normalized core and shell spectrum (in Fig. 4.27) from 535 eV to 550 eV. The O intensity is higher by a factor of 1.9 in the shell. If due to water, a water layer with thickness $t_{H_2O} = 0.45 \cdot t_{LiMn_2O_4}$ would be necessary to explain the additional signal. The relative sample thickness t/λ in shell regions is extracted from the low-loss spectra, where λ describes the inelastic mean free path of the electrons, which is 155 nm in $LiMn_2O_4$ and 210 nm in H_2O (simulated using QUASES[113]) and 300 kV acceleration voltage. The average thickness of the shell in Fig. 4.27 was calculated to be 18.6 nm using λ of $LiMn_2O_4$, of which 4.4 nm would correspond to the thickness of a water layer on top and bottom of the particle.

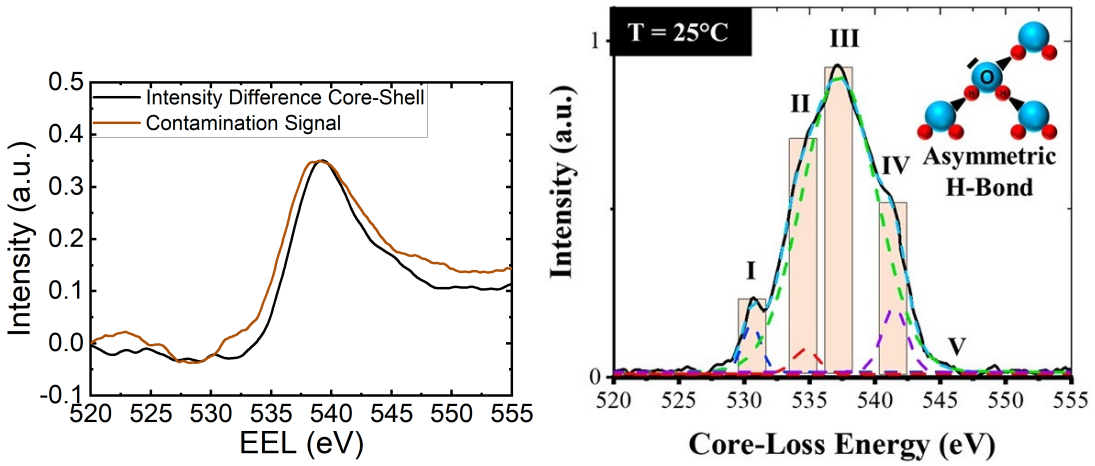

(a) (b)

Figure 5.7.: Difference of normalized core and shell EEL spectra shown in Fig. 4.27 (a) (black) compared to a spectrum of contamination that built up in high vacuum EELS experiments. Both spectra were normalized and smoothed for better comparison. (b) Reported EELS O K edge of water encapsulated in graphene. Reprinted with permission from ref. [161] Copyright 2019 American Chemical Society.

Formation of thin water layers at pressures lower than the equilibrium water pressure has been studied on manganites.[162,163] Thereby, the water coverage depends on the surface energy of the manganite surface,[163] which is dependent on the termination and orientation of the surfaces in $LiMn_2O_4$ but has a maximum of $1.3\,J/m^2$.[27] At the experimental water partial pressure of 2.4 mbar, a coverage of 3.6 monolayers of water is expected as maximum.[163] The thickness of a monolayer of water was determined to be 0.25 nm.[162] This means, that the water layer thickness, that can explain the higher oxygen signal in shell EEL spectra, is approximately four times higher than the upper limit of expected water layer thickness formation. As a consequence, the additional intensity has to be explained to a bigger extent by contamination formation, presumably by amorphous carbon deposition, than by an expected water layer.

Comparing of Fig. 4.26a and Fig. 4.27a shows that the water atmosphere in the microscope enhances contamination formation at particle surfaces, which is accelerated if a potential is applied (see Fig. 4.29). The observed contrast changes in high resolution experiments after water has been introduced in the microscope chamber, which got more pronounced after a potential was applied to the sample, have to be considered

being caused by formation of dirt, rather than by amorphization of the surface.

Oxidation of particle shells has not been observed in high vacuum conditions, which highlights that water has to be part in this reaction. If scanned with the electron beam in water atmosphere, the shell oxidises similar to what has been observed due to OER catalysis. Indeed, exposure to the electron beam is critical to cause this reaction. This is highlighted by the data presented in Fig. 4.30b. Although, the particle experienced water atmosphere and applied potential, no shell oxidation was found when scanned with the electron beam only in high vacuum. Electron beam dependent chemistry has been observed in previous ETEM experiments.[135,136,164] Generation of secondary electrons in the sample can lead to accumulation of positive charge and thus to potential formation in the sample.

The electrochemical conditions in the ETEM deviate to a great extent from RRDE experiments by the absence of an electrolyte and uncontrolled pH of the sample environment. While OH^- dominates in conducted cyclic voltammetry experiments using a NaOH solution with pH= 13, positively charged H_3O^+ is the more frequent species under ETEM conditions. Thus, a direct comparison to the effects of electrochemical experiments cannot be made.

5.5. Summary Particle Structure Effects

$LiMn_2O_4$ nanoparticles that were used in this work exhibit a complex microstructure, which reacts differently to electrochemical treatments. This behaviour is summarized in Fig. 5.8. It was shown that pristine particles are single crystalline but have a core-shell structure in terms of stoichiometry, site population and Mn oxidation state. The shell contains Mn defects that replace Li on approximately 2/3 of the 8*a*-tetrahedral sites and lead to a reduction of the average Mn oxidation state and the one of octahedrally coordinated Mn. This kind of defect structure is a frequently observed behaviour in $LiMn_2O_4$ surface regions.[81–83,85] Mn in the core of the particles is oxidised compared to the expected oxidation state of $Mn^{3.5+}$. That was attributed to a Li rich phase in the core, that is frequently observed in cubic spinel $LiMn_2O_4$.[59,74,78,165–167] The dependency of the lattice constant of the Mn oxidation state causes strain of about 1% in the shell due to the epitaxial relationship between core and shell.
Electrochemical delithiation led to the expected increase of the core Mn oxidation state,

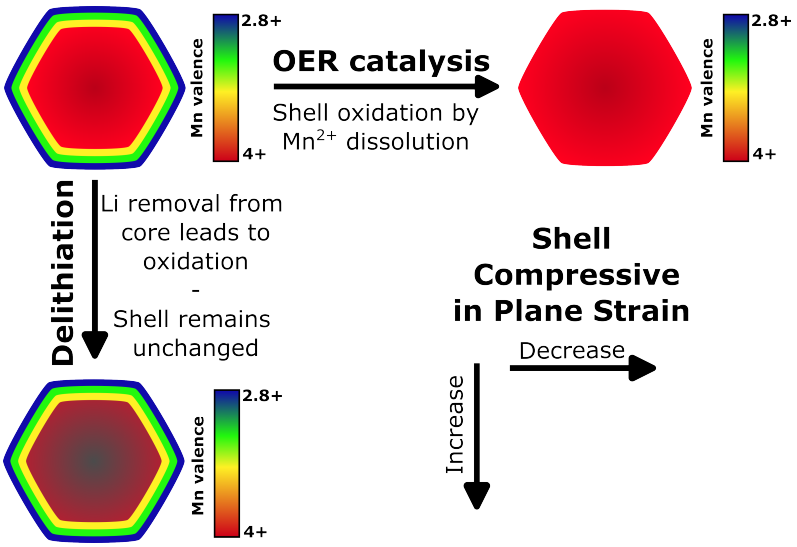

Figure 5.8.: Summary graph of how different electrochemical treatments affect the core and shell Mn oxidation state and strain.

however the defect structure of the shell remained. Since delithiation involves lattice contraction,[32] an increase of strain in the shell up to 2.3% is expected.

An opposite behaviour was found if the particles were used to catalyse the OER. The significant increase of the shell Mn oxidation state could be attributed to dissolution of tetrahedral Mn^{2+} in the first three electrochemical cycles, leading to a smaller difference of core and shell Mn oxidation state. The core oxidation state did only increase slightly after OER catalysis, which was explained by reordering of the Li distribution over tetrahedral sites. As a result of the better agreeing core and shell Mn oxidation states, a smaller amount of shell strain is expected after OER catalysis.

6. Discussion: OER Activity and Bulk Descriptors

An established approach to understand what influences the activity of a material that is used for catalysing the OER and ORR, is to assess the binding energies of reaction intermediates of OER/ORR on the surface of the catalyst.[11,35,36,168] This is condensed in the Sabatier principle, which states that an optimum catalyst surface binds neither too weak nor too strong to important reaction intermediates. Assuming a linear relationship between binding energy and overpotential leads to a volcano shaped activity relationship with the binding energy. Since binding energies are difficult to determine in experiments[15,169] correlations between material and binding energies or catalytic behaviour have been established so far to describe a material's catalytic activity and to predict highly active catalysts. Those descriptors often base on electronic properties like e_g-occupancy,[9,16] number of outer electrons,[36] oxygen $2p$-band centre,[26,38,39] or metal-oxygen covalence.[10,40] But also crystal structure based descriptors, e.g. metal-oxygen bond length or angle, have been taken into consideration.[17]

Often, these correlations are based on the catalysts bulk properties[9,10,12,16] and a clear statement about how these are connected to the properties of the surface is elusive. Since catalysis is a process that is happening at the catalysts surface, it has to be assumed that surface properties play the major role for effectively transferring electrons to or from the adsorbed reaction intermediates. The results presented in this work show that bulk and surface properties can differ vastly in $LiMn_2O_4$. The surface stoichiometry, electronic structure and strain state do not only differ from the bulk or core, they also evolve differently under electrochemical treatment. Delithiation changes the bulk Mn valence and hence the e_g occupancy, but no significant shell oxidation could be detected. On the other hand, the e_g occupancy changes under electrochemical cycling in the shell, whereas it stays constant in particle cores. Thus, using for example bulk Mn e_g occupancy, which is an established descriptor in spinels,[16] will inevitably

mislead the interpretation of catalytic activity of this material because surface properties are independent of the bulk.

Furthermore, it was concluded that the surface Mn e_g occupancy changes significantly in the first three cycles, which shows that the value of a descriptor can change during catalysis. This clearly limits the reliability of a steady state bulk descriptor. Other examples show that the surface termination of $LaNiO_3$ thin films has a large impact on the measured activity,[29] although the underlying bulk structure is identical. The fact that activity of RuO_2 and IrO_2 depends on the surface orientation[30,170] also highlights that a single bulk descriptor is not able to describe the catalytic activity of a surface accurately.

From this perspective, it is surprising that application of bulk material properties has been successful in establishing activity-property correlations in specific material systems. In fact, the bulk and surface structure are to some extent connected, which enables to find correlations between bulk properties and catalytic activity. In this case, the shell crystal structure obeys the core through an epitaxial relationship, meaning that structural parameters like bond lengths are likely to be similar at particle surfaces. In contrast, the e_g occupancy varies and predicts a tetragonal shell structure. Thus, the core imposes compressive in-plane stress to the shell. Since strain alters the electronic structure of transition metal oxides, e.g. the O $2p$ band centre or preferential occupation of e_g orbitals (details in Section 2.2.5), the shell electronic properties are affected by the core influence. Other examples, where bulk measures relate to surface properties, are correlations of the adsorption energies with the bulk formation energies of a material,[12] or between the bulk and surface O $2p$ band centre position relative to the Fermi level.[171] Nonetheless, these correlations have only been tested for stoichiometric surfaces, but did not take into account that the equilibrium structure at the surface of a material might favour defect formation as found in this work.

Overall, bulk descriptors have been employed successfully in different material classes to describe, screen and predict the catalytic activity of materials and led to development of materials with high activity.[9,10] This work highlights, however, that the surface electronic structure and stoichiometry of a catalyst can behave very differently. As a consequence, bulk based descriptors are less accurate and the direct connection to an activity determining mechanism at the surface of a catalyst is elusive. For the rational

design of highly effective catalysts, mechanistic insight about the OER is needed to develop material design guidelines.

6.1. OER Activity of $LiMn_2O_4$

Since the OER happens at the surface of a catalyst, the measured activity should be dependent on the properties of the catalyst surface. It was shown previously that the shell Mn valence and hence the Mn e_g occupancy changes during catalytic cycling, but does not change during delithiation within the standard deviation of the measurements. Since the valence determination of particle shells by EELS is not very accurate with measured standard deviations of single measurements of 0.2 a larger or smaller Mn valence change than indicated by the averaged numbers is possible during OER, ranging from 0.2 to 1.0. Nonetheless, the EEL and XPS spectra in conjunction with the estimated amount of dissolved Mn clearly indicate oxidation of particle shells and thereby a decrease of the Mn e_g occupancy due to Mn loss. If Mn e_g occupancy is activity determining, it is expected, that the measured OER activity changes significantly during electrochemical cycling. The following paragraphs highlight that the measured activity change during cycling is smaller than expected from the shell e_g occupancy change, which indicates that Mn e_g occupancy as a single descriptor is not sufficient to govern OER mechanisms in this case.

RRDE measurements allow detecting O or Mn as reaction products via the ring electrode.[23] Fig. 6.1 shows the measured oxygen product current of the cycles 1, 5 and 10. The measured currents are proportional to the amount of evolved oxygen,[90] and thus, are a more reliable measure of the OER activity than the corresponding disk currents in Fig. 5.5a, which also contain processes like Mn dissolution.

Comparison of cycle 1 and 10 in Fig. 6.1 shows that the O detection current at a disk potential of 1.6 V decreases with a step from cycle one to cycle two and then gradually in total by 44%. Decreasing O evolution currents can either be caused by a decreasing intrinsic activity of the catalyst or by a reduction of the active surface area of the catalyst. The latter can be caused by formation of oxygen bubbles in catalyst pores which, block active sites from electrolyte contact[23,172–174] or by mechanical detachment of active material during catalysis.[172]

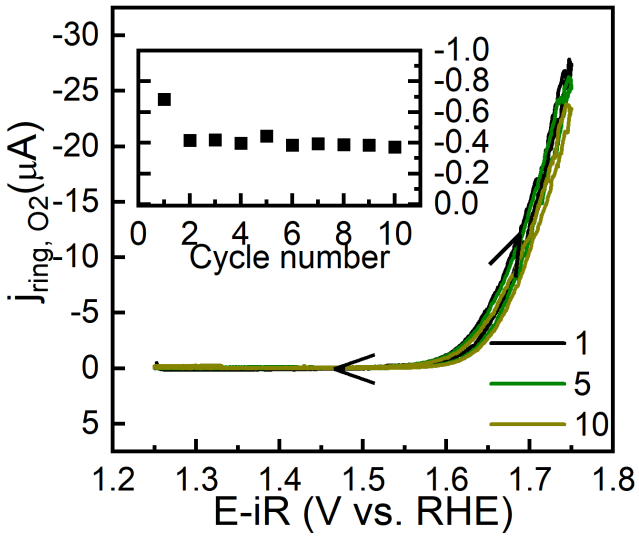

Figure 6.1.: Ring currents set to O detection of cycles 1, 5, and 10 of the CV experiment (Disk currents plotted in Fig. 5.5). The inset shows the measured currents for each cycle evaluated at a disk potential of 1.6 V. The electrochemical experiments have been performed by Max Baumung, currents are total product currents and not normalized to the electrode or oxide surface area.

Detachment of a large amount of material would result in a sudden drop of the disk currents[172] which was not observed in Fig. 5.5a. The effect of O bubble formation was studied using electrodes containing IrO_2 nanoparticles.[172–174] Accumulation of oxygen bubbles leads to decreasing disk and O detection currents at a set potential but the currents (partially) recover, if accumulated O bubbles are removed.[172,173] It was observed that the amount of active surface passivation through O bubbles scales with the applied current density, and that a relatively small critical disk current density of 0.45 mA/cm^2 already affects the measured O detection currents. Although, this critical current depends presumably on the electrodes' microstructure and porosity[173] its value is one order of magnitude smaller than the applied disk currents during OER experiments in Fig. 5.5a. Holding an electrode at disk current densities of 5 mA/cm^2 lead to a decrease of oxygen detection currents by 20% due to bubble formation within 30 s.[173] In the electrochemical experiments, disk current densities of more than 3 mA/cm^2 were exceeded for approximately 40 s, meaning that bubble formation is a possible explanation for the measured 22% decrease of oxygen detection currents.

The surface area of the sample used for catalytic experiments (Fig. 6.1) has not been

measured with the same protocol that Wei *et al.*[16] used. This means that measured data can only be compared qualitatively to literature data. An analysis by Omeshwari Bisen of the reported e_g-activity trend[9,16] (E =1.6 V) compared to measured activity of different $LiMn_2O_4$ samples showed that a change of the e_g occupancy of $\Delta e_g = 1$ results in a current change by a factor of 100 (unpublished). This trend was also confirmed by scaling the measured O product currents to the total disk currents.[23, 34, 90] Since the O product currents (ring currents) are a more direct measure of the O evolution, they are discussed further on.

Due to dissolution of tetrahedral Mn defects, an e_g occupancy change of 0.29 of octahedral Mn was estimated on basis of EELS and measured Mn product curents from OER onset to complete tetrahedral Mn dissolution. An analysis of the data of Wei *et al.*[16] by Omeshwari Bisen shows an exponential relationship between measured catalytic currents at a disc potential of 1.6 V and the e_g occupancy of the catalyst. A change of $\Delta e_g = 1$ yields to a catalytic current change by a factor of approximately 100 and thus a dependency of:

$$I_{@1.6V} = I_0 \cdot 100^{\Delta e_g}.$$

Applying the literature e_g-activity trend to particle shells leads to an expected O current decrease by a factor of 3.9 from cycle one to ten. If one includes the uncertainty of valence determination of particle shells, a current decrease by factor between 1.6 and 9.6 is within the range of the standard deviation. At the potential of 1.6 V, an O product current drop from 0.684 µA to 0.17 µA would be expected using the measured e_g change. This is larger by a factor of 2.2 than the measured current decrease by a factor of 1.8 from 0.684 µA to 0.373 µA at cycle ten on the basis of the estimated shell composition change based on averaged Mn valences. Thus, the OER activity change is smaller than expected from the estimated shell e_g occupancy change. With bubble formation as possible reason for an activity decrease, that means that the shell Mn e_g occupancy has a small or almost no influence on the OER activity of pristine particles. Interestingly, the core Mn e_g occupancy scales with the measured OER activity during cycling. The core Mn valence stayed constant within the measurement uncertainty during electrochemical cycling and accordingly, the OER activity stayed approximately constant as expected.[16]

This raises the question, whether octahedral e_g occupancy is a well suited descriptor for the OER activity of $LiMn_2O_4$. Within the limits of the shell structure model that comprises all measurements but lacks capability to resolve the surface structure with high accuracy it is indicated that Mn e_g occupancy does not describe the OER catalytic behaviour of $LiMn_2O_4$ well. In the following paragraphs the consequences of Mn e_g occupancy as a descriptor will be discussed under the assumption that the constructed model of shell structural changes is valid.

As a consequence, Mn e_g occupancy is either not a suitable descriptor in this case and thus is not able to relate to OER mechanisms in general, or surface properties are less important and OER activity is rather governed by bulk properties. Since OER catalysis is happening at the particle surfaces, the shell properties ought to be superior to bulk properties in determining OER activity. On this account, it has to be concluded that e_g occupancy[16] does not determine activity as single descriptor which is supported by literature studies where activity either failed to correlate with e_g occupancy,[10,175] or where a better agreement with other structural or electronic descriptors was found.[14,17,176,177] As a consequence, bulk e_g occupancy might indeed correlate with OER activity in limited cases, but cannot fully explain the mechanisms of the OER.

Since descriptors are established as property-activity correlations,[171] they are not necessarily cause-effect relationships. Thus, it is difficult to distinguish between material parameters that directly affect the OER reaction mechanisms from ones that just correlate with activity in certain cases. This is even more challenging if multiple parameters are changed at the same time, which is the case for the particle shell in this study. Since different properties of transition metal oxides, like e_g occupancy, are interlinked with each other activity-property correlations can exist without being linked to the reaction mechanisms. In $LiMn_2O_4$ for example, the lattice constants and thereby bond distances change when the Mn e_g occupancy and Mn-O covalence[10] change by delithiation[32,62] or by bulk defects (see Fig. 2.7). Another example is mechanical strain that leads to a shift of the metal *d*-band centre[44,45] or to splitting and preferential occupation of certain e_g orbitals[46] while changing bond distances.

Examples that do not show a clear relation between descriptor and reaction mechanism are the bulk formation energy[12] or the proposed descriptor μ/t. Here μ and t

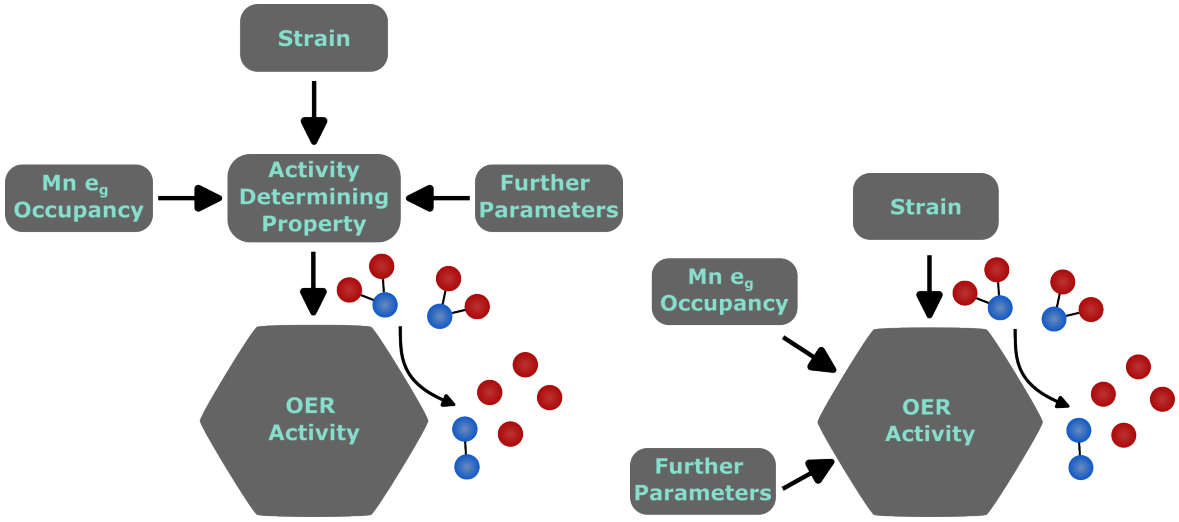

Figure 6.2.: Sketch of two possible relations of Mn e_g occupancy as OER descriptor. (a) Mn occupancy correlates with the actual activity determining material property. (b) Multiple properties determine activity together, the effect of e_g occupancy is partially mitigated by e.g. strain.

are the octahedral and tolerance factors and μ/t surpasses e_g occupancy by describing activity with higher statistical significance.[177] Both factors are calculated using the ionic radii and are defined for perovskites only. But no direct connection can be established, why a change of μ/t should impact a step in the OER reaction mechanism.[14] Presumably, an activity governing parameter is correlated with μ/t. That different descriptors are correlated with each other is also pointed out by a statistical analysis of 51 perovskites.[17] 14 activity-property correlations including metal-oxygen bond lengths, e_g occupancy, or charge transfer energy[17] were identified. Out of the 91 possible descriptor pairs, a strong correlation between two descriptors was found in 21 cases. Interestingly, the oxidation state exhibits the most correlations with other descriptors. Complex correlations between different descriptors impede to establish direct connections to activity determining factors.[17] Since no single descriptor was able to embrace the OER activity of all tested perovskite samples reliably and a set of seven descriptors was necessary to yield good statistical significance[17] it is either not possible to universally link the complex OER reaction kinetics to a single material property at all, or a potential universal descriptor was not covered in the analysis.

The lack of correlation between e_g occupancy and OER activity in this case can be

seen as a clue that e_g occupancy does only affect the catalytic mechanisms indirectly. This would suggest that e_g occupancy is related to a/the activity determining property but that it is not activity determining itself, as highlighted in Fig. 6.2a. If multiple descriptors are necessary to describe OER activity precisely, another possibility is that the influence of e_g occupancy is surpassed or mitigated by other factors, which are depicted in Fig. 6.2b. Due to the epitaxial core-shell relationship, the shells are strained if the e_g occupancy differs from the core. That strain has an impact on activity governing properties like intermediate adsorption energies[38,44,45,48] or directly on catalytic activity[42,178–180] has been investigated in a number of studies and applied to tune the activity of a specific material. The effect of compressive or tensile strain on the activity of a catalyst is hard to predict.[14] If adsorption energies of reaction intermediates increase or decrease by strain depends on the *B*-site occupation in perovskites,[38] meaning that the effect of strain has to be calculated for an individual system. Thus, it is difficult to estimate how the 1% compressive shell strain will alter the activity of $LiMn_2O_4$ nanoparticles. An analysis of strained $LaNiO_3$ films by Antipin and Risch[14] shows that strain of 1% increases the overpotential at a constant current by 20 mV, which would lead to a current change of a factor of 2.2 assuming a Tafel slope of 60 mV/decade.[16] The influence of strain on oxygen adsorption energies can vary by a factor of 5 comparing different perovskite samples,[38] which means that different material systems can not be compared a priori. However, this value can be taken as a guideline for the magnitude of strain effects. The observed current mismatch of a factor of 2.2 between the measured O product current decrease and the expected current decrease by the e_g descriptor is of the same size. If compressive in-plane strain leads to a decreasing OER activity in $LiMn_2O_4$, it will partially counteract the expected activity change when tetrahedral Mn increases the octahedral e_g occupancy in pristine particle shells.

This highlights that e_g occupancy has to be questioned being a robust descriptor for OER activity. Due to the complicated core-shell geometry of the investigated $LiMn_2O_4$ nanoparticles, multiple factors change when the particles catalyse the OER. Other than Mn e_g occupancy and the core-shell crystal structure and stoichiometry, further changes in the electronic structure can not be resolved by the conducted experiments, which makes it difficult to elucidate what other material properties can explain the observed catalytic behaviour. The O 2*p*-band centre for example, that recently gained attention as a more universal electronic structure based descriptor,[13,169,171,181] requires

band structure calculations to be measured. In order to establish reliable connections between simulated quantities and measured activity, the surfaces of the catalyst must be investigated with high resolution to ensure that the simulations reflect the actual surface structure.

7. Conclusion

Identifying correlations between a material property and its efficiency as a catalyst for the OER is an established approach used to identify guidelines for the design of environmentally friendly, abundant and favourably priced catalysts.[9,10,16,17,26,31,171,181] In order to establish reliable correlations between the OER activity and the catalysts material properties, so-called descriptors, a thorough investigation of the catalysts structure is necessary. Experiments that resolve the microstructure of $LiMn_2O_4$ nanoparticles, which are used as an OER model catalyst, were discussed and presented in this thesis. Within the associated research project C05 of the SFB1073, $LiMn_2O_4$ has been used to investigate how different factors like the particle size,[90] electrolyte pH,[91] or the manganese oxidation state[34] impact the OER catalytic behaviour and activity of this material. Complementary to these experiments with focus on electrochemistry, this thesis focused on resolving the crystal and electronic structure of $LiMn_2O_4$ nanoparticles with TEM as a core method. The structure of $LiMn_2O_4$ nanoparticles has been investigated in pristine state, after delithiation and after OER catalysis.
The main findings are:

- Pristine $LiMn_2O_4$ nanoparticles have a core-shell structure in terms of the Mn oxidation state, where Mn has a lower valence in a 3 nm thick shell. With the help of EELS simulations, it could be resolved that Mn defects, which partially replace Li on tetrahedral sites, cause the observed shell reduction.

- Although, Jahn-Teller distortions are expected for the measured shell oxidation state of $Mn^{2.9(2)+}$, the shell crystal structure is still cubic spinel and epitaxially connected to the particle's core. This induces compressive in-plane strain in the shell.

- Electrochemical delithiation leads to the expected core oxidation. However, a reduced shell is still present.

- Tetrahedral Mn is dissolved out of shells of pristine particles during OER cata-

lysis, predominantly in the first three cycles, thereby causing an increase of the shell Mn oxidation state.

- Comparing measured activity changes during OER catalysis of pristine $LiMn_2O_4$ with the shell e_g occupancy raises the question whether shell octahedral e_g occupancy is a sufficient descriptor for OER activity.

The fact that stoichiometry, defect structure and as a result the Mn oxidation state in the shell differ from the particle core, highlights the need to investigate the catalysts´ surface structure if property-activity correlations are to be established. Often bulk properties are linked to catalytic activity,[10,16,26] but the surface properties should have superior influence on the mechanisms of the catalytic reaction. The results of this thesis clearly demonstrate that bulk properties do not a priori describe the surface of a catalyst accurately. Thus, it has to be questioned if it is possible to draw conclusions about the mechanisms of the OER by previously reported bulk property-activity correlations.

Particle shells transform when used for OER catalysis. Tetrahedral site population and Mn oxidation state change by dissolution of Mn^{2+} defects. This could be stated by ex-situ TEM and XPS measurements of particles used for OER catalysis and by an analysis of the product currents measured during the reaction. It was evaluated that these changes happen predominantly in the first three out of ten cycles, which means that surface structure changes happen instantly when this material is used to catalyse the OER. Even if the surface structure of a catalyst has been investigated prior to OER catalysis, it cannot be assumed that the catalyst's state when activity is measured (e.g. in the third cycle[16]) is identical to the state during pre characterization. Thus, not characterizing the catalyst after electrochemical cycling imposes an additional possible error in governing the properties of the catalyst during OER, and not prior to OER. To understand the surface structure changes in more detail, one approach could be to perform TEM and XPS experiments after each cycle to monitor the Mn dissolution and valence changes with higher resolution in time.

Comparison of the structural changes of the particle shells with the OER activity trend leads to the idea that either Mn e_g occupancy, which has been proposed as OER descriptor,[9,16] does not have a direct influence on the OER mechanism or that its effect is mitigated by other important parameters like strain and strain induced band shifts,[38] or suppressed Jahn-Teller distortions.[182] The epitaxial core-shell relationship prevents

the shell structure to form its equilibrium crystal structure, which can be seen as a clue for the importance of connections between electronic and crystal structure of a catalyst. To further support the hypothesis that an expected activity change due to tetrahedral Mn defects is mitigated by constraining the crystal structure, it is necessary to understand how tetrahedral Mn defects and mechanical strain affect the electronic structure or O^* adsorption energies of $LiMn_2O_4$. That calls for further DFT calculations of this material with explicit focus on connections of crystal and electronic structure.

The hypothesis that surface e_g occupancy is not directly related to OER activity calls for further investigation of the shell structure evolution during OER of delithiated particles. This might lead to a better understanding about how significantly the investigated particles contradict the literature trends,[9,16] and about what factors determine activity of $Li_xMn_2O_4$. Interestingly, Mn defects are preserved in the shell after delithiation and Mn dissolution was detected during OER on delithiated samples as well, albeit less pronounced.[34] Although the surface stoichiometry of delithiated $Li_xMn_2O_4$ particles is identical to pristine ones, the OER activity is smaller.[34] Being able to resolve how the surfaces of delithiated particles differ from pristine ones when catalysing the OER might thus be a guideline towards understanding what governs OER activity in $Li_xMn_2O_4$.

It was possible to deduce, that the shell structure of $LiMn_2O_4$ particles changes when used for catalysing the OER from ex-situ experiments. Although, it is not possible to make statements about the structure of particle surfaces when they are actively catalysing the OER. It has been shown that in-situ ETEM experiments are able to resolve ad-atom surface dynamics of a catalyst in a water atmosphere, thereby gaining a more direct picture of the active surface of a catalyst.[163] A first step in this direction are the TEM experiments in water atmosphere that have been presented in this thesis. They have been successful in reproducing surface oxidation, but time resolution or a gradual change of surfaces could not be resolved yet. Therefore, further in-situ experiments are a promising approach in relating the catalytic activity of $LiMn_2O_4$ to the properties of an active surface.

A. Appendix

Material	$LiMn_2O_4$	Mn_3O_4	Mn_3O_4
Peak	111	103	224
$\|F\|$	189.876	127.199	213.584
p	8	8	8
2θ	18.6493	32.3945	59.9381

Table A.1.: Values for XRD peak intensity calculation to calculate the maximum Mn_3O_4 volume share in the used $LiMn_2O_4$ powder.

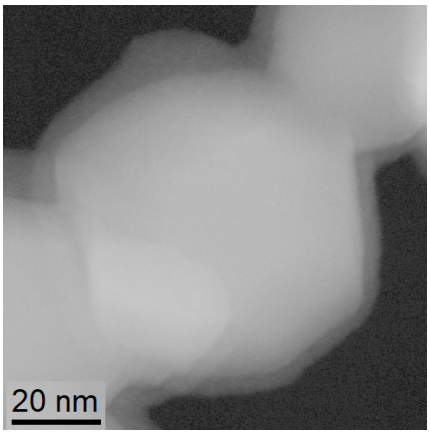

Figure A.1.: STEM overview image after the tenth scan of repeated EELS measurements at one particle location.

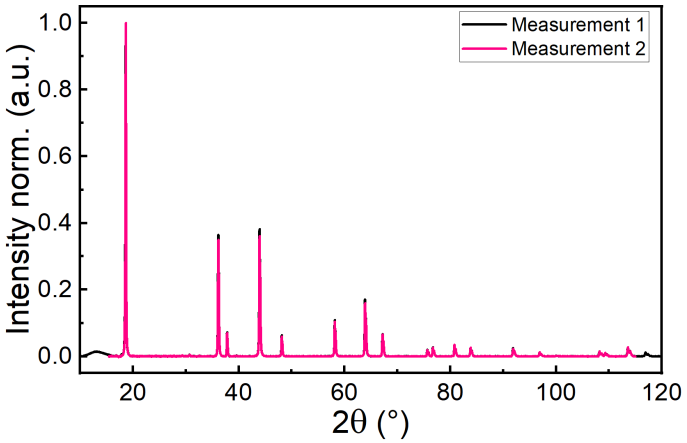

Figure A.2.: Comparison of two XRD diffractograms of pristine $LiMn_2O_4$ powder taken with a time delay of approximately two years.

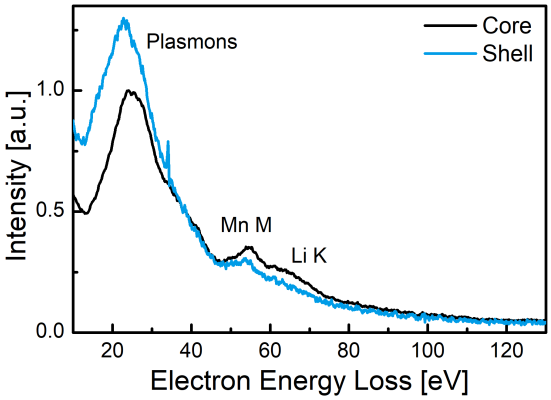

Figure A.3.: Representative EEL low-loss spectra after background subtraction of core and shell from a pristine particle showing the Mn M and Li K edge.

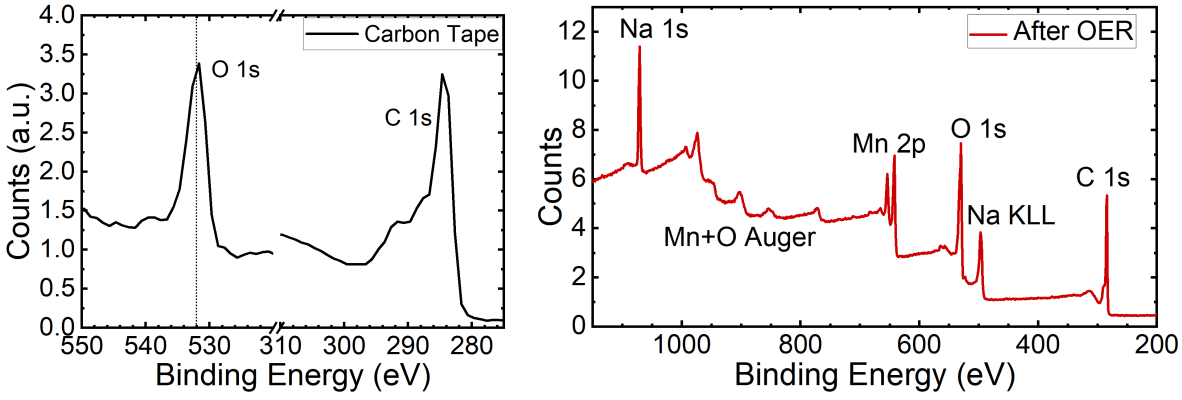

(a) (b)

Figure A.4.: XPS spectra of carbon tape used as support for powder measurements (a) and XPS overview spectrum of electrochemical cycled $LiMn_2O_4$ powder (b).

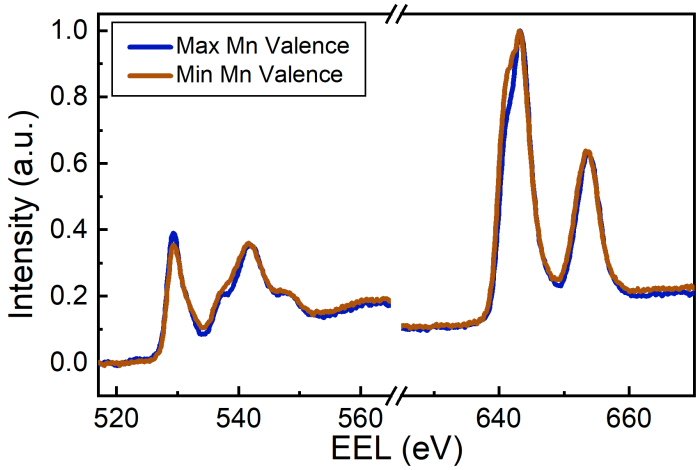

Figure A.5.: EEL spectra of pristine particle cores from the particles with highest and lowest measured Mn oxidation state. The intensity has been normalized to 1.

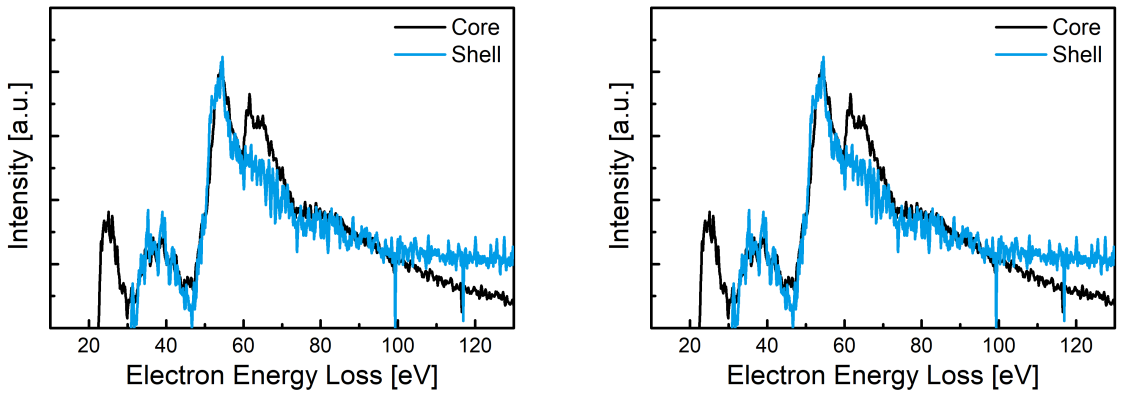

(a) (b)

Figure A.6.: STEM-EEL low-loss spectra of two cycled particles of core and shell regions displaying the Mn M edge at 50 eV and the Li K edge at 60 eV. Both spectra are collected from particles that where surface changes were found after electrochemical cycling.

Bibliography

[1] J. Rogelj, D. Shindell, K. Jiang, S. Fifita, P. Forster, V. Ginzburg, C. Handa, H. Kheshgi, S. Kobayashi, E. Kriegler, L. Mundaca, R. Seferian, and M. Vilarino, in *Glob. Warm. 1.5°C* (Cambridge University Press, 2022) pp. 93–174.

[2] T. Devezas, D. LePoire, J. C. Matias, and A. M. Silva, Futures **40**, 1 (2008).

[3] H.-W. Sinn, Eur. Econ. Rev. **99**, 130 (2017).

[4] W. A. Braff, J. M. Mueller, and J. E. Trancik, Nat. Clim. Chang. **6**, 964 (2016).

[5] M. Becherif, H. Ramadan, K. Cabaret, F. Picard, N. Simoncini, and O. Bethoux, Energy Procedia **74**, 371 (2015).

[6] J. Andrews and B. Shabani, Int. J. Hydrogen Energy **37**, 1184 (2012).

[7] J. Melder, P. Bogdanoff, I. Zaharieva, S. Fiechter, H. Dau, and P. Kurz, Zeitschrift für Phys. Chemie **234**, 925 (2020).

[8] S. Trasatti, J. Electroanal. Chem. **111**, 125 (1980).

[9] J. Suntivich, K. J. May, H. A. Gasteiger, J. B. Goodenough, and Y. Shao-Horn, Science (80-.). **334**, 1383 (2011), arXiv:1111.3644 .

[10] Y. Sun, H. Liao, J.-O. J. Wang, B. Chen, S. Sun, S. J. H. Ong, S. Xi, C. Diao, Y. Du, J.-O. J. Wang, M. B. H. Breese, S. Li, H. Zhang, and Z. J. Xu, Nat. Catal. **3**, 554 (2020).

[11] I. C. Man, H. Su, F. Calle-Vallejo, H. A. Hansen, J. I. Martínez, N. G. Inoglu, J. Kitchin, T. F. Jaramillo, J. K. Nørskov, and J. Rossmeisl, ChemCatChem **3**, 1159 (2011).

[12] F. Calle-Vallejo, O. A. Díaz-Morales, M. J. Kolb, and M. T. M. Koper, ACS Catal. **5**, 869 (2015).

[13] H. Wang, K. H. L. Zhang, J. P. Hofmann, V. A. de la Peña O'Shea, and F. E. Oropeza, J. Mater. Chem. A **9**, 19465 (2021).

[14] D. Antipin and M. Risch, J. Phys. Energy **2**, 032003 (2020).

[15] W. T. Hong, M. Risch, K. A. Stoerzinger, A. Grimaud, J. Suntivich, and Y. Shao-Horn, Energy Environ. Sci. **8**, 1404 (2015).

[16] C. Wei, Z. Feng, G. G. Scherer, J. Barber, Y. Shao-Horn, and Z. J. Xu, Adv. Mater. **29**, 1606800 (2017).

[17] W. T. Hong, R. E. Welsch, and Y. Shao-Horn, J. Phys. Chem. C **120**, 78 (2016).

[18] D. M. Robinson, Y. B. Go, M. Mui, G. Gardner, Z. Zhang, D. Mastrogiovanni, E. Garfunkel, J. Li, M. Greenblatt, and G. C. Dismukes, J. Am. Chem. Soc. **135**, 3494 (2013).

[19] P. F. Smith, B. J. Deibert, S. Kaushik, G. Gardner, S. Hwang, H. Wang, J. F. Al-Sharab, E. Garfunkel, L. Fabris, J. Li, and G. C. Dismukes, ACS Catal. **6**, 2089 (2016).

[20] C. W. Cady, G. Gardner, Z. O. Maron, M. Retuerto, Y. B. Go, S. Segan, M. Greenblatt, and G. C. Dismukes, ACS Catal. **5**, 3403 (2015).

[21] T. Takashima, K. Hashimoto, and R. Nakamura, J. Am. Chem. Soc. **134**, 1519 (2012).

[22] M. V. Abrashev, P. Chernev, P. Kubella, M. R. Mohammadi, C. Pasquini, H. Dau, and I. Zaharieva, J. Mater. Chem. A **7**, 17022 (2019).

[23] L. Köhler, M. Ebrahimizadeh Abrishami, V. Roddatis, J. Geppert, and M. Risch, ChemSusChem **10**, 4479 (2017).

[24] M. Huynh, C. Shi, S. J. Billinge, and D. G. Nocera, J. Am. Chem. Soc. **137**, 14887 (2015).

[25] M. Risch, K. A. Stoerzinger, B. Han, T. Z. Regier, D. Peak, S. Y. Sayed, C. Wei, Z. Xu, and Y. Shao-Horn, J. Phys. Chem. C **121**, 17682 (2017).

[26] R. Jacobs, J. Hwang, Y. Shao-Horn, and D. Morgan, Chem. Mater. **31**, 785 (2019).

[27] R. Benedek and M. M. Thackeray, Phys. Rev. B **83**, 195439 (2011).

[28] M. Eckhoff and J. Behler, J. Chem. Phys. **155**, 244703 (2021), arXiv:2109.14068 .

[29] C. Baeumer, J. Li, Q. Lu, A. Y.-L. Liang, L. Jin, H. P. Martins, T. Duchoň, M. Glöß, S. M. Gericke, M. A. Wohlgemuth, M. Giesen, E. E. Penn, R. Dittmann, F. Gunkel, R. Waser, M. Bajdich, S. Nemšák, J. T. Mefford, and W. C. Chueh, Nat. Mater. **20**, 674 (2021).

[30] K. A. Stoerzinger, L. Qiao, M. D. Biegalski, and Y. Shao-Horn, J. Phys. Chem. Lett. **5**, 1636 (2014).

[31] J. Suntivich, H. A. Gasteiger, N. Yabuuchi, H. Nakanishi, J. B. Goodenough, and Y. Shao-Horn, Nat. Chem. **3**, 546 (2011).

[32] M. Eckhoff, F. Schönewald, M. Risch, C. A. Volkert, P. E. Blöchl, and J. Behler, Phys. Rev. B **102**, 174102 (2020), arXiv:2007.00327 .

[33] M. M. Thackeray, Prog. Solid State Chem. **25**, 1 (1997), arXiv:0402594v3 [arXiv:cond-mat] .

[34] M. Baumung, *Georg. Univ. Sch. Sci.*, Dissertation, Georg-August-University Göttingen (2021).

[35] H. Dau, C. Limberg, T. Reier, M. Risch, S. Roggan, and P. Strasser, ChemCatChem **2**, 724 (2010).

[36] F. Calle-Vallejo, N. G. Inoglu, H.-Y. Su, J. I. Martínez, I. C. Man, M. T. M. Koper, J. R. Kitchin, and J. Rossmeisl, Chem. Sci. **4**, 1245 (2013).

[37] M. T. Koper, J. Electroanal. Chem. **660**, 254 (2011).

[38] S. A. Akhade and J. R. Kitchin, J. Chem. Phys. **137**, 084703 (2012).

[39] A. Grimaud, K. J. May, C. E. Carlton, Y. L. Lee, M. Risch, W. T. Hong, J. Zhou, and Y. Shao-Horn, Nat. Commun. **4**, 1 (2013).

[40] Y. Duan, S. Sun, S. Xi, X. Ren, Y. Zhou, G. Zhang, H. Yang, Y. Du, and Z. J. Xu, Chem. Mater. **29**, 10534 (2017).

[41] Y. Zhou, S. Sun, J. Song, S. Xi, B. Chen, Y. Du, A. C. Fisher, F. Cheng, X. Wang, H. Zhang, and Z. J. Xu, Adv. Mater. **30**, 1802912 (2018).

[42] L. Wang, K. A. Stoerzinger, L. Chang, X. Yin, Y. Li, C. S. Tang, E. Jia, M. E. Bowden, Z. Yang, A. Abdelsamie, L. You, R. Guo, J. Chen, A. Rusydi, J. Wang, S. A. Chambers, and Y. Du, ACS Appl. Mater. Interfaces **11**, 12941 (2019).

[43] S. Maiti, K. Maiti, M. T. Curnan, K. Kim, K.-J. Noh, and J. W. Han, Energy Environ. Sci. **14**, 3717 (2021).

[44] S. Schnur and A. Groß, Phys. Rev. B **81**, 033402 (2010).

[45] S. A. Akhade and J. R. Kitchin, J. Chem. Phys. **135** (2011), 10.1063/1.3631948.

[46] D. Pesquera, G. Herranz, A. Barla, E. Pellegrin, F. Bondino, E. Magnano, F. Sánchez, and J. Fontcuberta, Nat. Commun. **3**, 1 (2012).

[47] J. R. Kitchin, J. K. Nørskov, M. A. Barteau, and J. G. Chen, Phys. Rev. Lett. **93**, 156801 (2004).

[48] M. Mavrikakis, B. Hammer, and J. K. Nørskov, Phys. Rev. Lett. **81**, 2819 (1998).

[49] P. Moseley and W. A. Curtin, Nano Lett. **15**, 4089 (2015).

[50] J. R. Kitchin, J. K. Nørskov, M. A. Barteau, and J. G. Chen, J. Chem. Phys. **120**, 10240 (2004).

[51] J. Lee, S.-Y. Jun, T. Choi, D. Jung, J.-S. Bae, S. A. Lee, and W. S. Choi, Appl. Phys. Lett. **117**, 163906 (2020).

[52] P. Strobel, G. Rousse, A. Ibarra-Palos, and C. Masquelier, J. Solid State Chem. **177**, 1 (2004).

[53] D. Wickham and W. Croft, J. Phys. Chem. Solids **7**, 351 (1958).

[54] J. C. Hunter, J. Solid State Chem. **39**, 142 (1981).

[55] M. M. Thackeray, P. J. Johnson, L. A. de Picciotto, P. G. Bruce, and J. B. Goodenough, Mater. Res. Bull. **19**, 179 (1984).

[56] M. Thackeray, W. David, P. Bruce, and J. Goodenough, Mater. Res. Bull. **18**, 461 (1983).

[57] M. Yonemura, A. Yamada, H. Kobayashi, M. Tabuchi, T. Kamiyama, Y. Kawamoto, and R. Kanno, J. Mater. Chem. **14**, 1948 (2004).

[58] T. Ohzuku, M. Kitagawa, and T. Hirai, J. Electrochem. Soc. **136**, 3169 (1989).

[59] R. Gummow, A. de Kock, and M. Thackeray, Solid State Ionics **69**, 59 (1994).

[60] A. V. der Ven, C. Marianetti, D. Morgan, and G. Ceder, Solid State Ionics **135**, 21 (2000).

[61] H. Berg and J. O. Thomas, Solid State Ionics **126**, 227 (1999).

[62] F. Schönewald, *TEM and STEM-EELS investigations of Li1Mn2O4 nanoparticles*, Masters thesis, Georg-August Universität Göttingen (2019).

[63] T. Eriksson, A. K. Hjelm, G. Lindbergh, and T. Gustafsson, J. Electrochem. Soc. **149**, 1164 (2002).

[64] Y. Xia, T. Sakai, T. Fujieda, X. Q. Yang, X. Sun, Z. F. Ma, J. McBreen, and M. Yoshio, J. Electrochem. Soc. **148**, A723 (2001).

[65] X. Q. Yang, X. Sun, S. J. Lee, J. McBreen, S. Mukerjee, M. L. Daroux, and X. Xing, Electrochem. Solid-State Lett. **2**, 157 (1999).

[66] A. Paolone, C. Castellano, R. Cantelli, G. Rousse, and C. Masquelier, Phys. Rev. B - Condens. Matter Mater. Phys. **68**, 1 (2003).

[67] G. Rousse and C. Masquelier, Chem. Mater. **11**, 3629 (1999).

[68] A. Yamada and M. Tanaka, Mater. Res. Bull. **30**, 715 (1995).

[69] J. Rodríguez-Carvajal, G. Rousse, C. Masquelier, and M. Hervieu, Phys. Rev. Lett. **81**, 4660 (1998).

[70] V. Massarotti, D. Capsoni, M. Bini, P. Scardi, M. Leoni, V. Baron, and H. Berg, J. Appl. Crystallogr. **32**, 1186 (1999).

[71] C. Y. Ouyang, S. Q. Shi, and M. S. Lei, J. Alloys Compd. **474**, 370 (2009).

[72] R. Kanno, M. Yonemura, T. Kohigashi, Y. Kawamoto, M. Tabuchi, and T. Kamiyama, J. Power Sources **97-98**, 423 (2001).

[73] M. Kopec, J. Dygas, F. Krok, A. Mauger, F. Gendron, and C. Julien, J. Phys. Chem. Solids **69**, 955 (2008).

[74] C. Masquelier, M. Tabuchi, K. Ado, R. Kanno, Y. Kobayashi, Y. Maki, O. Nakamura, and J. B. Goodenough, J. Solid State Chem. **123**, 255 (1996).

[75] Y. Gao and J. R. Dahn, J. Electrochem. Soc. **143**, 100 (1996).

[76] X. Hao, O. Gourdon, B. J. Liddle, and B. M. Bartlett, J. Mater. Chem. **22**, 1578 (2012).

[77] Y. Xia and M. Yoshio, J. Electrochem. Soc. **143**, 825 (1996).

[78] M. Thackeray, A. de Kock, and W. David, Mater. Res. Bull. **28**, 1041 (1993), arXiv:arXiv:1310.3244v1 .

[79] T. Buhrmester, *Zur Fehlordnung im System Li1+xMn2-yO4-d*, Dissertation, Technische Universität Darmstadt (2001).

[80] T. Kanasaku, K. Amezawa, and N. Yamamoto, Solid State Ionics **133**, 51 (2000).

[81] D. Tang, Y. Sun, Z. Yang, L. Ben, L. Gu, and X. Huang, Chem. Mater. **26**, 3535 (2014).

[82] X. Gao, Y. H. Ikuhara, C. A. J. Fisher, R. Huang, A. Kuwabara, H. Moriwake, K. Kohama, and Y. Ikuhara, J. Mater. Chem. A **7**, 8845 (2019).

[83] T. Liu, A. Dai, J. Lu, Y. Yuan, Y. Xiao, L. Yu, M. Li, J. Gim, L. Ma, and J. et al. Liu, Nat. Commun. **10**, 4721 (2019).

[84] K. Momma and F. Izumi, J. Appl. Crystallogr. **44**, 1272 (2011).

[85] C. D. Amos, M. A. Roldan, M. Varela, J. B. Goodenough, and P. J. Ferreira, Nano Lett. **16**, 2899 (2016).

[86] Y. H. Ikuhara, Y. Iwamoto, K. Kikuta, and S.-i. Hirano, J. Mater. Res. **14**, 3102 (1999).

[87] K. Hoang, J. Mater. Chem. A **2**, 18271 (2014), arXiv:1412.5264 .

[88] R. Huang, Y. H. Ikuhara, T. Mizoguchi, S. D. Findlay, A. Kuwabara, C. A. J. Fisher, H. Moriwake, H. Oki, T. Hirayama, and Y. Ikuhara, Angew. Chemie Int. Ed. **50**, 3053 (2011).

[89] F. Schönewald, M. Eckhoff, M. Baumung, M. Risch, P. E. Blöchl, J. Behler, and C. A. Volkert, "A criticial view on e$_g$ occupancy as a descriptor for oxygen evolution catalytic activity in LiMn$_2$O$_4$ nanoparticles," (2020), arXiv:2007.04217 .

[90] M. Baumung, F. Schönewald, T. Erichsen, C. A. Volkert, and M. Risch, Sustain. Energy Fuels **3**, 2218 (2019).

[91] M. Baumung, L. Kollenbach, L. Xi, and M. Risch, ChemPhysChem , 1 (2019).

[92] R. Egerton, *Electron Energy-Loss Spectroscopy in the Electron Microscope*, 3rd ed. (Springer US, Boston, MA, 2011).

[93] F. M. De Groot, M. Grioni, J. C. Fuggle, J. Ghijsen, G. A. Sawatzky, and H. Petersen, Phys. Rev. B **40**, 5715 (1989), arXiv:U .

[94] R. D. Leapman, L. A. Grunes, and P. L. Fejes, Phys. Rev. B **26**, 614 (1982).

[95] T. Sparrow, B. Williams, C. Rao, and J. Thomas, Chem. Phys. Lett. **108**, 547 (1984).

[96] H. Kurata and C. Colliex, Phys. Rev. B **48**, 2102 (1993).

[97] L. Laffont and P. Gibot, Mater. Charact. **61**, 1268 (2010).

[98] M. Varela, M. P. Oxley, W. Luo, J. Tao, M. Watanabe, A. R. Lupini, S. T. Pantelides, and S. J. Pennycook, Phys. Rev. B **79**, 085117 (2009).

[99] J. Graetz, C. C. Ahn, H. Ouyang, P. Rez, and B. Fultz, Phys. Rev. B - Condens. Matter Mater. Phys. **69**, 1 (2004), arXiv:0406561 [cond-mat] .

[100] H. Tan, J. Verbeeck, A. Abakumov, and G. Van Tendeloo, Ultramicroscopy **116**, 24 (2012).

[101] S. Zhang, K. J. T. Livi, A.-C. Gaillot, A. T. Stone, and D. R. Veblen, Am. Mineral. **95**, 1741 (2010).

[102] G. A. BOTTON, C. C. APPEL, A. HORSEWELL, and W. M. STOBBS, J. Microsc. **180**, 211 (1995).

[103] T. Riedl, T. Gemming, and K. Wetzig, Ultramicroscopy **106**, 284 (2006).

[104] T. Erichsen, B. Pfeiffer, V. Roddatis, and C. A. Volkert, ACS Appl. Energy Mater. , acsaem.0c00380 (2020).

[105] T. Yamaguchi, S. Shibuya, S. Suga, and S. Shin, J. Phys. C Solid State Phys. **15**, 2641 (1982).

[106] F. M. F. de Groot, J. C. Fuggle, B. T. Thole, and G. A. Sawatzky, Phys. Rev. B **42**, 5459 (1990).

[107] M. Sotoudeh, S. Rajpurohit, P. Blöchl, D. Mierwaldt, J. Norpoth, V. Roddatis, S. Mildner, B. Kressdorf, B. Ifland, and C. Jooss, Phys. Rev. B **95**, 235150 (2017), arXiv:1610.07548 .

[108] S. Nyquist and U. Hålenius, Phys. Chem. Miner. **41**, 255 (2014).

[109] K. van Benthem and H. Kohl, Micron **31**, 347 (2000).

[110] F. A. Stevie and C. L. Donley, J. Vac. Sci. Technol. A **38**, 063204 (2020).

[111] A. G. Shard, Surf. Interface Anal. **46**, 175 (2014).

[112] M. P. Seah and W. A. Dench, Surf. Interface Anal. **1**, 2 (1979).

[113] S. Tougaard, "QUASES-IMFP-TPP2M Ver.3.0," (2016).

[114] G. H. Major, N. Fairley, P. M. A. Sherwood, M. R. Linford, J. Terry, V. Fernandez, and K. Artyushkova, J. Vac. Sci. Technol. A **38**, 061203 (2020).

[115] M. C. Biesinger, B. P. Payne, A. P. Grosvenor, L. W. Lau, A. R. Gerson, and R. S. C. Smart, Appl. Surf. Sci. **257**, 2717 (2011).

[116] G. Williamson and W. Hall, Acta Metall. **1**, 22 (1953).

[117] R. Egerton, P. Li, and M. Malac, Micron **35**, 399 (2004).

[118] S. Hettler, M. Dries, P. Hermann, M. Obermair, D. Gerthsen, and M. Malac, Micron **96**, 38 (2017).

[119] C. M. McGilvery, A. E. Goode, M. S. Shaffer, and D. W. McComb, Micron **43**, 450 (2012).

[120] A. Kumau, H. Hashimoto, K. Shiraishi, A. Kumao, H. Hashimoto, and K. Shiraishi, J. Electron Microsc. (Tokyo). **30**, 161 (1981).

[121] P. Hirsch, M. Kässens, M. Püttmann, and L. Reimer, Scanning **16**, 101 (1994).

[122] H. Seiler, J. Appl. Phys. **54**, R1 (1983).

[123] D. C. Joy, M. S. Prasad, and H. M. Meyer, J. Microsc. **215**, 77 (2004).

[124] K. J. Livi, B. Lafferty, M. Zhu, S. Zhang, A. C. Gaillot, and D. L. Sparks, Environ. Sci. Technol. **46**, 970 (2012).

[125] D. Tang, L. Ben, Y. Sun, B. Chen, Z. Yang, L. Gu, and X. Huang, J. Mater. Chem. A **2**, 14519 (2014).

[126] M. De Jong, W. Chen, T. Angsten, A. Jain, R. Notestine, A. Gamst, M. Sluiter, C. K. Ande, S. Van Der Zwaag, J. J. Plata, C. Toher, S. Curtarolo, G. Ceder, K. A. Persson, and M. Asta, Sci. Data **2**, 1 (2015).

[127] C. V. Ramana, M. Massot, and C. M. Julien, Surf. Interface Anal. **37**, 412 (2005).

[128] C. R. Brundle and B. V. Crist, J. Vac. Sci. Technol. A **38**, 041001 (2020).

[129] J. Töpfer, A. Feltz, D. Gräf, B. Hackl, L. Raupach, and P. Weissbrodt, Phys. Status Solidi **134**, 405 (1992).

[130] J. S. Foord, R. B. Jackman, and G. C. Allen, Philos. Mag. A **49**, 657 (1984).

[131] V. C. BOSE and V. BIJU, Bull. Mater. Sci. **38**, 865 (2015).

[132] O. Mykhailiv, H. Zubyk, and M. E. Plonska-Brzezinska, Inorganica Chim. Acta **468**, 49 (2017).

[133] R. Benedek, J. Phys. Chem. C **121**, 22049 (2017).

[134] J. Suntivich, H. A. Gasteiger, N. Yabuuchi, and Y. Shao-Horn, J. Electrochem. Soc. **157**, B1263 (2010).

[135] D. Mierwaldt, V. Roddatis, M. Risch, J. Scholz, J. Geppert, M. E. Abrishami, and C. Jooss, Adv. Sustain. Syst. **1**, 1700109 (2017).

[136] S. Mildner, M. Beleggia, D. Mierwaldt, T. W. Hansen, J. B. Wagner, S. Yazdi, T. Kasama, J. Ciston, Y. Zhu, and C. Jooss, J. Phys. Chem. C **119**, 5301 (2015).

[137] B. Chen, L. Ben, H. Yu, Y. Chen, and X. Huang, ACS Appl. Mater. Interfaces **10**, 550 (2018).

[138] S. DORRIS and T. MASON, J. Am. Ceram. Soc. **71**, 379 (1988).

[139] M. Eckhoff, P. E. Blöchl, and J. Behler, Phys. Rev. B **101**, 205113 (2020), arXiv:2001.10975 .

[140] M. V. Ganduglia-Pirovano, A. Hofmann, and J. Sauer, Surf. Sci. Rep. **62**, 219 (2007).

[141] R. Arabolla Rodríguez, M. González Montiel, N. Della Santina Mohallem, Y. Mosqueda Laffita, L. Andrey Montoro, M. Avila Santos, H. León Ramírez, and E. L. Pérez-Cappe, Solid State Ionics **369**, 115707 (2021).

[142] R. Arabolla Rodríguez, N. Della Santina Mohallem, M. Avila Santos, D. A. Sena Costa, L. Andrey Montoro, Y. Mosqueda Laffita, L. A. Tavera Carrasco, and E. L. Perez-Cappe, J. Power Sources **490**, 229519 (2021).

[143] C. Zuo, Z. Hu, R. Qi, J. Liu, Z. Li, J. Lu, C. Dong, K. Yang, W. Huang, C. Chen, Z. Song, S. Song, Y. Yu, J. Zheng, and F. Pan, Adv. Energy Mater. **10**, 1 (2020).

[144] P. C. S. U. Nikolaychuk (2015) pp. 120–123.

[145] M. Morcrette, P. Barboux, J. Perrière, T. Brousse, A. Traverse, and J. P. Boilot, Solid State Ionics **138**, 213 (2001).

[146] Z. Lu, X. Lu, J. Ding, T. Zhou, T. Ge, G. Yang, F. Yin, and M. Wu, Appl. Surf. Sci. **426**, 19 (2017).

[147] M. M. Thackeray, Y. Shao-Horn, A. J. Kahaian, K. D. Kepler, E. Skinner, J. T. Vaughey, and S. A. Hackney, Electrochem. Solid-State Lett. **1**, 7 (1998).

[148] R. Wang, X. Li, Z. Wang, and H. Guo, J. Solid State Electrochem. **20**, 19 (2016).

[149] Y. Xia, Y. Zhou, and M. Yoshio, J. Electrochem. Soc. **144**, 2593 (1997).

[150] C. Zhan, T. Wu, J. Lu, and K. Amine, Energy Environ. Sci. **11**, 243 (2018).

[151] R. Benedek, M. M. Thackeray, J. Low, and T. Bučko, J. Phys. Chem. C **116**, 4050 (2012).

[152] N. P. W. Pieczonka, Z. Liu, P. Lu, K. L. Olson, J. Moote, B. R. Powell, and J.-h. Kim, J. Phys. Chem. C **117**, 15947 (2013).

[153] H.-W. Chan, J.-G. Duh, and H.-S. Sheu, J. Electrochem. Soc. **153**, A1533 (2006).

[154] J. Sugiyama, T. Atsumi, T. Hioki, S. Noda, and N. Kamegashira, J. Alloys Compd. **235**, 163 (1996).

[155] H. Berg, J. O. Thomas, W. Liu, and G. C. Farrington, Solid State Ionics **112**, 165 (1998).

[156] H. Berg, H. Rundlöv, and J. O. Thomas, Solid State Ionics **144**, 65 (2001).

[157] H. T. Chung, S. T. Myung, T. H. Cho, and J. T. Son, J. Power Sources **97-98**, 454 (2001).

[158] J. Rockenberger, L. Troger, A. L. Rogach, M. Tischer, M. Grundmann, A. Eychmuller, and H. Weller, J. Chem. Phys. **108**, 7807 (1998).

[159] J. Park, W. Lu, and A. M. Sastry, J. Electrochem. Soc. **158**, A201 (2011).

[160] D. N. Madsen and J. P. Hansen, Renew. Sustain. Energy Rev. **114**, 109306 (2019).

[161] S. M. Ghodsi, S. Anand, R. Shahbazian-Yassar, T. Shokuhfar, and C. M. Megaridis, ACS Nano **13**, 4677 (2019).

[162] A. Opitz, M. Scherge, S. I. Ahmed, and J. A. Schaefer, J. Appl. Phys. **101** (2007), 10.1063/1.2712155.

[163] G. Lole, V. Roddatis, U. Ross, M. Risch, T. Meyer, L. Rump, J. Geppert, G. Wartner, P. Blöchl, and C. Jooss, Commun. Mater. **1**, 68 (2020).

[164] S. Raabe, D. Mierwaldt, J. Ciston, M. Uijttewaal, H. Stein, J. Hoffmann, Y. Zhu, P. Blöchl, and C. Jooss, Adv. Funct. Mater. **22**, 3378 (2012).

[165] A. Yamada, J. Solid State Chem. **122**, 160 (1996).

[166] V. Massarotti, D. Capsoni, M. Bini, G. Chiodelli, C. Azzoni, M. Mozzati, and A. Paleari, J. Solid State Chem. **131**, 94 (1997).

[167] H. Berg, K. Göransson, B. Noläng, and J. O. Thomas, J. Mater. Chem. **10**, 1437 (2000).

[168] E. M. Fernández, P. G. Moses, A. Toftelund, H. A. Hansen, J. I. Martínez, F. Abild-Pedersen, J. Kleis, B. Hinnemann, J. Rossmeisl, T. Bligaard, and J. K. Nørskov, Angew. Chemie Int. Ed. **47**, 4683 (2008).

[169] J. Hwang, Z. Feng, N. Charles, X. R. Wang, D. Lee, K. A. Stoerzinger, S. Muy, R. R. Rao, D. Lee, R. Jacobs, D. Morgan, and Y. Shao-Horn, Mater. Today **31**, 100 (2019).

[170] M. KOMO, A. HAGIWARA, S. TAMINATO, M. HIRAYAMA, and R. KANNO, Electrochemistry **80**, 834 (2012).

[171] L. Giordano, K. Akkiraju, R. Jacobs, D. Vivona, D. Morgan, and Y. Shao-Horn, Acc. Chem. Res. **55**, 298 (2022).

[172] H. A. El-Sayed, A. Weiß, L. F. Olbrich, G. P. Putro, and H. A. Gasteiger, J. Electrochem. Soc. **166**, F458 (2019).

[173] I. S. Filimonenkov, S. Y. Istomin, E. V. Antipov, G. A. Tsirlina, and E. R. Savinova, Electrochim. Acta **286**, 304 (2018).

[174] A. Maljusch, O. Conradi, S. Hoch, M. Blug, and W. Schuhmann, Anal. Chem. **88**, 7597 (2016).

[175] W. Li, F. Yang, and J. Zhang, J. Phys. Conf. Ser. **2393**, 012019 (2022).

[176] K. Toyoda, R. Hinogami, N. Miyata, and M. Aizawa, J. Phys. Chem. C **119**, 6495 (2015).

[177] B. Weng, Z. Song, R. Zhu, Q. Yan, Q. Sun, C. G. Grice, Y. Yan, and W.-J. J. Yin, Nat. Commun. **11**, 1 (2020).

[178] J. R. Petrie, V. R. Cooper, J. W. Freeland, T. L. Meyer, Z. Zhang, D. A. Lutterman, and H. N. Lee, J. Am. Chem. Soc. **138**, 2488 (2016).

[179] K. A. Stoerzinger, W. Seok Choi, H. Jeen, H. N. Lee, and Y. Shao-Horn, J. Phys. Chem. Lett. **6**, 487 (2015).

[180] M. Luo and S. Guo, Nat. Rev. Mater. **2**, 17059 (2017).

[181] J. Liu, H. Liu, H. Chen, X. Du, B. Zhang, Z. Hong, S. Sun, and W. Wang, Adv. Sci. **7** (2020), 10.1002/advs.201901614.

[182] S. Hirai, S. Yagi, A. Seno, M. Fujioka, T. Ohno, and T. Matsuda, RSC Adv. **6**, 2019 (2016).

Acknowledgements

Dear reader,
although there is only one author named on the cover page of this thesis, more people than me contributed directly or indirectly to this work and enabled that I am now able to write these last lines of my thesis.

First of all I would like to express my deep thankfulness to Prof. Cynthia Volkert who motivated me to start with this thesis, gave me the chance to work in her group and guided me through this process as my supervisor. Although it was sometimes difficult for me to stay on track I would like to thank for Cynthia´s sympathy, constant support and will to move this project forward.

I would also like thank Dr. Marcel Risch, for being part in my thesis committee, becoming my second examiner and for numerous interesting, clear and fruitful discussions that helped me to move forward. At this place I would also like to thank Marcel for making it possible to experience beam time at ALBA and BESSY.

In the same course, I would like to thank Prof. Jörg Behler for being part of my thesis committee, his interest in connecting theory and experiment and for his constant support throughout this work. I would also like to thank all further members of the examination board for this thesis and the defense.

The collaboration with Dr. Marco Eckhoff was a great pleasure for me and a very valuable insight for me to learn about our material system from another angle. I would like to thank him for providing me with simulations of EEL spectra and the possibility to publish articles with him. I would also like to thank Dr. Tobias Meyer for his support in conducting and interpreting ETEM experiments. Dr. Max Baumung and Dr. Omeshwari Bisen, both partners in the research project C05 of the SFB 1073 are gratefully acknowledged for providing samples, electrochemical experiments and dis-

cussions about their work.

I would like to thank as well my work group and all members of the institute for materials physics for the open and encouraging environment, help with experiments and questions, and a very enjoyable time. I would like to mention Niklas Weber and Tobias Schulz especially. Niklas and me started working at the IMP at the same. We did not only share the same fate and office but also interests so that Niklas became a great friend. Thank you for accompanying me during the last years and thank you for a very valuable time together. Tobi also made the the institute becoming a very enjoyable place and I enjoyed his special way to motivate people a lot.

Finally I would like to thank my family and friends who supported me on the way to finish this last paragraph. Louis and Erna have been very valuable and understanding friends and I am very happy that I could share ideas, thoughts, doubts and good moments with them. My parents Hartmut, Cinja and Ralph and my sister Luisa gave me their constant and unconditional support throughout my university career, thank you for accompanying me. I would also like to thank Jules who, as my partner, was my closest companion in finishing this work.